UNIVERSITY OF TRENTO

Doctoral School in Civil, Environmental and Mechanical Engineering

Curriculum 1. Civil and Environmental Engineering

Gabriele Barile

River bifurcations: key processes, timescales and evolutionary trajectories



2025 - Doctoral thesis

Supervisors
Prof. Marco Tubino - University of Trento, Trento, Italy
Prof. Marco Redolfi - University of Modena and Reggio Emilia, Modena, Italy

Examination Committee
Prof. Walter Bertoldi - University of Trento, Trento, Italy
Prof. Chris Paola - University of Minnesota, Minneapolis, USA
Prof. Luca Ridolfi - Politecnico di Torino, Turin, Italy

Front Cover: Tigris River (credits: Google Earth)

ABSTRACT

River bifurcations are constituent components of multi-thread fluvial systems, playing a crucial role in their morphodynamic evolution. As highlighted by several field studies and laboratory investigations, natural bifurcations tend to display unbalanced configurations, in which one branch carries most of the incoming water and sediment supply. This tendency often results in the partial or complete abandonment of one of the bifurcates (known as avulsion), leading to the diversion of the majority or all the incoming water and sediment discharges towards the other bifurcate. Most studies in the literature either focused on the long-term equilibrium configurations of bifurcations or tailored their analysis on specific case studies, rarely addressing avulsion conditions. Moreover, only a few works aimed at quantifying the characteristic timescales with which a bifurcation evolves towards its long-term configuration. Among the different fluvial contexts in which the dynamics of bifurcations is relevant, river deltas are of particular interest from both a geomorphological and coastal management viewpoints. Interestingly, available relations for sediment division at bifurcations mostly concern bedload transport, while within deltas most of the sediments are transported in suspension.

The first part of this PhD thesis focuses on the key physical processes underlying the evolution of river bifurcations, along with their characteristic timescales and the different resulting evolutionary trajectories. These analyses are carried out mostly by means of a novel one-dimensional numerical model of a bifurcation, which is formulated by combining the solution of the free-surface profiles and Exner equations along the branches with existing nodal point relations for sediment partitioning. The numerical model is firstly employed to explore the conditions in which one branch has a vanishing transport capacity, to overcome the limitations of existing equilibrium models. Model results show that when the difference in the flow discharges among the bifurcates is so high that one branch no longer transport sediments (partial avulsion conditions), the other branch undergoes significant degradation due to an autogenic process, which leads to the abandonment of the non-transporting branch when the bifurcates are sufficiently long. To complement the numerical findings, a new analytical model is formulated to reproduce the essential characteristics of the partial avulsion equilibrium and to identify the key parameters that control the transition between different long-term configurations. The same numerical model is then used to quantify the evolutionary timescale of bifurcations, looking at the velocity with which small perturbations are amplified as a result of the free instability of the system. Firstly, an operative definition of the intrinsic timescale of a bifurcation is provided; then, its dependence on the governing parameters, namely the flow conditions in the upstream channel and the length of the bifurcates, is investigated. By combining the numerical results with those obtained through a linear analytical model, the bifurcation timescale is then compared with those of external forcings, namely migrating bars and time-varying flow discharge. The second part of the thesis concerns bifurcations belonging to river-dominated deltas. Specifically, an in-depth analysis of the flow and sediment division at several bifurcations belonging to the Wax Lake Delta (US) is performed, by means of a Lagrangian particle tracking model and a 2D numerical hydrodynamic model. First, sediment particles are routed on previously calibrated hydrodynamic simulations performed for the whole delta. The resulting sediment partitioning at each bifurcation satisfactorily compared against available field data on suspended sediment concentration. To extend our findings to similar deltaic contexts, the same numerical tools are then used on a synthetic geometry, which allows for a broad analysis of the role of differences in channel width, branching angle and inlet bed elevation between the bifurcates on water and sediment partitioning.

The insights gained from these analyses provide a foundation for further investigations on natural bifurcations and may offer valuable information for the design of sustainable river restoration projects in different fluvial contexts. Moreover, our

investigations on deltaic bifurcations help to understand the preferential pathways for sediment transport in river deltas, with noteworthy implications for delta management.

CONTENTS

I Introduction

1 A brief overview of river bifurcations 2

2 Modelling bifurcations 5

3 Research questions and outline of this work 17

II Avulsions in river bifurcations

4 Introduction 20

5 Methods 23

5.1 Formulation 23

5.2 Numerical scheme 25

6 Results 28

7 Simplified equilibrium model for partial avulsions 36

8 Discussion and conclusions 41

9 Appendix: comparison with laboratory experiments 46

III How fast do bifurcations evolve?

10 Introduction 49

11 Model formulation 52

11.1 Numerical implementation 54

12 Linear analysis 56

12.1 Linear solution for downstream channels 56

12.2 Coupled solution for the bifurcation-downstream channels system 58

13 Results 60

13.1 Transient behaviour of bifurcations 60

13.2 The bifurcation timescale 63

13.3 Insights on the morphological response of the bifurcates 66

14 Discussion and conclusions 72

14.1 Bifurcation timescale and flow variability 72

14.2 Bifurcation timescale and bar evolution 74

14.3 Comparison between different models 76

15 Appendix: coefficients arising from linear analysis 80

IV Water and sediment division at deltaic bifurcations: lessons from the Wax Lake Delta (USA)

16 Introduction 84

17 Methods 86

17.1 The ANUGA and dorado numerical models 86

17.2 Definition of the asymmetry indicators 87

17.3 Local analysis of the bifurcations in the Wax Lake Delta 87

17.4 Setup of dorado simulations for the Wax Lake Delta 90

17.5 Computation of sediment fluxes from Total Suspended Solid measurements in the Wax Lake Delta 91

17.6 Simplified geometry 93

18 Results 95

18.1 Bifurcations in the Wax Lake Delta 95

18.1.1 Asymmetries computed using ANUGA and `dorado` 95

18.1.2 Comparison with remote sensing estimates 97

18.2 Simplified geometry 99

19 Discussion and conclusions 103

20 Appendix: simple formula for the flow partitioning 108
21 Supporting Information 110
21.1 Sediment flux map of the Wax Lake Delta 110
21.2 Cross-section profiles of the bifurcations in the Wax Lake Delta 111
21.3 Further details on the synthetic geometry definition 112

v Concluding remarks
22 Conclusions 114
23 Closing statements 120

Part I

INTRODUCTION

1 A BRIEF OVERVIEW OF RIVER BIFURCATIONS

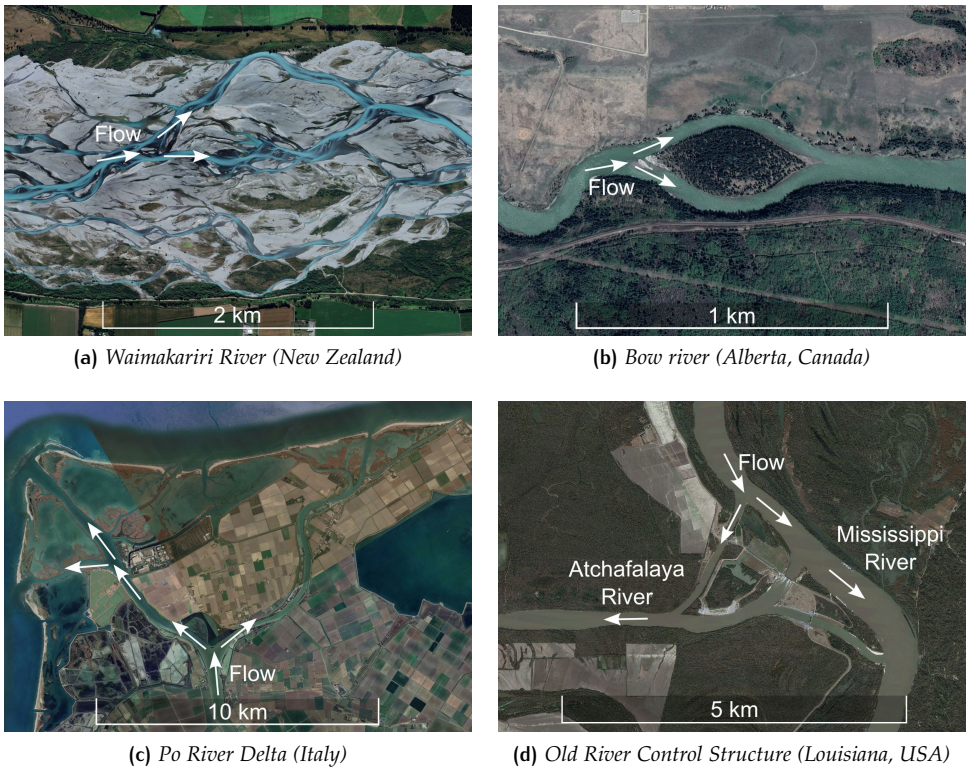
RIVER BIFURCATIONS: WHAT ARE THEY? WHY DO WE NEED TO STUDY THEM?

As river scientists, we enjoy spending quite some time looking at satellite images of fluvial systems and wandering along rivers in field surveys. During these investigations, it is quite common to encounter rivers that split in two (or more) channels, sometimes reconnecting further downstream. This phenomenon, usually referred to as *branching*, can be observed in very different fluvial contexts, some examples of which are illustrated in Figure 1.1: braiding rivers, meander cutoffs, river deltas, alluvial fans, and anastomosing rivers are all examples of riverine systems where branching occurs frequently in space and time. Following the established terminology adopted in geomorphology, we will use the term *river bifurcation* to refer to the ensemble of the branching node and the channels attached to it. Understanding how water and sediments split at bifurcations, and how this splitting impacts the morphological evolution of the downstream branches is a crucial effort to make in order to sketch the evolutionary trajectory of branching systems at different scales. In fact, outlining the possible behaviour of individual bifurcations can inform modelling efforts focusing on more complex networks.

Besides their relevance in natural branching systems, river bifurcations are increasingly involved in river engineering projects with different aims. Firstly, river practitioners often prescribe the creation or reactivation of bifurcations as part of restoration projects (Habersack & Piégay, 2007). Moreover, man-made bifurcations can also be designed for water resource management and flood control purposes, and to enhance the ecological functionality of rivers while maintaining their navigability (Vuren et al., 2006). Some examples of these practices are given by longitudinal training walls (Konsoer et al., 2024; Le et al., 2020) and reopening of abandoned side channels (AIPO, 2022; Mandler et al., 2004; Muhar et al., 2016). Trying to assess the stability of bifurcations, evaluating whether both branches are likely to effectively transport water and sediments in the long-term, is a necessary step to ensure the effectiveness and sustainability of these engineering interventions.

PHENOMENOLOGY OF RIVER BIFURCATIONS

Regardless of the surrounding fluvial context, both natural and man-made bifurcations are often asymmetrical, with one branch carrying the majority of the incoming water and sediments. The most evident mark of this uneven flux distribution is the different channel width of the downstream branches. Interestingly, the bifurcation asymmetry can also manifest itself as a bathymetric difference between the branches, which previous studies referred to as "inlet steps" (Bolla Pittaluga et al., 2003). Such steps are commonly observed in braiding networks (Zolezzi et al., 2006) and other anabranching rivers (Rodrigues et al., 2006; Slingerland & Smith, 2004), man-made side channels (Le, Crosato, & Uijttewaal, 2018; Van Denderen et al., 2019) and river deltas (Buschman et al., 2010; Edmonds and Slingerland, 2008, Part iv of this work), and they considerably affect the partitioning of water and sediments at the bifurcation node (Bertoldi & Tubino, 2007). As one may expect, larger bathymetric differences are associated with a larger asymmetry in the flux distribution between the branches; as will be shown in Part ii, very large bathymetric steps can indicate



(a) *Waimakariri River (New Zealand)*

(b) *Bow river (Alberta, Canada)*

(c) *Po River Delta (Italy)*

(d) *Old River Control Structure (Louisiana, USA)*

Figure 1.1: Examples of river bifurcations located in different fluvial contexts. All images have been retrieved from Google Earth.

that the minor branch is close to channel closure, i.e., it has a vanishing capability to effectively convey a portion of the incoming water and sediments.

Bifurcations also show different degrees of planform activity, ranging from multi-decadal stability (Kästner & Hoitink, 2019) to swift changes in the partitioning of water and sediments between the branches, as often observed in braiding networks (Bertoldi, 2012), which can trigger rapid morphological changes in the downstream branches (Edmonds et al., 2009; Van Denderen et al., 2019). Investigating the factors that control the velocity of the morphological evolution of bifurcations, as done in Part iii, is relevant per se, but also gives insights on the interplay between the bifurcation morphodynamics and other unsteady processes that may affect it. In fact, several field studies and laboratory experiments pointed out that both the transient behaviour and the long-term regime configuration of bifurcations can be influenced by a variety of external forcings. For example, bifurcations in gravel-bed anabranching rivers are subject to rapid flow rate variations and interact with migrating bars (Ashmore, 1991; Bertoldi, 2012; Burge, 2006; Ferguson et al., 1992). Furthermore, the morphodynamic evolution of bifurcations in lowland rivers is usually affected by downstream controls, such as tides (Wagner & Mohrig, 2019), differences in the longitudinal bed slope (Edmonds, 2012; Van Dijk et al., 2012), steady changes in the downstream water level (Jerolmack, 2006; Kleinhans et al., 2013) and prograding branches (Salter et al., 2018). In these contexts, changes in the incoming flow discharge are typically regulated by the hydrological cycle, and peak flood events can trigger substantial changes in bifurcation evolutionary trends (Chowdhury et al., 2023) and channel abandonment (Toonen et al., 2012).

As a result of their morphodynamic evolution, bifurcations can experience channel abandonment, in which one of the two downstream channels stops transporting water and sediment. This phenomenon was widely observed both in bedload-dominated (Ferguson, 1993; Field, 2001), and suspended-load dominated (Makaske, 2001; Mohrig et al., 2000; Slingerland & Smith, 2004) rivers. Predicting the conditions

that can lead to channel abandonment, to which Part ii provides a contribution, is crucial for both understanding how river networks evolve over time and designing effective river engineering projects that involve the (re)opening of side channels. In the following, we will refer to channel abandonment using the term "avulsion", following the terminology adopted by previous studies on bifurcations (Edmonds & Slingerland, 2008; Salter et al., 2018). We acknowledge that the same term has been extensively adopted to describe the incision of a new channel in the floodplain as a result of a levee breach (Slingerland & Smith, 2004). The two definitions are not mutually exclusive, but rather refer to two different time frames: in this work we study the evolutionary trajectory of already developed bifurcations, regardless of their formation mechanism; the more common definition of avulsion encompasses the whole process, including both the formation of new channels and the diversion of part or all of the incoming flow (Smith, 1978).

2 MODELLING BIFURCATIONS

Modelling river bifurcations is a matter of quantifying how much the partitioning of sediments at the node differs from the partitioning of water, and how this difference can cause a mismatch between the sediment supplied to each branch and the transport capacity of the branch itself. This imbalance drives the morphodynamic evolution of the downstream branches (i.e., the *bifurcates*), and therefore of the river network the bifurcation belongs to. The first modelling efforts concerning bifurcations trace back to the design criteria for man-made channel diversions (Raudkivi, 1993), which aimed at providing engineers empirical relationships to determine the geometry of the side channel in such a way to prevent its abandonment. However, these relations were usually tailored to specific case studies, and the insights they give are difficult to generalize. To broadly characterize the long-term conditions of bifurcations, several nodal points relationships were developed in the following years. By combining these relations with simplifying assumptions to model the flow conditions in the branches, different authors attempted at identifying the possible long-term equilibrium configurations of bifurcations and assessing their morphodynamic stability. These studies provided valuable insights on the morphodynamics of bifurcations, leading the way for building a comprehensive framework that encompasses bifurcations with different planform configurations and hydraulic conditions (Edmonds et al., 2022; Redolfi et al., 2019). Several works also investigated bifurcation stability using two- and three-dimensional numerical schemes (Edmonds & Slingerland, 2008; Kleinhans et al., 2008; Siviglia et al., 2013). However, most numerical studies that focused on the long-term equilibrium configurations of bifurcations failed to reproduce the observed stable, unbalanced configurations of bifurcations, leading to channel closure. The invariable abandonment of one of the bifurcates was also observed in several Delft3D simulations performed so far, even for bifurcations with a symmetric planform geometry (Durante et al., 2023; Salter, pers. comm.), and has been forcibly avoided by employing non-realistic values of the coefficient that regulates the gravitational effects on bedload transport (Gao et al., 2024; Iwantoro et al., 2021), a strategy that presents several criticalities and may hide poor modelling choices (Tritthart et al., 2024).

BIFURCATIONS AS A STABILITY PROBLEM: THE WORK BY WANG ET AL. (1995)

In a noteworthy advance, Wang et al. (1995) first studied bifurcations as a stability problem by means of a one-dimensional analytical model. Their model considered the geometry sketched in Figure 2.1, in which the three channels linked by the bifurcation node have fixed banks and a rectangular cross-section, and relied on the following equations (the subscripts a, b, c refer to the upstream, left and right branch, respectively):

- water discharge (Q) balance

$$Q_a = Q_b + Q_c, \tag{2.1}$$

- sediment discharge (Q_s) balance

$$Q_{sa} = Q_{sb} + Q_{sc}, \tag{2.2}$$

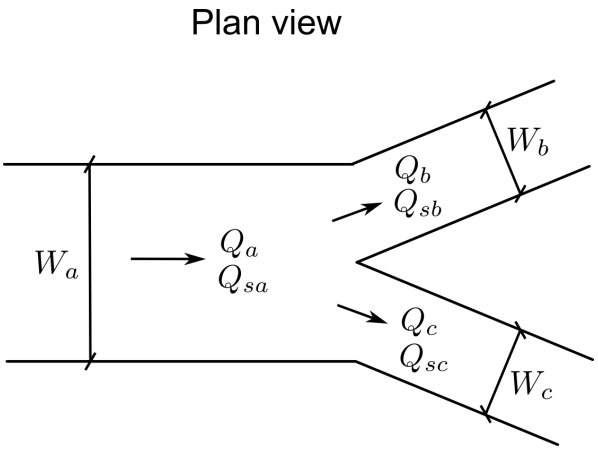


Figure 2.1: Sketch of the geometry considered by Wang et al. (1995). Q and Q_s stand for the flow and sediment rates, respectively, while W stands for the channel width.

- uniform flow conditions in the branches

$$Q_i = W_i C \sqrt{g S_i} D_i^{3/2}, \quad i = a, b, c, \tag{2.3}$$

  where W is the channel width, C is the Chézy roughness coefficient (here assumed to be constant), g is gravity acceleration, S is the longitudinal bed slope and D is the water depth,

- equal water level at the downstream end of the branches and at the bifurcation node; given the hypothesis of uniform flow conditions, these assumptions lead to the geometric relation

$$S_b L_b = S_c L_c, \tag{2.4}$$

  where L is the length of the branch.

The transport capacity of the branches is estimated by means of a power-law formula of the form

$$Q_{si} = W_i m \left(\frac{Q_i}{W_i D_i} \right)^n, \quad i = a, b, c, \tag{2.5}$$

where m and n are arbitrary coefficients.

To close the mathematical problem, they formulated a novel nodal-point relationship to predict the partitioning of sediments at the bifurcation. Specifically, their relation allows for computing the ratio between the sediment supply rate delivered to the downstream branches as

$$\frac{Q_{sb}}{Q_{sc}} = \left(\frac{Q_b}{Q_c} \right)^k \left(\frac{W_b}{W_c} \right)^{1-k}, \quad k > 0, \tag{2.6}$$

where k is an empirical parameter.

By assigning the incoming flow (Q_a) and sediment discharges (Q_{sa}), along with the planform geometry of the bifurcation (i.e., the channel width and length of the bifurcates) and the roughness coefficient C, Wang et al. solved the system of Equations (2.1-2.6) for the unknowns S_i, D_i, Q_i, Q_{si} ($i = b, c$), identifying the possible equilibrium configurations of the bifurcation.

Their results revealed that the system only admits of two categories of equilibrium configurations:

- a balanced configuration, in which water and sediments are split evenly between the downstream branches;

- channel abandonment, in which all the incoming water and sediments are carried by one of the two downstream channels.

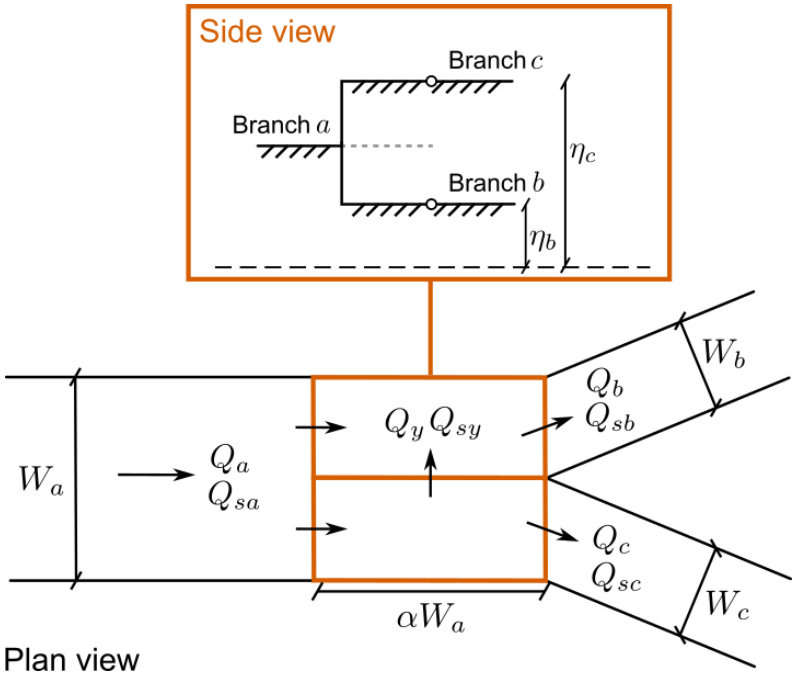


Figure 2.2: Sketch of the geometry considered by Bolla Pittaluga et al. (2003).

The authors then performed a linear stability analysis of the balanced configuration, exploring its dependence on the parameter k. Their results showed that lower values of k, i.e. a lower dependence of the sediment partitioning on the water partitioning (see Equation 2.6), cause the balanced configuration to be unstable and lead the bifurcation to evolve towards channel abandonment, i.e. the only other equilibrium state permitted by their model. According to their linear analysis, the threshold value k below which the balanced configuration equals $n/3$, where n is the exponent of the power-law formula adopted to estimate the transport capacity of each branch (see Equation 2.5).

The main limitation of this formulation resides in the high dependence of the results on the empirical parameter k, which must be calibrated on a case-by-case basis, thus making it difficult to use it for general purposes (Kleinhans et al., 2008). Moreover, this model is unable to reproduce the unbalanced bifurcations observed in the field and in laboratory experiments (Bertoldi & Tubino, 2007), in which one of the two branches carries a smaller fraction of the incoming water and sediments without being abandoned.

Following Wang's work, two seminal studies employed a physically based approach to characterize the sediment division at bifurcations, employing a one-dimensional approach for the three channels. On the one hand, Bolla Pittaluga et al. (2003) focused on the effect of the local transverse bed slope at the node on the partitioning of bedload transport, while Slingerland and Smith (1998) modelled the division of suspended sediments with reference to a bifurcation in a lowland sandy river. These two works are described more in detail in the following.

THE BRT NODAL POINT RELATION

The nodal relationship formulated by Bolla Pittaluga et al. (2003), hereafter referred to as BRT, is built upon the widely known influence exerted by a transverse bed slope on the direction of bedload transport, which the author quantify following Ikeda et al. (1981). This effect plays a key role in the partitioning of bedload transport at bifurcations: in fact, both field (Zolezzi et al., 2006) and laboratory (Bertoldi &

Tubino, 2007) evidence suggests that natural bifurcations often display a transverse bed slope immediately upstream of the bifurcation node, which accommodates the difference in bed elevation between the bifurcates (i.e., the *inlet steps* mentioned in the previous chapter). To include this transverse bed gradient in their model formulation, Bolla Pittaluga et al. discretized the last reach of the upstream channel by means of two adjacent nodal cells (Figure 2.2), which are allowed to exchange water and sediment in the transverse direction (hereafter denoted with the y subscript). At the upstream end of the cells, the incoming flow and sediment discharge are distributed homogeneously along the cross-section, so that the fluxes entering the node cells are proportional to their width. The length of the cells equals αW_a, where α is a calibration parameter and W_a is the width of the upstream channel. Physically, α identifies the portion of the upstream channel affected by the two-dimensional effects due to the presence of the bifurcation node; following the evidence provided by their laboratory experiments, Bolla Pittaluga et al. (2003) suggested that α is an order-1 parameter. Each node cell is characterized by a single value of bed elevation, which corresponds to the inlet bed elevation of the corresponding branch. The transverse bed gradient can therefore be quantified as the difference between the bed elevations of the two node cells divided by the distance between their centroids.

For the sake of simplicity, in the following the model formulation will be presented for the case of a symmetric planform geometry, where the width of the branches satisfy $W_b = W_c = W_a/2$. In this case, the bed gradient $\partial\eta/\partial y$ equals

$$\frac{\partial \eta}{\partial y} \sim \frac{\eta_b - \eta_c}{W_a/2}, \tag{2.7}$$

where η_b and η_c are the bed elevations of the node cells (Figure 2.2). The transverse flux of sediments Q_{sy} at the bifurcation node is then estimated using the bulk relationship

$$\underbrace{\frac{Q_{sy}}{Q_{sa}}}_{\text{bedload direction}} = \underbrace{\frac{Q_y}{Q_a}}_{\text{flow direction}} - \underbrace{\frac{\alpha r}{\sqrt{\theta_a}} \frac{\eta_b - \eta_c}{W_a/2}}_{\text{gravitational effect}}, \tag{2.8}$$

where r is an empirical coefficient which may vary between 0.3 and 1 (see e.g. Baar et al., 2018), θ_a is the Shields stress of the incoming flow, and $\partial\eta/\partial y$ is the transverse bed elevation gradient.

Lastly, the transverse water discharge Q_y can be readily derived from mass balance considerations within the node cells as

$$Q_y = \frac{1}{2}\left(Q_b - Q_c\right). \tag{2.9}$$

The gravitational effect on the transverse flux of sediments, as quantified by the second term of the right-hand side of Equation (2.8), plays a crucial role in the morphodynamic stability of the downstream branches. In fact, this term increases the sediment supplied to the branch having a smaller inlet bed elevation, which carries the larger fraction of the incoming water and sediments. If sediments split proportionally to water (i.e., if we neglected the gravitational effect), there would be a strong mismatch between the sediment supplied to each branch and its transport capacity, due to the strongly nonlinear relationship between the latter and the flow discharge. This mismatch would enhance erosion in the dominant branch and deposition in the non-dominant branch, further amplifying the degree of asymmetry of the bifurcation. We note that this assumption is equivalent to employing the model by Wang et al. (1995) using $k = 1$, which inevitably leads to channel closure according to their results. The inclusion of the gravitational term counteracts this instability, adding a surplus to the bedload redirected towards the dominant branch and facilitating the achievement of the morphological equilibrium.

Rather than writing an overall sediment mass balance for the bifurcation node as done by Wang et al. (1995) (Equation 2.2), Bolla Pittaluga et al. considered in the model the Exner equation in integral form written for each node cell, which read

$$\begin{aligned}(1-p)\frac{\alpha W_a^2}{2}\frac{d\eta_b}{dt} + Q_{sb} - Q_{sb}^{IN} - Q_{sy} = 0\\ (1-p)\frac{\alpha W_a^2}{2}\frac{d\eta_c}{dt} + Q_{sc} - Q_{sc}^{IN} + Q_{sy} = 0,\end{aligned} \tag{2.10}$$

where p is bed porosity, t is time, and Q_{sb}^{IN} and Q_{sc}^{IN} denote the sediment fluxes entering each cell. In the simple configuration with a symmetric planform configuration, the latter is estimated by assuming that the incoming sediment discharge is split evenly between the node cells, i.e.

$$Q_{sb}^{IN} = Q_{sc}^{IN} = \frac{Q_{sa}}{2}. \tag{2.11}$$

The transport capacities of the downstream branches (Q_{sb}, Q_{sc}) are written in the general form

$$Q_{si} = W_i\sqrt{g\Delta D_s^3}\Phi(\theta_i), \quad i = b, c, \tag{2.12}$$

where the unit dimensionless transport capacity Φ is evaluated according to Meyer-Peter and Müller (1948) as

$$\Phi = 8\,(\theta - \theta_{cr})^{3/2}, \quad \theta_{cr} = 0.047. \tag{2.13}$$

Given the uniform flow assumption, the Shields stress can be written for each branch as

$$\theta_i = \frac{S_i D_i}{\Delta D_s}, \quad i = a, b, c. \tag{2.14}$$

Another closure relationship is needed for the Chézy roughness coefficient, which is written in terms of the water depth according to a standard logarithmic law

$$C = 6 + 2.5\log\left(\frac{D}{2.5D_s}\right). \tag{2.15}$$

The addition of the unknown bed elevation of the node cells (η_b, η_c) to the model formulation requires two new conditions to close the mathematical problem. To achieve this, the authors used the hypothesis of flat water-surface elevation at the bifurcation node (also done by Wang et al., 1995), from which they derived the equations

$$\eta_a + D_a = \eta_b + D_b = \eta_c + D_c, \tag{2.16}$$

where η_a is the reference bed elevation at the downstream end of the upstream channel, which the authors assume to be equal to $\eta_a = (\eta_b + \eta_c)/2$.

The BRT model can thus be written as the system of eight equations composed of the water mass balance (2.1), the two uniform flow rating curves (2.3), the geometric relationship for the slopes of the bifurcates (2.4), the Exner equations for the node cells (2.10) and the two conditions deriving from the flat surface elevation hypothesis (2.16). The equilibrium solutions of this system can be found by setting $d\eta_i/dt = 0$ in Equations (2.10) and solving the resulting eight algebraic equations for the eight unknowns $\eta_b, \eta_c, D_b, D_c, S_b, S_c, Q_b, Q_c$. Note that the transport capacities Q_{sb} and Q_{sc} can be written in terms of the bed slope and water depth of the branches through Equations (2.12,2.13,2.14). It is worth highlighting that the solution of the governing system of equations only depends on the ratio between the length of the branches, which sets the bed slope ratio S_b/S_c according to the geometrical relationship (Equation 2.4), thus it is independent of the length of each bifurcate.

The authors presented the model results in terms of the uniform flow conditions of the upstream channel, noted in the following with the subscript o. Specifically,

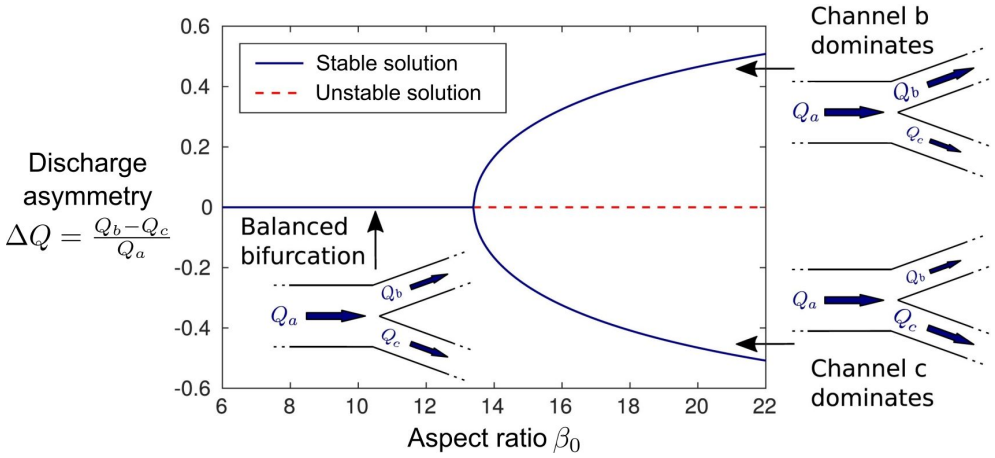


Figure 2.3: Equilibrium solutions of a bifurcation according to the model by Bolla Pittaluga et al. (2003), where the difference between the flow discharge of the branches ΔQ (defined as in Equation 2.18) is plotted against the width-to-depth (aspect) ratio of the upstream channel. Figure adapted from Redolfi et al. (2019).

they defined these conditions in terms of three dimensionless parameters, namely the Chézy coefficient C_0, the Shields stress θ_0 and the half-width to depth ratio β_0 (hereafter, *aspect ratio*), defined as

$$\beta_0 := \frac{W_a/2}{D_0}. \tag{2.17}$$

The two parameters β_0 and θ_0 are also the main drivers of the gravitational effect on the transverse flux of sediments, as suggested by Equations (2.8, 2.7). Thus, looking at the equilibrium solutions through the lens of these parameters allows for focusing on the role played by the core of the nodal point relationship.

The authors noted that imposing the values of the three parameters β_0, θ_0 and C_0 completely determines the reference flow conditions of the upstream channel, once the sediment properties (Δ, D_s) have been defined. In fact, for a given value of the reference grain size D_s, the flow depth D_0 can be obtained by reversing Equation (2.15); then, the channel width W_a and bed slope S_0 can be derived from Equation (2.17) and Equation (2.14), respectively. Lastly, the flow and sediment discharges of the upstream channel a (i.e. Q_a and Q_{sa}, respectively) can be computed through Equations (2.3,2.12).

In the following, we will look at the equilibrium solutions given by the BRT model for bifurcations with branches of equal length ($L_b = L_c$). It is worth noting that the latter condition implies that, following Equation (2.4), the bifurcates have the same bed slope. Moreover, the degree of asymmetry of the equilibrium will be analysed in terms of the dimensionless flow discharge asymmetry ΔQ, as defined by Bertoldi et al. (2009):

$$\Delta Q = \frac{Q_b - Q_c}{Q_a}. \tag{2.18}$$

Analogously to the model formulated by Wang et al. (1995), the BRT model admits of a balanced equilibrium configuration, in which water is split evenly between the bifurcates (i.e. $\Delta Q = 0$), which are characterized by the same values of water depth and bed slope. In this configuration the node cells have the same bed elevation, i.e. the inlet step vanishes. For lower values of the aspect ratio β_0, this configuration represents the only stable equilibrium point of the bifurcation. When β_0 exceeds a critical threshold, the balanced configuration becomes unstable and the bifurcation admits of two unbalanced, albeit stable, specular equilibrium configurations, characterized by the same absolute value of ΔQ but different sign (Figure 2.3); the resulting equilibrium diagram thus takes the form of a *pitchfork bifurcation*. Moreover, the authors found the critical threshold of the aspect ratio for

the bifurcation stability to increase with the reference Shields stress θ_0. However, as outlined by following studies that employed the BRT model (Bolla Pittaluga et al., 2015), this dependence may change according to the adopted transport formula: by using the transport formula by Engelund and Hansen (1967), the critical aspect ratio decreases with the Shields stress.

In the unbalanced solutions, water and sediment fluxes are split unevenly between the bifurcates, and the node cells —and therefore the inlets of the two bifurcates— have two different values of bed elevation, the lower node cell being that corresponding to the dominant branch. Moreover, in unbalanced configurations the bed slope of the downstream branches is lower than that of the upstream channel. Notably, in these solutions the non-dominant channel is never abandoned, whereas the model by Wang et al. (1995) would predict the closure of the non-dominant branch whenever the balanced solution is unstable. In the BRT model, the existence of unbalanced equilibrium solutions is mainly determined by the stabilizing effect exerted by the gravitational term, the magnitude of which is governed by the aspect ratio β_0. For a given value of the reference flow depth, smaller values of β_0 correspond to a narrower channel, thus to a larger transverse bed slope $\partial\eta/\partial y$ (provided the same perturbation of the transverse bed slope, see Equation 2.7) and therefore to a stronger stabilizing effect, which prevents the formation of unbalanced equilibrium states by flattening any perturbation to the transverse bed slope at the node. For larger values of β_0, albeit less intense, the same effect makes the sediment supplied by the bifurcation node to match the transport capacity of the dominant branch, allowing it to reach the morphological equilibrium.

The ability of the BRT model to represent unbalanced bifurcations by means of a physically-based approach represented a noteworthy advance, which led it to be widely adopted in following studies (Edmonds et al., 2022). However, this formulation becomes inherently inconsistent when the transport capacity of the non-dominant branch vanishes, thus in the conditions that may lead to channel abandonment. This limit will be addressed in Part ii, in which these conditions will be investigated through a novel, unsteady numerical model.

INSIGHTS FROM THE BRT MODEL: FREE AND FORCED MORPHODYNAMICS OF BIFURCATIONS

Free bifurcations

Here we use the term *free bifurcation* to refer to the simple geometric configuration considered by Wang et al. (1995) and Bolla Pittaluga et al. (2003), in which there is no external factor that favours one of the two bifurcates. In this case, the development of an unbalanced configuration is due uniquely to the autogenous mechanism described in the previous section, and it is driven by the nodal point relationship (Equation 2.8). The framework outlined by the BRT model performed well at describing the experimental results obtained by Bertoldi and Tubino (2007) on a laboratory-scaled physical model of a free bifurcation. In fact, laboratory runs with lower reference aspect ratio and Shields stress remained balanced over time, while in the other runs the bifurcation evolved spontaneously towards an unbalanced configuration, displaying degradation in one branch and deposition in the other and reaching a stable, long term equilibrium. By considering a single value for the calibration parameter α, the authors showed that the BRT model correctly predicted the balanced or unbalanced character of the observed equilibrium configurations, based on the flow conditions of the upstream channel. Moreover, the authors analysed their findings using the theory of morphodynamic influence proposed by Seminara et al. (2001). According to this theory, there exist a *resonant* aspect ratio β_R above which any disturbance of the flow field (such as channel curvature,

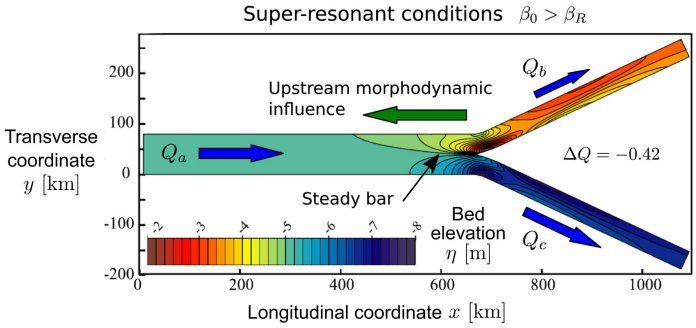


Figure 2.4: Bed elevation map of a river bifurcation as returned by the Delft3D numerical simulations performed by Edmonds and Slingerland (2008). Figure adapted from Redolfi et al. (2019).

or a partial obstruction of the cross-section) is felt preferentially in the upstream direction (*super-resonant* conditions), while it is felt mainly downstream for $\beta_0 < \beta_R$ (*sub-resonant* conditions). For the case of a bifurcation, the disturbance is exerted by the nodal conditions when the discharge is unevenly distributed and an inlet step between the downstream branches develops, which requires a corresponding transverse bed deformation in the upstream channel. Bertoldi and Tubino highlighted how experimental runs performed in super-resonant conditions always reached unbalanced equilibrium states, while the degree of asymmetry (in terms of flow partitioning and difference in the bed elevation of the bifurcates) was negligible in the sub-resonant ones. The authors explained this finding by arguing that the occurrence of unbalanced equilibrium solutions depends on the formation of a steady bar upstream of the node, which only occurs when the bifurcation is able to exert a morphodynamic influence in the upstream direction (i.e., when the upstream channel is in super-resonant conditions). The presence of the bar means that most of the water and sediment coming from the main channel is directed towards the branch corresponding to the depression produced by the bar. The results obtained by Bertoldi and Tubino (2007) were later confirmed by the numerical simulations performed by Edmonds and Slingerland (2008): in fact, their results provided a straightforward example of the bed configuration of an unbalanced (free) bifurcation in super-resonant conditions, showing that a steady bar forms upstream of the bifurcation node (Figure 2.4).

The strong link between the morphodynamic influence theory and the stability of bifurcations was demonstrated by Redolfi et al. (2016), who derived a two-dimensional analytical solution of the morphodynamic problem at the bifurcation node. Their results clearly showed that an initially balanced free bifurcation is subject to instability and tends towards an unbalanced equilibrium only if the reference aspect ratio β_0 of the upstream channel is greater than the resonance threshold β_R. In particular, if $\beta_0 < \beta_R$ the only stable equilibrium configuration is the balanced one, whereas for $\beta_0 > \beta_R$ two unbalanced, specular equilibrium solutions coexist. The bed elevation map returned by their analytical model for a sub-resonant and a super-resonant case are illustrated in Figure 2.5. The resonance criterion introduced by Redolfi et al. (2016) was validated by Redolfi et al. (2019), who analysed a database containing 71 bifurcations studied in the field, modelled numerically or reproduced in the laboratory, predicting the balanced or unbalanced nature of each bifurcation from the hydraulic parameters of the channel upstream and comparing the result with available information (Figure 2.6).

The resonance criterion for the bifurcation stability also allowed Redolfi et al. (2019) to write an explicit formula to compute the coefficient α a priori, without the need for calibrating it. This formula was derived by imposing the equivalence between the resonant aspect ratio β_R (which is a function of the reference flow conditions only) and the critical aspect ratio for the bifurcation stability, as returned

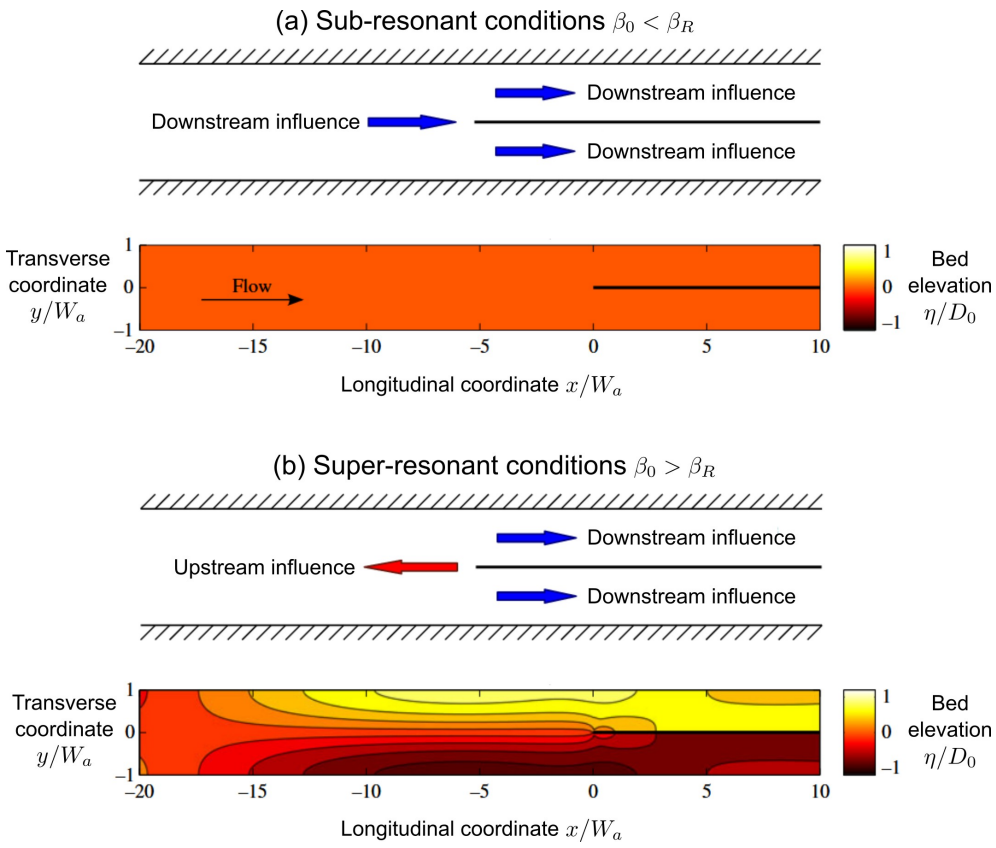


Figure 2.5: Bed elevation maps of the three channels connected to a bifurcation node having a vanishing angle in (a) sub-resonant and (b) super-resonant conditions. The arrows show the directions of the morphodynamic influence in each channel. The x and y coordinates are scaled with the width of the upstream channel, while the bed elevation η is scaled with the reference flow depth. Figure adapted from Redolfi et al. (2016).

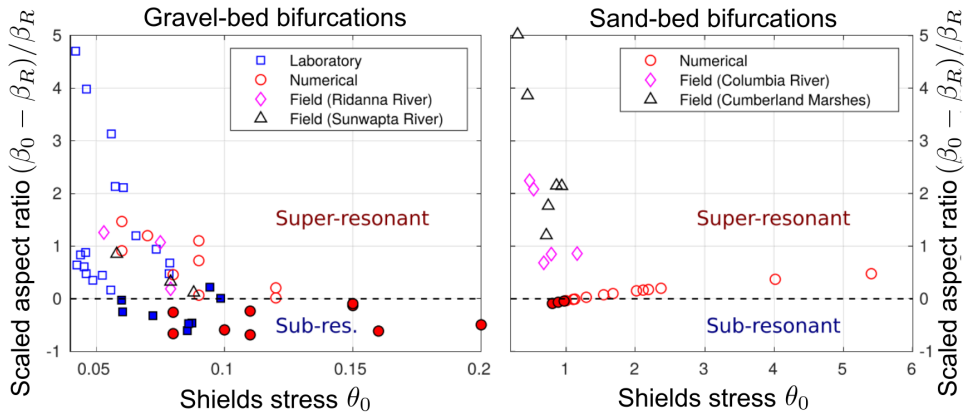


Figure 2.6: Validation of the stability criteria based on the resonant aspect ratio suggested by Redolfi et al. (2016). Filled markers indicate unbalanced bifurcations, while empty markers indicate balanced bifurcations. Figure adapted from Redolfi et al. (2019).

by the linear stability analysis of the BRT model performed by Bolla Pittaluga et al. (2015), which depends explicitly on the α parameter.

Forced bifurcations

As outlined in the previous sections, there are many factors that can influence the evolutionary trajectory of natural bifurcations. These factors, which we will refer to as *forcings*, can affect either the upstream or downstream channels of a bifurcation. Building upon the formulation proposed by Bolla Pittaluga et al. (2003), several studies investigated the possible regime configurations of bifurcations under the influence of these forcings — i.e., of *forced* bifurcations.

A few examples of upstream forcings that can interact with evolving bifurcations are alternate bars, a curvature in the upstream channel, and the variations of flow and sediment supply over time. Within the BRT framework, these effects were modelled by considering an uneven distribution of liquid and solid flow rates at the inlet of the two node cells. For instance, Kleinhans et al. (2008) derived a formula to compute the water and sediment entering the node cells for the case of a curved upstream channel, by accounting for the effect of secondary currents. Redolfi et al. (2019) analysed the implications of this effect for the long-term equilibrium configurations, distinguishing the behaviour of sub-resonant bifurcations ($\beta < \beta_R$) from that of super-resonant bifurcations ($\beta > \beta_R$). As shown in Figure 2.7, under sub-resonant conditions the hydraulic and morphological effect of curvature on the upstream channel causes the branch located on the outer side to always become dominant. This makes the equilibrium configuration unbalanced, where instead the BRT model for the free bifurcation provides a balanced solution (i.e. $\Delta Q = 0$). In other words, in sub-resonant conditions the bifurcation equilibrium is mainly determined by the external forcing. On the other hand, under super-resonant conditions a first stable equilibrium solution does not significantly differ from the unbalanced equilibrium solution predicted by BRT, having as dominant branch the one located at the outer side of the curve. As predicted by BRT, there is a second stable, unbalanced equilibrium solution where it is the other branch that has a greater flow rate. The latter equilibrium solution may therefore appear counter-intuitive, since the branch located at the inner side of the upstream curve has a greater flow rate. Considering values of the aspect ratio considerably larger than the resonant aspect ratio, the equilibrium flow asymmetry of the forced bifurcation matches that of the free bifurcation, i.e., the influence of secondary currents in the upstream channel become negligible and the equilibrium configuration is entirely determined by the intrinsic instability mechanism of the free bifurcation. Overall, the effect of the curvature of the upstream channel shows that the impact of external forcings on the degree of asymmetry of a bifurcation are mitigated or amplified by the interaction of the forcings themselves with the inherent instability of the bifurcation, the intensity of which mainly depends on the aspect ratio β_0 and the resonance value β_R.

Similar interactions between the intrinsic bifurcation instability and external forcings were observed for many other factors that influence real-world bifurcations, such as the effect of migrating bars (Bertoldi et al., 2009), imposed differences in the bed slope of the bifurcates (Redolfi et al., 2019), and the presence of a confluence (Ragno et al., 2021). In all these studies, the free instability of the bifurcation influenced its equilibrium configurations and their stability. Although previous works characterized the effects of different forcings on the long-term equilibrium configurations of bifurcations, little is known on the relationship between the timescales of the forcings and the timescale with which bifurcations evolve over time. Part iii investigates this issue considering this unsteady perspective, quantifying the timescale on which a bifurcation evolves and comparing with two time-dependent forcings, namely the sediment flux fluctuations due to the migration of alternate bars and the changes in the incoming flow discharge.

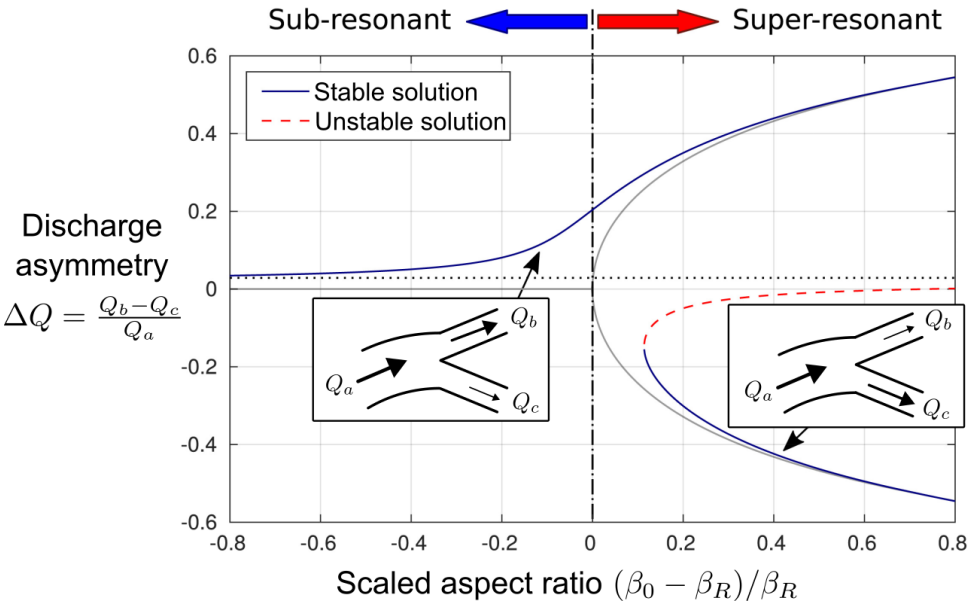


Figure 2.7: Equilibrium configurations of a forced bifurcation, where the upstream channel has a planimetric curvature. Figure adapted from Redolfi et al. (2019).

DEALING WITH SUSPENDED SEDIMENTS

Compared to their bedload-dominated counterparts, the stability and equilibrium of suspended-load dominated bifurcations have received less attention in the past. In fact, the applicability of the BRT nodal-point relationship has not been widely tested for suspended-load dominated bifurcations, where gravitational effects play a minor role in routing the transported sediments. As a nodal point relationship, previous studies simply assumed that sediment partitioning was equal to water partitioning (Edmonds et al., 2011; Hines & Piliouras, 2024; Iwantoro et al., 2021; Kleinhans et al., 2008), thus considering a uniform distribution of the sediment concentration in the water column. It follows that whenever the Rouse number of the incoming sediment flux is vanishingly small, this assumption loses validity. Moreover, as outlined in the previous sections, a partitioning of sediments proportional to the partitioning of water inevitably causes an imbalance between the sediment supply and transport capacity of each branch, which makes all unbalanced configurations unstable and therefore enhances the chances of reaching channel abandonment. However, bifurcations in suspended-load dominated systems often display unbalanced configurations that have remained stable for decades (Kästner & Hoitink, 2019; Kleinhans et al., 2012). Therefore, it is not clear what are the stabilizing factors that can counteract the instability arising by assuming a proportional partitioning of sediments, as done by the gravitational effect embedded in the BRT formulation. Kästner and Hoitink (2020) outlined several possible candidates for this stabilizing role, mentioning the influence on the partitioning of suspended sediment exerted by inlet steps (Slingerland & Smith, 2004), helical flow (Bulle, 1926; Herrero et al., 2015) and secondary currents induced by curvature in the upstream channel (Kleinhans et al., 2008).

Among the few studies on bifurcations that explicitly addressed suspension, the nodal-point relation proposed by Slingerland and Smith (1998) firstly tackled the problem through a simple, yet insightful one-dimensional formulation. Taking as reference the avulsion process in lowland rivers, they considered a bifurcation in which the avulsing channel branches off laterally and has a higher inlet bed elevation compared to the riverbed of the main channel. Given the vertical concentration profile in the main channel, the proposed relationship assumes that all sediments in the upper portion of the water column are diverted in the side channel. Specifically,

the diverted sediments are those located in the region between the side channel inlet elevation and the water surface. This formulation clearly takes into account the variability of the Rouse number of the incoming sediment flux, since larger values of this parameter would lead to a larger concentration near the riverbed and therefore a lower sediment flux supplied to the side channel. The explicit inclusion of the Rouse number in the formulation allows for bridging the proportional sediment partitioning approach, which corresponds to a vanishing Rouse number, with a novel formulation which covers the case of non-negligible values of the Rouse number, the influence of which is regulated by the height of the bathymetric step between the branches. By coupling this nodal point relationship with the same simplifying assumptions adopted by the BRT model (uniform flow conditions, flat water surface at the bifurcation node), the authors performed a series of unsteady numerical simulations finding three possible equilibrium configurations: the newly formed channel becomes dominant (avulsion), silts up, or remains open and non-dominant. This nodal-point relationship was only been adopted in unsteady numerical models (Han & Kim, 2022; Slingerland & Smith, 1998), and has not been employed to investigate the dependence of the stability and equilibrium conditions of the bifurcation on the upstream flow conditions. However, it represents the main modelling effort concerning sand-bed bifurcations, and may represent the starting point for future studies on bifurcations in sand-bed rivers.

3 RESEARCH QUESTIONS AND OUTLINE OF THIS WORK

Building upon the state-of-the-art knowledge regarding the modelling of river bifurcations, this thesis aims at addressing the following questions, by employing mainly analytical and numerical strategies:

- For which hydraulic conditions does the non-dominant branch reach a vanishing transport capacity? How is this condition linked to channel abandonment? Can we extend currently existing nodal-point relationship to understand when an evolving unbalanced bifurcation experiences channel abandonment?
- How fast do bifurcations evolve toward their equilibrium? What role does the length of the branches play in this evolutionary process? How does the timescale of bifurcations compare against variations in the upstream and downstream conditions typically observed in natural bifurcations?
- How do water and sediments split in deltaic bifurcations? Which factors should a novel relation for sediment partitioning take into account?

Part ii investigates the conditions that can lead to channel abandonment in gravel-bed bifurcations by means of a novel, one-dimensional numerical model. The same numerical model is employed in Part iii to estimate the characteristic timescales of evolving bifurcations, along with an analytical linear model. After providing a definition of the bifurcation timescale, this part explores how the velocity with which bifurcations evolve depend on the bifurcation geometry and the flow conditions of the upstream channel. The resulting values for the bifurcation timescale are then compared with those of migrating bars and hydrological cycles. Lastly, Part iv jumps into the world of suspended-load bifurcations, looking at how water and sediments split at the bifurcations in the Wax Lake Delta according to field data and numerical analyses. The insights provided by this case study are then further explored by means of a two-dimensional numerical model of a simple bifurcation with a variable planform configuration, which is employed to understand if and how channel width, bathymetric steps and branching angle affect the division of water and suspended sediments.

Part II

AVULSIONS IN RIVER BIFURCATIONS

ABSTRACT

River bifurcations are constituent components of multi-thread fluvial systems, playing a crucial role in their morphodynamic evolution and the partitioning of water and sediment. Although many studies have been directed at exploring bifurcation dynamics, the conditions under which avulsions occur, resulting in the complete abandonment of one branch, are still not well understood. To address this knowledge gap, we develop a novel 1D numerical model, based on existing nodal point relations for sediment partitioning, which allows for the simulation of the morphodynamic evolution of a free bifurcation. Model results show that when the discharge asymmetry is so high that the shoaling branch does not transport sediments (partial avulsion conditions) the dominant branch undergoes significant degradation, leading to a higher inlet step between the bifurcates and further amplifying the discharge asymmetry. The degree of asymmetry is found to increase with the length of the downstream channels, to the point that when they are sufficiently long, the shoaling branch is completely abandoned (full avulsion conditions). To complement our numerical findings, we also formulate a new analytical model that is able to reproduce the essential characteristics of the partial avulsion equilibrium, which enables us to identify the key parameters that control the transition between different configurations. In summary, this research sheds light on the fundamental processes that drive avulsion through the abandonment of river bifurcations. The insights gained from this study provide a foundation for further investigations and may offer valuable information for the design of sustainable river restoration projects.

The content of this part is published as a research article in the journal Earth Surface Dynamics. Reference: Barile, G., Redolfi, M., and Tubino, M.: Analysis of autogenic bifurcation processes resulting in river avulsion, Earth Surf. Dynam., 12, 87–103, https://doi.org/10.5194/esurf-12-87-2024, 2024.

4 INTRODUCTION

Bifurcations constitute essential geomorphic elements of a variety of fluvial systems, such as braiding rivers and deltas. The morphodynamic evolution of these systems strongly depends on the water and sediment partitioning set by the bifurcation node, which in turn is determined by the reach-scale morphodynamic processes occurring in the three branches connected by the bifurcation node. Understanding these processes is therefore key to foresee the behaviour of multi-thread systems across temporal scales, as well as to design sustainable river restoration projects (Habersack & Piégay, 2007).

Among the morphodynamic processes that occur at bifurcations, the partial or complete abandonment of one of the bifurcates is of crucial importance. This event, which leads to the diversion of the majority or all of the incoming water and sediment discharges towards one of the two bifurcates, can be considered as one of the possible styles of river avulsions, such as "soft" or "choking" avulsions (Edmonds et al., 2011; Leddy et al., 1993). These processes have been shown to play a major role in the evolutionary trajectories of braiding networks (Ferguson, 1993), lowland rivers (Slingerland & Smith, 2004), river deltas (Salter et al., 2018) and alluvial fans (Field, 2001), as they can cause shifts in evolving morphologies and suddenly modify the flooding risk and water resource availability in the downstream areas. Moreover, a clear understanding of the conditions that can ensure the long-term preservation of bifurcating systems is also crucial for the effective implementation of river interventions aimed at recovering the eco-morphological quality of river ecosystems, thus reducing the need for intensive maintenance.

Although many studies have been directed at exploring the possible long-term states of bifurcations, little is yet known about the conditions for which avulsions occur during the transient stage of an evolving bifurcation. Among others, 1-D approaches proved to be very effective in analysing the key mechanisms that govern water and sediment partitioning at bifurcation nodes. These studies stemmed largely from the analytical model developed by Bolla Pittaluga et al. (2003), hereafter referred to as BRT, where a quasi-2D physically-based nodal relationship was used to describe the sediment partitioning at the node.

The BRT model was originally formulated to analyse the dependence on the parameters of the upstream flow of the long-term equilibrium states of a "free" bifurcation (i.e. in the absence of external factors influencing the morphodynamic processes occurring at the node). The model was further extended to include the effects of migrating bars (Bertoldi et al., 2009), tides (Ragno et al., 2020), curvature in the upstream channel (Kleinhans et al., 2012), slope advantage between the branches (Redolfi et al., 2019), and downstream effects generated by prograding branches (Salter et al., 2018).

The main outcome of the BRT model, later confirmed by the experimental results of Bertoldi and Tubino (2007), is the occurrence of two distinct regimes, depending on the values of the half-width to depth ratio β (hereafter referred to as "aspect ratio") and the Shields stress θ of the upstream flow. Specifically, for low values of the aspect ratio β the model only admits of one stable equilibrium solution, in which water and sediments are partitioned evenly by the bifurcation node; in other words, the only equilibrium state of the bifurcation is "balanced". When the aspect ratio β exceeds a critical threshold, the balanced solution becomes unstable and the system admits of two stable, antisymmetric and unbalanced equilibrium configurations. In these unbalanced equilibrium states, both branches are morphodynamically active, i.e. they have a non-negligible transport capacity. As highlighted by Redolfi et al. (2016),

the critical aspect ratio is found to coincide with the resonant value that discriminates between prevailing upstream or downstream propagation of morphological changes (Zolezzi & Seminara, 2001), which reveals the close connection between the dynamics of free bifurcations and the framework of 2-D morphodynamic influence.

However, when further increasing the value of β a second threshold appears, beyond which all stable equilibrium states identified by the BRT model are characterized by a branch with vanishing transport capacity (see Figure 4.1). These states correspond to bifurcations in which one of the two branches is morphodynamically inactive, thus more likely to be abandoned as the bifurcation evolves. Under these conditions the theoretical predictions based on the BRT model are no longer suitable, as the model assumes that both branches are able to adjust their bed slope to a prescribed equilibrium value, which is clearly not possible for the channel that is no longer transporting sediments. The question then arises on whether in this condition the bifurcation can still attain an equilibrium state, and to what extent such state differs from that predicted by the BRT model. To address this question, an evolutionary model is required to trace the trajectory of a bifurcation starting from a nearly-balanced initial state.

In the past two decades, many authors attempted at investigating the transient behaviour of bifurcations belonging to different fluvial environments, though most of these studies were focused on the effect of external forcing factors. For example, Salter et al. (2018) developed a numerical model to study the transient behaviour of bifurcations with prograding branches, considering suitable initial and boundary conditions for reproducing the evolutionary trajectories of bifurcations in depositional environments. Using a similar approach, Iwantoro et al. (2022) studied the effect of tides on the stability of bifurcations by properly varying the downstream boundary conditions. Other evolutionary models of bifurcations available in the literature were tailored to specific case studies, such as bifurcations located downstream a reservoir (Mendoza et al., 2022) and longitudinal training walls in presence of alternate bars in the upstream channel (Le, Crosato, Mosselman, & Uijttewaal, 2018).

The stability of equilibrium states of free bifurcations was indeed studied by Edmonds and Slingerland (2008). However, their analysis was limited to specific deltaic environments in which both branches of the bifurcation were always morphodynamically active. On the contrary, in some of the 3-D numerical simulations performed by Kleinhans et al. (2008) all the incoming solid discharge was steered towards one of the two downstream branches. Analysing these simulations, the authors highlighted the limited capability of the BRT model – both in the original version and with the modifications proposed in their study – to correctly predict the equilibrium value of the water discharge asymmetry of the bifurcation. They specifically showed that bifurcations can display a much higher degree of asymmetry than that foreseen by BRT. Although the simulations considered a bifurcation with a curved upstream channel, thus introducing an external forcing in the model, this study highlighted the important role that the transient behaviour may have in determining the long-term equilibrium state of a bifurcation.

There is therefore a lack of knowledge about the transient behaviour of a "free" bifurcation and about the possible existence of an autogenic mechanism that may lead to the partial or complete abandonment of a branch. In this work, we aim at analysing the transient behaviour of an initially balanced bifurcation that spontaneously evolves over time. To this purpose, we employ a novel 1D numerical model that relies on the BRT relationship for sediment partitioning at the bifurcation node and accounts for the morphodynamic evolution of the three branches composing the bifurcation. By analysing the model outputs, we firstly outline the evolutionary processes that lead the system to reach its long-term, unbalanced equilibrium configuration. Secondly, we show how model results vary considerably according to the aforementioned regions of the BRT model parameter space, displayed in Figure 4.1. Specifically, we show how the bifurcation may evolve towards considerably more unbalanced

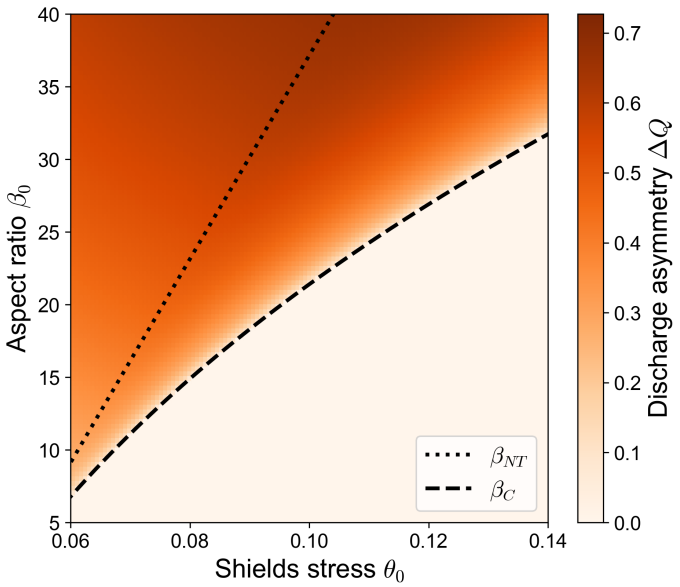


Figure 4.1: Regions of the parameter space identifying different types of equilibrium solutions of river bifurcations computed by means of the BRT model (Bolla Pittaluga et al., 2003) for different combinations of the aspect ratio β_0 and Shields stress θ_0. The dashed line indicates the critical aspect ratio β_C, which separates the region where the balanced equilibrium configuration is stable (lower right region of the plot) from the region where only unbalanced equilibrium configurations are stable (upper left portion of the plot). The dotted line indicates the no-transport aspect ratio β_{NT}: when $\beta_0 \geqslant \beta_{NT}$, the BRT model predicts a vanishing transport capacity in the shoaling branch. Darker shades indicate larger values of the equilibrium discharge asymmetry ΔQ, defined as the difference in the water discharges flowing in the bifurcates, scaled by the incoming discharge.

equilibrium states than those foreseen by the BRT model, including those in which one branch is completely abandoned. Lastly, we formulate a simple analytical model to characterize this new category of equilibrium states.

5 METHODS

5.1 FORMULATION

We consider a "free" bifurcation consisting of three branches, each characterized by a rectangular cross-section and fixed banks. The widths of the bifurcates b and c are assumed to be both equal to half the width of the upstream branch a. The upstream channel is fed by constant liquid (Q_0) and solid (Q_{s0}) discharges, while at the outlet of the downstream branches b and c a constant water-surface elevation h_d is set. At the bifurcation node we also impose the water discharge balance and an equal water level for the three branches. Lastly, we employ the quasi-2D two-cell nodal condition proposed by Bolla Pittaluga et al. (2003) to compute the transverse exchange of sediments at the node.

To model the morphodynamic evolution of the bifurcation over time, we solve numerically the gradually varied flow equation and the Exner equation along the three branches, according to a quasi-steady approach. As initial conditions we consider a balanced bifurcation, where water and sediments are partitioned equally among the downstream branches. After applying a small perturbation on the transverse bed slope between the branches, we then let the bifurcation evolve spontaneously over time.

Computation of hydrodynamic conditions and morphological evolution along the branches

The hydrodynamic conditions are evaluated by assuming that riverbed changes are much slower than flow adaptation, which implies that the solution for the liquid phase can be decoupled from that of the solid phase. The constancy of the water supply then implies that a unique value of water discharge can be considered for each branch. The water-surface profile computation along each branch is then performed by integrating in the x-direction the gradually varied flow equation:

$$\frac{dD}{dx} = \frac{S - j(Q, D)}{1 - Fr^2(Q, D)}, \tag{5.1}$$

where D is the water depth, S is the local bed slope, j is the energy gradient, and Fr is the Froude number. Both j and Fr are computed as functions of the water discharge Q and of the water depth D as:

$$j = \left(\frac{Q}{W C \sqrt{g} D^{3/2}} \right)^2, \tag{5.2a}$$

$$Fr = \frac{Q}{W \sqrt{g} D^{3/2}}, \tag{5.2b}$$

where W is the width of the branch, g is the gravity acceleration and C is the dimensionless Chézy coefficient, which is here for simplicity considered to be independent of the water depth and known a priori.

Integrating Equation (5.1) along the downstream bifurcates requires the knowledge of the respective flow rates, which we compute by means of an iterative procedure that relies on the assumption of equal surface elevation at the bifurcation node. This procedure is similar to that employed by previous models (e.g., Kleinhans et al., 2008), and will be later described in this section.

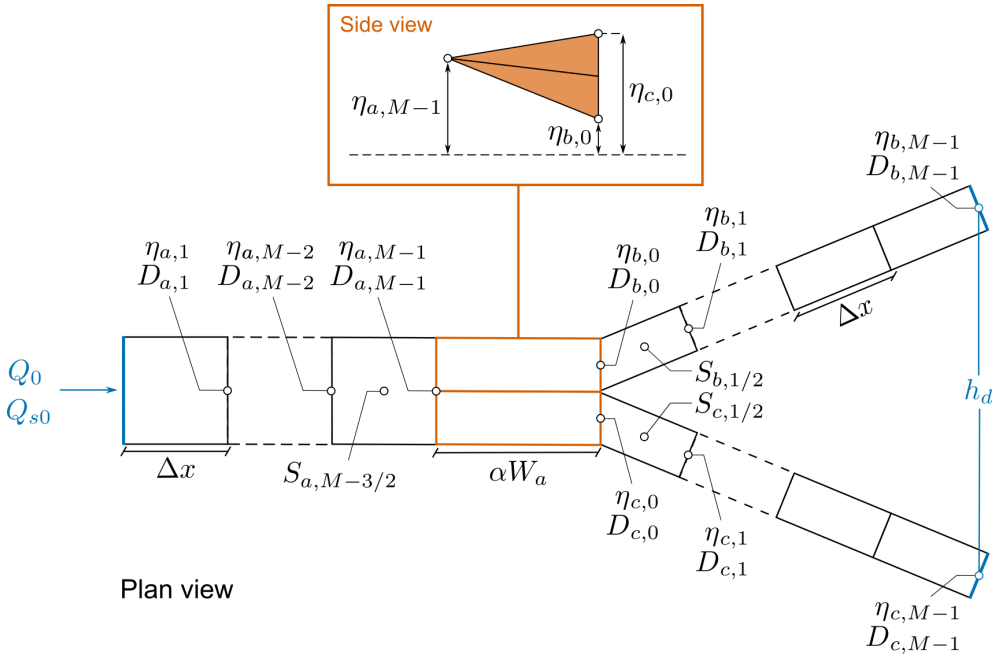


Figure 5.1: Spatial discretization of water depth D, bed elevation η and bed slope S along the channels and within the nodal bifurcation cells. The side view illustrates in detail the triangular step scheme adopted for the bed elevation profiles of the node cells, whose length is given by the product of the order-1 parameter α and the upstream channel width W_a. Q_0 and Q_{s0} represent the water and sediment supply, while h_d stands for the fixed water level at the downstream end of branches b and c.

Once the water discharge and the water depth along the three branches have been determined, the evolution over time of the bed profile is computed by integrating in time the Exner equation, which for channels having a rectangular cross-section and constant width is written in the form:

$$(1-p)\frac{\partial \eta}{\partial t} = -\frac{1}{W}\frac{\partial Q_s}{\partial x}, \tag{5.3}$$

where t is the time, η the local bed elevation, p the bed porosity, and Q_s the sediment flux. The latter is expressed as:

$$Q_s = W\sqrt{g\Delta D_s^3}\,\Phi(\theta), \tag{5.4}$$

where Δ is the relative submerged weight of sediments, D_s is the median grain size, and $\Phi(\theta)$ is the dimensionless transport capacity per unit width. The latter is evaluated by means of a suitable transport formula (e.g., Meyer-Peter & Müller, 1948; Parker, 1978) as a function of the Shields stress θ, defined as:

$$\theta = \frac{jD}{\Delta D_s}. \tag{5.5}$$

Water surface gradient and transverse solid discharge at the node cells

Following the approach proposed by Bolla Pittaluga et al. (2003), we model the last reach of the upstream channel a by means of two node cells, which are allowed to exchange water and sediments in the transverse direction. The length of the node cells is estimated as αW_a, where α is an order-1 parameter for which different values have been proposed in the literature, as discussed by Redolfi (2023). For these node cells, the mathematical formulation must be amended to suitably represent the quasi-2D scheme introduced by BRT to account for the sediment transport redistribution driven by flow exchange and transverse bed slope.

The first question that arises is how to schematize the elevation gap between the two cells. Here we integrate the gradually varied flow equation and the Exner equation by considering the"triangular step" scheme represented in Figure 5.1, i.e. by assuming that the bed elevation varies linearly along each node cell.

A second issue concerns how the water-surface profile is computed, and specifically how to determine the water level at the inlet of the nodal cells, which sets the boundary condition for the computation of the backwater profile along the upstream channel a. Most existing 1D models (e.g., Iwantoro et al., 2022; Kleinhans et al., 2008) solved this problem by assuming a constant water surface elevation throughout the bifurcation cells. However, considering that the nodal cells extend over several channel widths, this may be not fully appropriate, especially in relatively steep channels. To overcome this limitation, the difference in water level between the upstream and downstream ends of the node cells is calculated by integrating Equation (5.1) along the node cells themselves, assuming a composite cross-section made of two halves with different bed elevation. The resulting formula for the energy gradient j reads:

$$j = \left(\frac{Q_a}{C\sqrt{g} W_a \dfrac{D_{ab}^{3/2} + D_{ac}^{3/2}}{2}} \right)^2 , \tag{5.6}$$

where Q_a ($= Q_0$) is the water discharge, D_{ab} and D_{ac} stand for the water depths of the two halves of the cross-section, and the Froude number is computed using the average water depth, i.e. $D = (D_{ab} + D_{ac})/2$.

A third problem to be addressed regards the computation of the sediment fluxes at the cell boundaries and the subsequent update of the bed elevation of the node cells. The latter is achieved by means of the Exner equation, which we use in integrated form for each node cell. To compute the transverse exchange of sediments between the node cells we employ the nodal relationship proposed by BRT, which reads:

$$Q_{sy} = Q_{sa} \left(\frac{Q_b - Q_c}{2Q_a} - \frac{2\alpha r}{\sqrt{\theta_a}} \frac{\eta_{bN} - \eta_{cN}}{W_a} \right), \tag{5.7}$$

where r is an empirical coefficient that quantifies the effect of transverse bed slope (e.g., Baar et al., 2018), Q_{sa} and θ_a are the sediment flux and the Shields stress of the incoming flow, η_{bN} and η_{cN} are the average bed elevations of the two node cells, and Q_b and Q_c are the water discharges flowing in the downstream branches. The transverse flux of sediments Q_{sy} is then used to compute the evolution of the node cell elevation over time. To do so, we integrate the Exner equation (5.3) in space over the node cells. By considering the aforementioned "triangular step" geometry, the resulting equation for the node cell b reads:

$$(1-p)\frac{d\eta_{bN}}{dt}\frac{\alpha W_a^2}{2} + Q_{sb} - \frac{Q_{sa}}{2} - Q_{sy} = 0, \tag{5.8}$$

where Q_{sb} is the sediment flux entering the channel b. An analogous equation is obtained for the node cell c.

5.2 NUMERICAL SCHEME

In order to integrate the gradually-varied flow equation (5.1) and the Exner equation (5.3) over our domain, we discretize each of the three branches composing the bifurcation by means of M nodes. As shown in Figure 5.1, the bed elevation η, the water depth D, the Shields parameter θ and the solid discharge Q_s are all defined at each node, identified by means of the index i. On the contrary, the longitudinal bed slope S is defined between each couple of subsequent nodes.

In all simulations performed, the flow conditions along the three branches is subcritical at any point in time and space. Consequently, we integrate the gradually varied flow equation in upstream direction and use a backward difference scheme for the spatial derivative in the Exner equation, according to an upwind approach. In the following, some details about the integration procedures adopted in the numerical scheme are provided.

To solve numerically Equation (5.1) between two adjacent nodes, we first discretize the derivative of water depth D and bed elevation η as:

$$\begin{aligned} \frac{dD}{dx} &= \frac{D^n_{k,i+1} - D^n_{k,i}}{\Delta x}, \\ S = S^n_{k,i+1/2} &= \frac{\eta^n_{k,i} - \eta^n_{k,i+1}}{\Delta x}, \end{aligned} \qquad \begin{cases} k = a, b, c \\ i = 0..M-1 \end{cases} \tag{5.9}$$

where $\eta^n_{k,i}$ stands for the bed elevation at node i at the generic time step n, and Δx is the prescribed grid size.

We then solve Equation (5.1) in upstream direction by means of a fourth-order Runge-Kutta scheme, computing the water depth at the node i given the water depth at the subsequent node $i+1$. The integration procedure starts from the water depth at the downstream end of branches b and c, which is computed as the difference between the prescribed water level h_d and the bed elevation at the last node of each branch resulting from the previous iteration. It is worth noting that, according to the adopted quasi-steady approach, we use the bed slope S computed at the previous time step n to compute the water depth along each branch at the new time step $n+1$.

The integration of the gradually varied flow equation eventually returns the water depths at the first nodes of branches b and c (i.e. $D_{b,0}$ and $D_{c,0}$). If the condition of equal water level at the bifurcation node isn't met, Equation (5.1) is iteratively integrated along the branches b and c until the condition is satisfied. Iterations are performed over the water discharge flowing in one branch according to the Newton-Raphson method. At each iteration, the discharge flowing in the other branch is retrieved from water mass continuity. The water discharges flowing in branches b and c resulting from these iterations are then used to compute the final water-surface profiles along the bifurcates.

To update the bed profile along the three branches, we integrate the Exner equation (5.3) in time, using a time step Δt computed according to a CFL condition and an upwind scheme to discretize the spatial derivative of the sediment flux Q_s:

$$\eta^{n+1}_{k,i} = \eta^n_{k,i} - \frac{1}{(1-p)W_k}\frac{\Delta t}{\Delta x}\left(Q^{n+1}_{sk,i} - Q^{n+1}_{sk,i-1}\right) \qquad \begin{cases} k = a, b, c \\ i = 1..M-1 \end{cases} . \tag{5.10}$$

Note that Equation (5.10) is used to update the bed elevation of all nodes except the first node of each channel. The first node of channel a is updated by using a ghost cell, while the bed elevation at the inlets of branches b and c are updated by integrating Equation (5.8). We then compute the transverse sediment flux Q_{sy} flowing from one node cell to the other according to Equation (5.7). Consistently with the discretization of the node cells represented in Figure 5.1, at any time step n the average bed elevations of the node cells η_{bN} and η_{cN} are computed as

$$\eta_{bN} = \frac{\eta^n_{a,M-1} + \eta^n_{b,0}}{2}, \qquad \eta_{cN} = \frac{\eta^n_{a,M-1} + \eta^n_{c,0}}{2}. \tag{5.11}$$

Furthermore, the Shields stress θ_a and solid discharge Q_{sa} corresponding to the incoming flow are retrieved from the last node of the upstream channel a. The resulting expression used in the numerical scheme to compute Q_{sy} at the time step $n+1$ reads:

$$Q^{n+1}_{sy} = Q^{n+1}_{sa,M-1}\left(\frac{Q^{n+1}_b - Q^{n+1}_c}{2Q_a} - \frac{\alpha r}{\sqrt{\theta^{n+1}_{a,M-1}}}\frac{\eta^n_{b,0} - \eta^n_{c,0}}{W_a}\right). \tag{5.12}$$

The update of the bed elevation of a node cell - say, cell b - thus returns:

$$\eta_{b,0}^{n+1} = \eta_{b,0}^{n} + \eta_{a,M-1}^{n} - \eta_{a,M-1}^{n+1} - \frac{4\Delta t}{(1-p)\alpha W_a^2}\left(Q_{sb,0}^{n+1} - Q_{sy}^{n+1} - \frac{Q_{sa,M-1}^{n+1}}{2}\right), \tag{5.13}$$

while an analogous formula is used to update the bed elevation of cell c.

6 RESULTS

The numerical model described in chapter 5 is here used to explore the full range of conditions depicted in Figure 4.1, for different values of the length of the downstream bifurcates L. Each simulation is characterized by a given set of boundary conditions, namely the water (Q_0) and sediment (Q_{s0}) discharges supplied to the upstream channel and the water level at the downstream end of the branches h_d. We note that when the values of the upstream width W_a, grain size D_s and Chézy coefficient C are specified, the water and sediment supply completely determine the reference uniform flow and sediment transport state that characterizes the initial configuration in the three branches, namely the values of the flow depth D_0 and the bed slope S_0. For a given length L of the bifurcates, these values also fix the downstream water level h_d with respect to the initial bed level at the node.

Simulation results will be presented in dimensionless form, using the parameters of the initial reference state as scaling quantities. As the Chézy coefficient is assumed to be constant, only two parameters are needed to specify in dimensionless form such reference state, namely its aspect ratio β_0 and Shields stress θ_0, which are prescribed as input values. Following the lead of BRT, we then quantify the degree of asymmetry between the two bifurcates by means of two dimensionless parameters, namely the discharge asymmetry ΔQ and the inlet step $\Delta\eta$, that we define as:

$$\Delta Q = \frac{Q_b - Q_c}{Q_0}, \quad \Delta\eta = \frac{\eta_c - \eta_b}{D_0}, \tag{6.1}$$

where η_b and η_c stand for the bed elevations at the inlets of the downstream branches. Furthermore, we define the average bed elevation $\overline{\eta}$ at the inlet of the bifurcates as:

$$\overline{\eta} = \frac{\eta_b + \eta_c}{2D_0}. \tag{6.2}$$

Finally, we scale the longitudinal coordinate x with the reference flow depth D_0 and the time t with the morphodynamic timescale T_F defined by the Exner equation:

$$T_F = \frac{W_a^2 D_0}{Q_{s0}}. \tag{6.3}$$

As foreseen by the BRT model, in all numerical simulations in which the aspect ratio β_0 is larger than the critical aspect ratio β_C any asymmetric perturbation of the initially balanced bifurcation grows over time. The early stages of these simulations take place according to a well-defined behaviour (later described in this section), which is qualitatively independent of the governing parameters. On the contrary, the long-term state of bifurcations may be of two types depending on the reference conditions of the upstream channel. Specifically, the bifurcation may either reach an equilibrium configuration that corresponds to that foreseen by the BRT model or evolve towards a considerably more asymmetric type of equilibrium state. The latter type of equilibrium configuration occurs when the transport capacity of the branch carrying the smaller portion of the incoming discharge becomes negligible. We term this condition "partial avulsion".

Whether the bifurcation reaches one type of long-term state or the other depends on the dimensionless parameters of the reference state β_0 and θ_0. Specifically, we found that the long-term state of numerical simulations depends on which of the three regions of the $\beta_0 - \theta_0$ space identified by the BRT model (and described in Figure 4.1) the provided values of β_0 and θ_0 belong to. For a given value of θ_0, these regions are identified by the critical aspect ratio β_C and by the value of β_0 for which

the non-dominant branch has no transport capacity at equilibrium according to the BRT model, i.e. the no-transport aspect ratio β_{NT}. If $\beta_C < \beta_0 < \beta_{NT}$, the numerical simulation evolves towards the long-term state predicted by BRT. Conversely, when $\beta_0 \geqslant \beta_{NT}$ a partial avulsion occurs. In the following, the transient behaviour of these two types of simulations are described in detail.

Figure 6.1 shows an example of simulations in which $\beta_C < \beta_0 < \beta_{NT}$, where the system always evolves towards an equilibrium state where both branches actively transport sediments. Since the transport capacity of both branches is non-negligible both during the evolution of the bifurcation and at equilibrium, we will hereafter refer to this category of simulations as "fully active". In this case, the morphodynamic evolution of the bifurcation takes place by means of three distinct evolutionary stages.

In the first stage, the bed elevation gap between the branches - i.e. the "inlet step" defined by BRT - grows over time following an exponential trend. Specifically, while the branch carrying an increasingly larger fraction of the incoming water discharge (the "dominant" branch) undergoes an erosion process, the other branch (the "non-dominant" branch) undergoes a deposition process. As this two opposite processes develop, the bed slopes of the branches don't vary significantly with respect to their initial value S_0. On the contrary, the water discharge asymmetry ΔQ grows exponentially over time (see Figure 6.1). The amplification of the degree of asymmetry of the bifurcation in this stage closely matches that resulting from a linear stability analysis of the system of equations of the BRT model, as recently shown by Ragno (2023).

In the second stage of these simulations, nonlinear effects become dominant as the overall bed elevation and the bed slopes of the branches further evolve. The bed slopes of both branches decrease over time, approaching the equilibrium value foreseen by the BRT model, while the discharge asymmetry ΔQ keeps growing until it reaches a maximum value (see Figure 6.1). In the third stage, after the maximum of ΔQ is reached, the water discharge asymmetry of the bifurcation decreases, showing an upward-concave trend over time, until it reaches its equilibrium value.

It is worth noticing that there is a non-negligible difference between the maximum value of ΔQ reached at the end of the second stage and its long-term equilibrium value. From now on, we will refer to this difference as "overshoot", as the simulated value of ΔQ goes beyond the equilibrium value predicted by the analytical BRT model. The overshoot is due to the morphodynamic evolution of the non-dominant branch: the temporary increase of ΔQ is in fact caused by an excess of deposition with respect to the final state that occurs at the inlet of the branch. This temporary increase of the bed elevation of the non-dominant branch causes a decrease in the water discharge entering that branch, thus increasing the water discharge asymmetry ΔQ. This phenomenon may play an important role in determining the long-term state of the bifurcation, as will be discussed later in this section.

As a result of these processes, the bifurcation eventually reaches a long-term state that matches the equilibrium configuration foreseen by the analytical BRT model. In this equilibrium state, both branches are characterized by uniform flow, with constant water depth and bed slope over their length. Since the widths of the branches are both equal to half the width of the upstream channel, the equilibrium value of the bed slopes must always be lower than the initial bed slope S_0 to ensure the conservation of sediment mass. Under equilibrium conditions, the inlet step ensures that the transverse sediment flux at the node balances the difference between the transport capacities of the downstream branches, as results from the BRT bulk relationship (5.7).

When $\beta_0 > \beta_{NT}$, the evolutionary trajectory of the bifurcation doesn't lead it to reach the equilibrium foreseen by the BRT model as it does for fully active simulations. An example of this type of simulation is represented in Figure 6.2. By comparing the evolution over time of the discharge asymmetry ΔQ of this type of simulations (panel (c) of Figure 6.2) with that of fully active simulations (panel

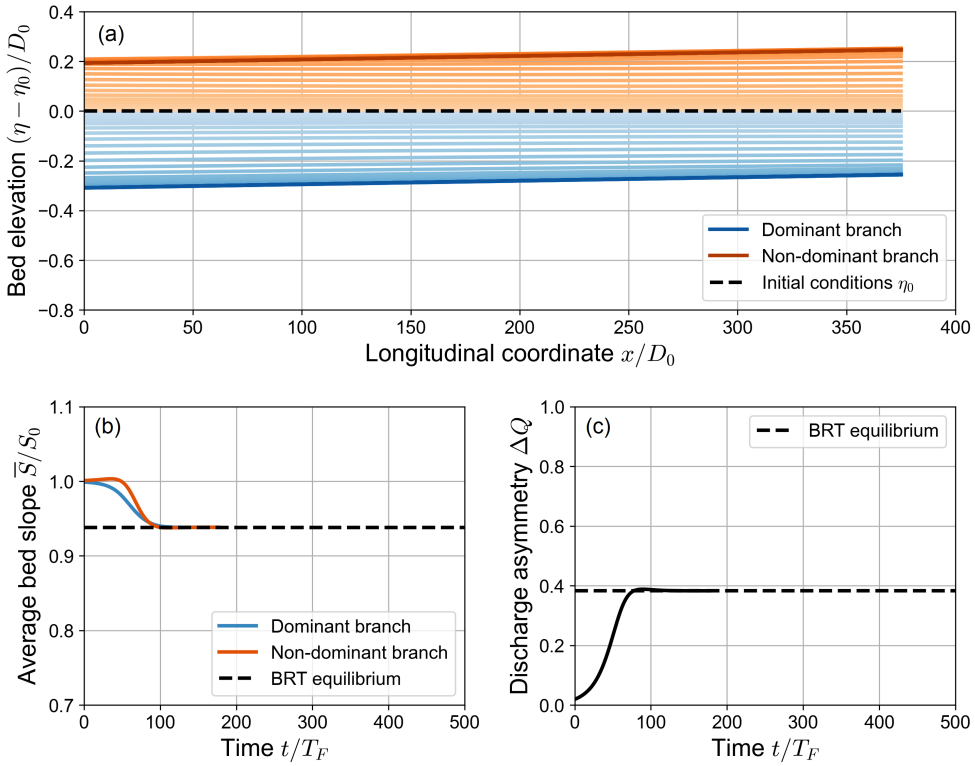


Figure 6.1: Spatial (upper panel) and temporal (lower panels) evolution of a fully active numerical simulation, where the long-term state matches the equilibrium solution of the BRT model ($\beta_0 = 15$, $\theta_0 = 0.07$, $C = 12$, transport formula of Meyer-Peter and Müller, 1948). The upper panel shows the variation over time of the bed elevation profiles with respect to the initial bed profile η_0 (dashed line). Note that both the longitudinal coordinate x and the bed elevation variation $\eta - \eta_0$ are scaled with the reference water depth D_0. The profiles are sampled with a constant time step of $\Delta t/T_F = 4.4$, where T_F is defined as in Equation (6.3). The lower left panel shows the evolution of the average bed slope of the branches, scaled with the initial bed slope S_0. The lower right panel shows the evolution over time of the water discharge asymmetry ΔQ, defined as in Equation (6.1). In both lower panels, the dashed line indicates the equilibrium solution foreseen by the BRT model.

(c) of Figure 6.1), one can see that the first two stages qualitatively resemble each other. However, contrary to fully active simulations, at the end of the second stage of simulations where $\beta_0 > \beta_{NT}$ the transport capacity of the non-dominant branch becomes negligible. As a result, the dominant branch is fed with all the incoming sediment discharge and, most importantly, the non-dominant branch is not able to adjust its bed slope over time any more. After this "freezing" of the bed slope of the non-dominant branch, the water discharge and the average water depth of the dominant branch considerably increase over time, while its bed slope decreases. This leads to an overall degradation of the branch. Since the non-dominant branch is no longer capable of modifying its morphology, this degradation sharply increases the difference in water depth between the branches, as the water level is prescribed to be the same at the inlets of the branches. The discharge asymmetry ΔQ keeps increasing as well, asymptotically reaching a much larger equilibrium value than that foreseen by the BRT model (see Figure 6.2).

At equilibrium, the bed slope of the dominant branch is significantly lower than the equilibrium slope predicted by BRT. On the contrary, the bed slope of the non-dominant branch remains close to the slope S_0 prescribed as initial condition. This is due to the fact that, as in the fully active simulations, the bed slope of both branches doesn't vary significantly in the early evolutionary stages, while the inlet elevation gap grows over time. The equilibrium configurations of the two bifurcates also differ in terms of water-surface profile. While the dominant branch is characterized by uniform flow conditions, the water surface along the non-dominant branch follows an upward-concave profile. Being the transport capacity equal to zero along this branch, the backwater curve doesn't imply an ongoing morphodynamic evolution, and is therefore compatible with an equilibrium condition.

It is worth noticing that the two types of equilibrium configurations described above show a remarkably different dependency on the governing parameters. As shown in Figure 6.3, the equilibrium configuration of a fully active bifurcation (i.e. when $\beta_C < \beta_0 < \beta_{NT}$) doesn't depend on the length of the bifurcates, as foreseen by the BRT model, the resulting asymmetry being mainly governed by the parameters of the reference upstream flow (i.e. the aspect ratio β_0). On the contrary, when a partial avulsion occurs the final configuration also exhibits a sharp dependence on the length of the downstream branches. Specifically, bifurcations with longer branches show a larger discharge asymmetry, a lower bed slope of the dominant branch and – as a result – a larger overall degradation of the dominant branch itself, as shown by the considerably lower values of $\overline{\eta}$. The scenario depicted in Figure 6.3 does not qualitatively change when changing the reference Shields stress θ_0 but for the values of the critical and the no-transport aspect ratio, whose dependence on θ_0 is illustrated in Figure 4.1.

The results of numerical simulations therefore suggest that in the case of a partial avulsion the equilibrium state gets more unbalanced as the dimensionless length of the bifurcates $L^* = L/D_0$ increases. Interestingly, by further increasing the length of the branches the evolution of the bifurcation eventually leads to the complete abandonment of the non-dominant branch. In these cases, which we call "full avulsions", the dominant branch carries all the incoming water and sediment discharges.

Figure 6.3 also shows that the exact value of β_0 above which partial avulsions occur in the numerical simulations is slightly lower than the threshold value β_{NT} computed analytically by means of the BRT model (see dotted lines in the figure). This offset is due to the overshoot phenomenon: if the temporary decrease in the water discharge flowing in the non-dominant branch is large enough, the transport capacity of the branch may drop to zero, thus causing a partial avulsion. Overall, the dependence of the amplitude of the overshoot on the length of the bifurcates is rather weak, as shown by Figure 6.4a. Thus, the threshold for β_0 for which a partial avulsion occurs in the numerical simulations is almost independent of the length of downstream branches.

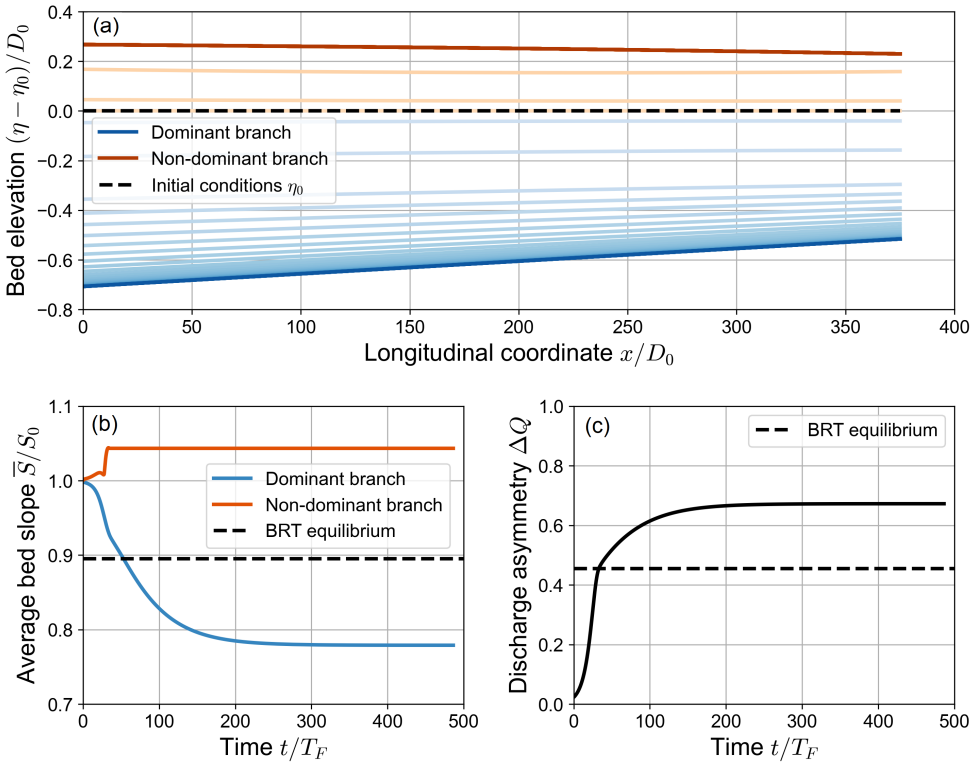


Figure 6.2: Spatial (upper panel) and temporal (lower panels) evolution of a numerical simulation where a partial avulsion occurs ($\beta_0 = 20$, $\theta_0 = 0.07$, $C = 12$, transport formula of Meyer-Peter and Müller, 1948). The upper panel shows the variation over time of the bed elevation profiles with respect to the initial bed profile η_0 (dashed line). Note that both the longitudinal coordinate x and the bed elevation variation $\eta - \eta_0$ are scaled with the reference water depth D_0. The profiles are sampled with a constant dimensionless time step of $\Delta t/T_F = 12.2$, where T_F is defined as in Equation (6.3). The lower left panel shows the evolution of the average bed slope of the branches, scaled with the initial bed slope S_0. The lower right panel shows the evolution over time of the water discharge asymmetry ΔQ, defined as in Equation (6.1). In both lower panels, the dashed line indicates the equilibrium solution foreseen by the BRT model.

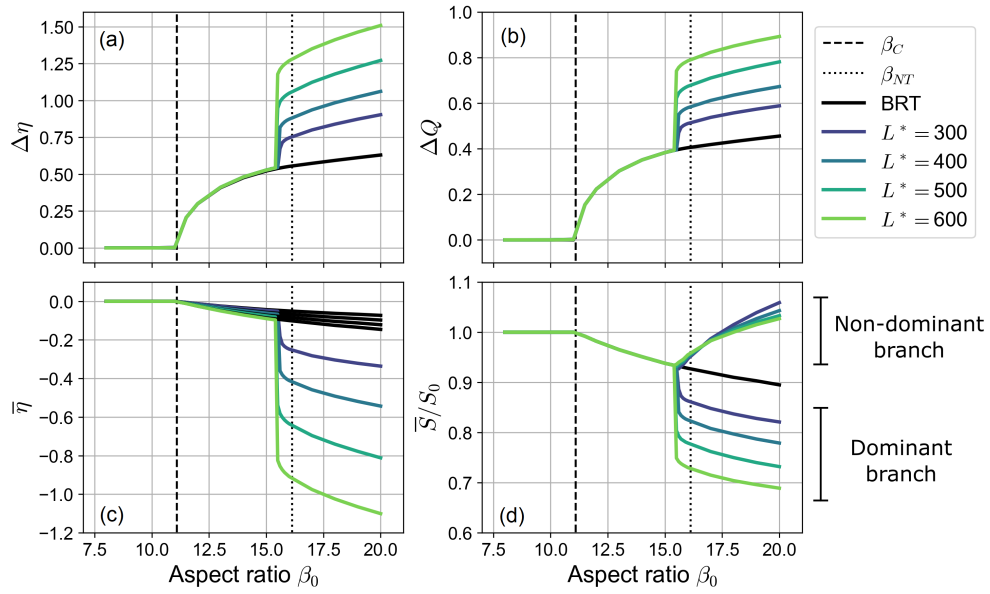


Figure 6.3: Long-term equilibrium states of a free bifurcation: the four panels show the dependence on the aspect ratio β_0 of the inlet step $\Delta\eta$, the water discharge asymmetry ΔQ, the average bed elevation at the inlets of the branches $\overline{\eta}$ and of the bed slope averaged over the branch $\overline{S}$, for different values of the non-dimensional length of the bifurcates $L^* = L/D_0$ ($\theta_0 = 0.07, C = 12$, transport formula of Meyer-Peter and Müller, 1948). Solid black lines indicate the equilibrium solutions computed by means of the BRT model. Dashed and dotted lines represent the critical aspect ratio β_C and the no-transport aspect ratio β_{NT}, respectively.

Figure 6.4b illustrates how the system evolves in time towards conditions of partial avulsion when $\beta_0 > \beta_{NT}$. After the initial phase, in which the discharge asymmetry weakly depends on the length L^*, an abrupt change is observed as ΔQ exceeds ΔQ_{BRT}, when one of the bifurcates becomes no longer able to transport sediments. After this point, the evolution significantly depends on L^*, with longer branches leading to a larger discharge asymmetry and requiring a longer time to reach the final equilibrium configuration.

Based on the results of numerical simulations, we can therefore identify different categories of the long-term equilibrium state of a free bifurcation in the $\beta_0 - L^*$ plane, as reported in Figure 6.5. When β_0 is lower than the critical aspect ratio β_C, all stable equilibrium states of the bifurcation are balanced, i.e. show an even partitioning of water and solid discharge. Instead, when $\beta_0 > \beta_C$ the bifurcation evolves towards a stable and unbalanced equilibrium state, where both branches effectively carry sediments ("fully active" simulations). When β_0 exceeds a second threshold β_{NT}, which is found numerically to be slightly lower than the no-transport threshold predicted analytically, a partial avulsion occurs during the evolution of the bifurcation. In this case, the equilibrium state can be of two types, depending on the value of the dimensionless length of the bifurcates L^*. For lower values of L^*, the non transporting branch remains open, although the water discharge asymmetry is much larger than that resulting in the fully active region and also depends on the length of the branches, while it keeps a similar dependency on β_0. At larger L^* values a full avulsion occurs, and the non-dominant branch is completely abandoned. As suggested by Figure 6.5, the threshold value of L^* for which a full avulsion occurs is weakly dependent on the upstream aspect ratio β_0.

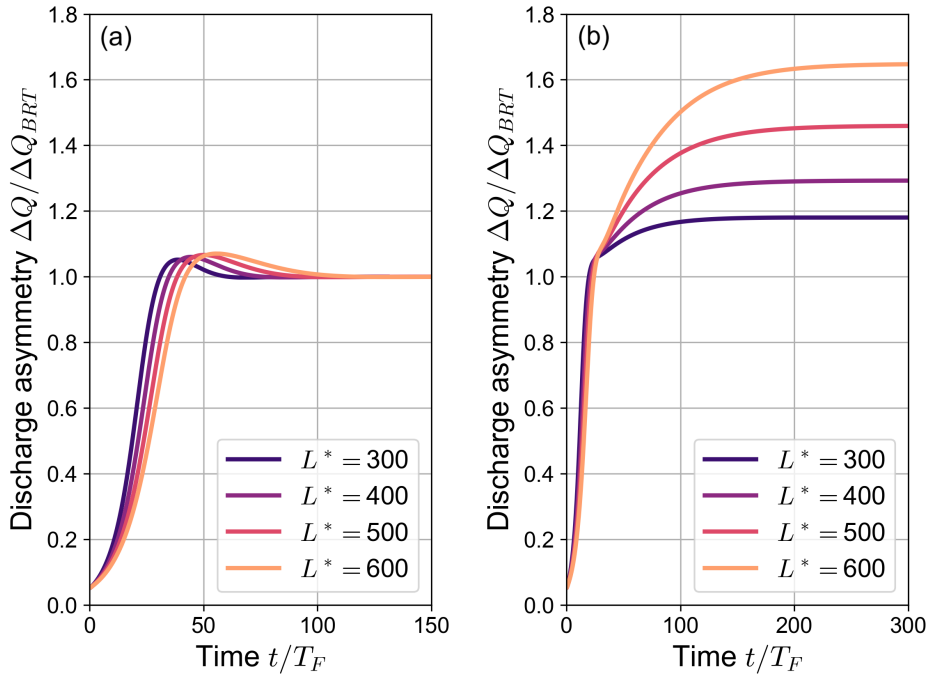


Figure 6.4: The variation over time of the ratio between the simulated discharge asymmetry ΔQ and the equilibrium value foreseen by the BRT model ΔQ_{BRT}, for different values of the dimensionless length of the bifurcates $L^* = L/D_0$: (a) $\beta_0 = 18 < \beta_{NT}$; (b) $\beta_0 = 25 > \beta_{NT}$ ($\theta_0 = 0.07$, $C = 12$, transport formula of Parker, 1978). The time t is made dimensionless by means of the Exner timescale T_F, defined as in Equation (6.3).

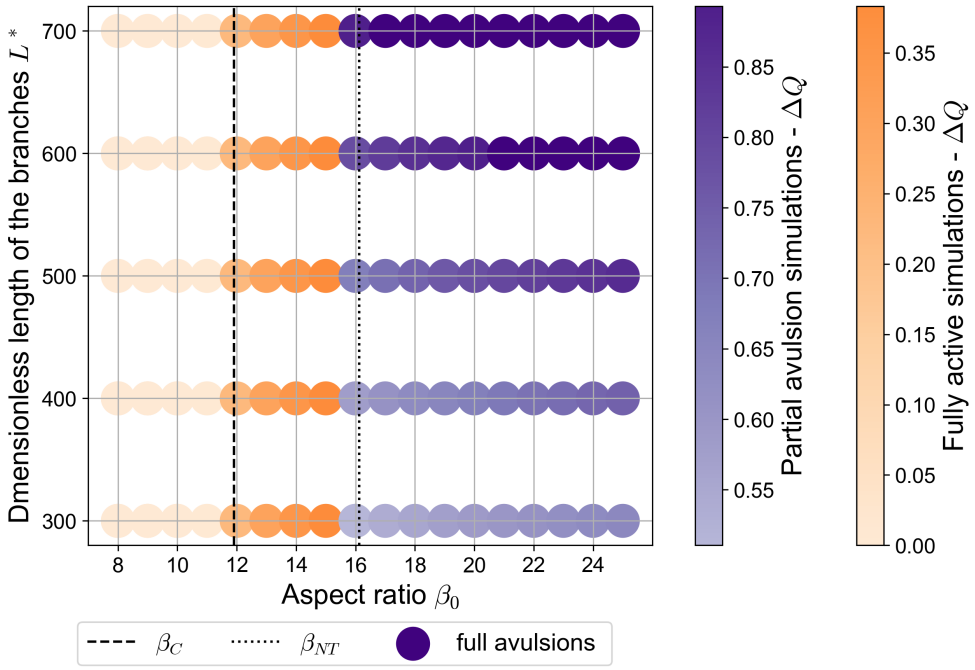


Figure 6.5: Equilibrium configurations of a free bifurcation for different values of the dimensionless length of the downstream branches L^* and of the aspect ratio β_0 ($\theta_0 = 0.07$, $C = 12$, transport formula of Meyer-Peter and Müller, 1948). Each point corresponds to a single numerical simulation. Reddish colours indicate fully active states, where the discharge asymmetry ΔQ predicted by BRT is attained. Bluish tones indicate partial avulsion states, in which one of the bifurcates does not transport sediments, while dark blue dots indicate states where one of the branches in completely abandoned ($\Delta Q \simeq 1$, full avulsions). Note that the value of the reference Shields stress is the same for all simulations.

7 SIMPLIFIED EQUILIBRIUM MODEL FOR PARTIAL AVULSIONS

The results of numerical simulations reported in the previous section suggest that under conditions of partial avulsion the long-term equilibrium state of a free evolving bifurcation significantly differs from that predicted by the analytical BRT model. Nonetheless, in this section we show how the equilibrium value of the discharge asymmetry can be still predicted by a simple, analytical model by introducing appropriate hypotheses that are supported by information retrieved from numerical simulations.

We consider the long-term state of an initially balanced bifurcation depicted in Figure 7.1, where the shoaling branch c is not able to effectively transport sediments. As in the BRT model, the upstream water (Q_0) and sediment (Q_{s0}) supplies are given, while the water level at the downstream end of the branches h_d is fixed and defined by the reference water depth D_0. However, in this case two additional pieces of information are required to close the mathematical formulation of the equilibrium state, namely the slope S_c and the inlet bed elevation η_c of the shoaling branch. In fact, their actual value results from the evolutionary process of the bifurcation, being determined when the transport capacity vanishes. Moreover, the sediment transport partition at the node takes a simple form, as all the incoming solid discharge is conveyed by the dominant branch.

Under fully active conditions, both downstream branches evolve towards a uniform flow and sediment transport configuration, in which the water surface and bed elevation profiles are straight and parallel to each other. This implies that the equilibrium bed slopes are the same ($S_b = S_c$), as assumed by BRT. However, this is no longer the case under partial avulsion conditions, because when the transport capacity of the shoaling branch vanishes its bed slope S_c remains constant over time, while the slope S_b of the dominant branch continues to evolve until equilibrium is attained. By looking closely at the transient behaviour of the shoaling branch displayed by numerical simulations, we may observe that the overall homogeneous deposition occurring along the branch causes it to stop transporting sediments before its bed slope changes appreciably. Therefore, numerical results suggest that the slope of the shoaling branch does not vary significantly with respect to the initial condition, so that it is reasonable to assume that, at equilibrium:

$$S_c = S_0. \tag{7.1}$$

As can be seen in panel (d) of Figure 6.3, the error we make by using Equation (7.1) is relatively small, namely of order $10^{-2} S_0$.

Another key difference of partial avulsions with respect to the fully-active configurations is the computation of the transverse flux of sediments at the node Q_{sy}. Under fully-active conditions Q_{sy} is computed by means of the BRT bulk relationship (5.7), and depends on both the discharge asymmetry and the bed elevation gap between the branches. Under conditions of partial avulsion, the equilibrium value of the transverse flux of sediment at the node is always equal to half the incoming sediment discharge, thus granting solid mass continuity in the node cells, regardless of the bed elevation gap between the branches. Thus, the transverse bed slope adjusts in order to satisfy the relationship between the discharge asymmetry and Q_{sy} defined by Equation (5.7). On the other hand, the bed elevation gap between the downstream branches – i.e. the inlet step $\Delta\eta$, as defined in Equation (6.1) – is entirely governed by the degradation of the dominant branch that leads it to reach its equilibrium bed slope. Thus, the node cells and the inlet step evolve according to two different mechanisms, and do not coincide anymore as they do in fully-active conditions. As a result, the system gains a degree of freedom.

To replace the missing condition, we assume that, when the transport capacity of the non-dominant branch vanishes, the inlet step $\Delta\eta$ equals the inlet step $\Delta\eta_{BRT}$ foreseen by the BRT model. This assumption is consistent with the numerical results, since the first stages of partial avulsion and fully active simulations evolve in a very similar manner. This allows us to compute the bed elevation η_c at the inlet of the shoaling channel c, defined with respect to the initial bed elevation, as

$$\eta_c = \frac{\Delta\eta_{BRT}}{2} D_0. \tag{7.2}$$

We also note that the variations of discharge asymmetry after the freezing of the shoaling branch imply that flow conditions do not keep uniform throughout the channel. Specifically, the reduction of the water discharge Q_c and the fixed water surface elevation at the downstream end of both branches produce an upward concave water-surface profile in the shoaling branch, as illustrated in Figure 7.1. Nonetheless, when the branches are longer than the backwater length, it is still possible to assume that in the upstream part of the shoaling branch the flow keeps nearly uniform. This allows us to consider the following uniform flow relations for both branches:

$$Q_b = W_b C \sqrt{g S_b} D_b^{3/2}, \tag{7.3a}$$

$$Q_c = W_c C \sqrt{g S_c} D_c^{3/2}, \tag{7.3b}$$

where the water fluxes Q_b and Q_c can be expressed as functions of the discharge asymmetry ΔQ by considering the water mass conservation:

$$\frac{Q_b}{Q_0} = \frac{1+\Delta Q}{2}, \quad \frac{Q_c}{Q_0} = \frac{1-\Delta Q}{2}. \tag{7.4}$$

By substituting Equation (7.2) into the nodal condition that sets the same water surface elevation at the inlets of branches b and c, we obtain:

$$D_b - D_c = \eta_c - \eta_b = \frac{\Delta\eta_{BRT}}{2} D_0 - \eta_b, \tag{7.5}$$

where the bed elevation at the inlet of the dominant branch η_b is given by the following geometrical relation, illustrated by Figure 7.1:

$$\eta_b = -(S_0 - S_b)L - (D_b - D_0). \tag{7.6}$$

The system of equations is finally completed by the sediment mass conservation, which under partial avulsion conditions becomes particularly simple, as the entire sediment supply is carried by the dominant branch b:

$$\Phi(\theta_b) = \Phi(\theta_0)\frac{W_a}{W_b} = 2\Phi(\theta_0), \tag{7.7}$$

where the Shields stress θ_b takes the following form:

$$\theta_b = \frac{S_b D_b}{\Delta D_s}. \tag{7.8}$$

Summarizing, the analytical model for the long-term state of bifurcations under partial avulsion conditions can be cast into a system of four algebraic equations in terms of the four unknowns S_b, D_b, D_c and ΔQ. Specifically, by substituting (7.3) into (7.4), (7.6) into (7.5) and using (7.7, 7.8) we obtain:

$$\frac{D_c}{D_0} + \frac{\Delta\eta_{BRT}}{2} = 1 - (S_0 - S_b)\frac{L}{D_0}, \tag{7.9a}$$

$$\sqrt{\frac{S_b}{S_0}} \left(\frac{D_b}{D_0}\right)^{3/2} = 1 + \Delta Q, \tag{7.9b}$$

$$\left(\frac{D_c}{D_0}\right)^{3/2} = 1 - \Delta Q, \tag{7.9c}$$

$$\Phi(\theta_b) = 2\Phi(\theta_0). \tag{7.9d}$$

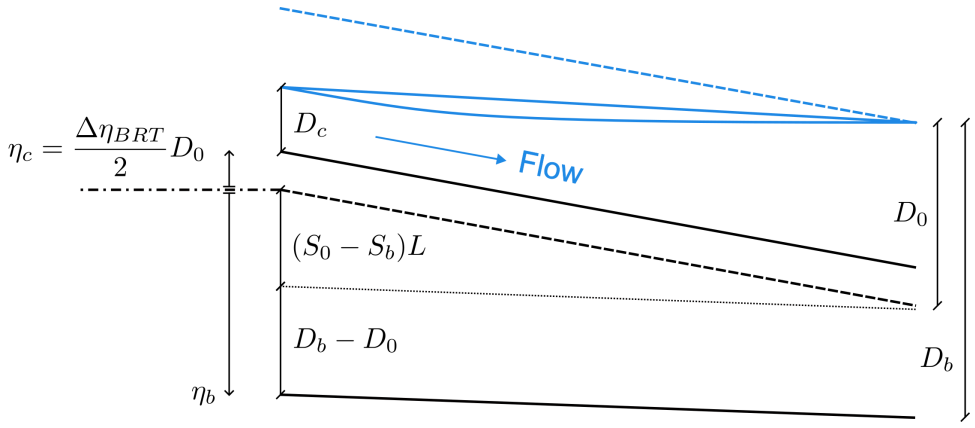


Figure 7.1: Schematic view of two anabranches that undergo a partial avulsion. The bed elevation and water surface profiles are shown for both the initial condition (dashed lines) and long-term configuration (solid lines). η stands for the bed elevation at the inlet of the bifurcates, while S is the longitudinal bed slope, L is the length of both branches and D is the water depth. The subscripts b and c refer to the dominant and non-dominant branch, respectively, while the subscript 0 denotes the initial reference conditions, which correspond to the initial conditions of the downstream branches. The dash-dotted line indicates the reference level for the bed elevation η, while the dotted line is plotted to highlight the two contributions to the bed elevation η_b appearing in Equation (7.6).

Despite its approximate nature, our simple analytical model proves capable of capturing the key ingredients that determine the equilibrium configurations reached by numerical simulations in which a partial avulsion occurs. As shown by Figure 7.2, the equilibrium discharge asymmetry ΔQ foreseen by the analytical model closely matches that obtained in numerical simulations, with an average relative accuracy of less than 3%. Specifically, our simplified model is able to correctly reproduce the dependence of ΔQ on both the aspect ratio β_0 and the dimensionless channel length L^*. On the contrary, the equilibrium values of ΔQ computed using the BRT model, besides being independent on the length of the bifurcates, are considerably lower than those shown by numerical simulations, although the dependence of ΔQ on the aspect ratio β_0 is similar.

The analytical model also makes it possible to determine the marginal conditions for which one of the bifurcates closes completely (full avulsion), and to compute the associated avulsion length L_{AV}. This is accomplished by setting $D_c = 0$ in Equation 7.9a, and isolating the length as:

$$L_{AV} = \frac{D_0}{S_0} \frac{1 - \frac{\Delta\eta_{BRT}}{2}}{1 - S_b/S_0}. \tag{7.10}$$

The resulting expression highlights the key ingredients that determine the avulsion length, as all terms on the right-hand side of Equation (7.10) bring a precise physical meaning. Specifically, the first factor is the backwater length:

$$L_B = \frac{D_0}{S_0}, \tag{7.11}$$

which provides the length scale of L_{AV}. Furthermore, the numerator of the second factor accounts for the aggradation experienced by the non-dominant branch until it stops transporting sediment, while the denominator holds the contribution of the incision of the dominant branch. The latter term can be determined from Equation 7.9b, by setting $\Delta Q = 1$ and using Equation (7.8), in the form:

$$\frac{S_b}{S_0} = \frac{1}{2}\left(\frac{S_b}{S_0}\frac{D_b}{D_0}\right)^{3/2} = \frac{1}{2}\left(\frac{\theta_b}{\theta_0}\right)^{3/2}. \tag{7.12}$$

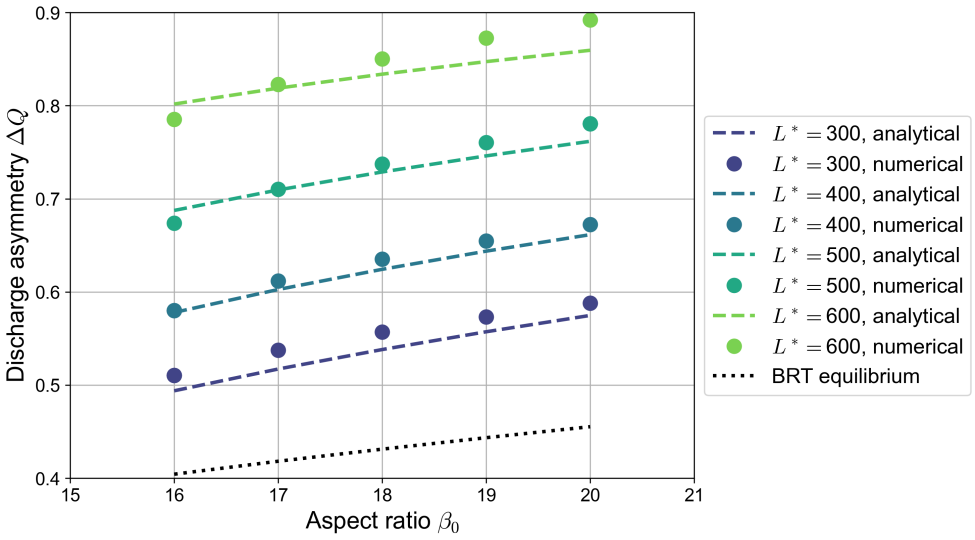


Figure 7.2: Comparison between the equilibrium values of the discharge asymmetry ΔQ of bifurcations undergoing partial avulsion as computed by numerical simulations (dots) and those predicted by the analytical model (dashed lines), for different values of the dimensionless length of the bifurcates $L^* = L/D_0$ ($\theta_0 = 0.07, C = 12$, transport formula of Meyer-Peter and Müller, 1948). Each dot represents the outcome of a single numerical simulation. The dotted line indicates the equilibrium solution computed by means of the BRT model, which is independent of the length of the branches.

This allows us to re-write Equation (7.10) as

$$\frac{L_{AV}}{L_B} = \frac{1 - \frac{\Delta\eta_{BRT}}{2}}{1 - \frac{1}{2}\left(\frac{\theta_b}{\theta_0}\right)^{3/2}}, \tag{7.13}$$

where θ_b can be calculated from mass conservation (7.7).

Results reported in Figure 7.3a reveal that, for typical parameter values of gravel bed rivers, the avulsion length is in the order of several hundred times the upstream flow depth. Furthermore, its dimensionless value exhibits a decreasing trend with both the Shields stress θ_0 and the aspect ratio β_0. The former inverse dependence is mainly driven by the role of the channel slope S_0, while the latter is due to the increase of the term $\Delta\eta_{BRT}$ with β_0. Interestingly, when we filter out the main effect of S_0 by scaling the avulsion length L_{AV} with the backwater length L_B, the dependence of the avulsion length on the Shields stress is reversed, as shown by Figure 7.3b.

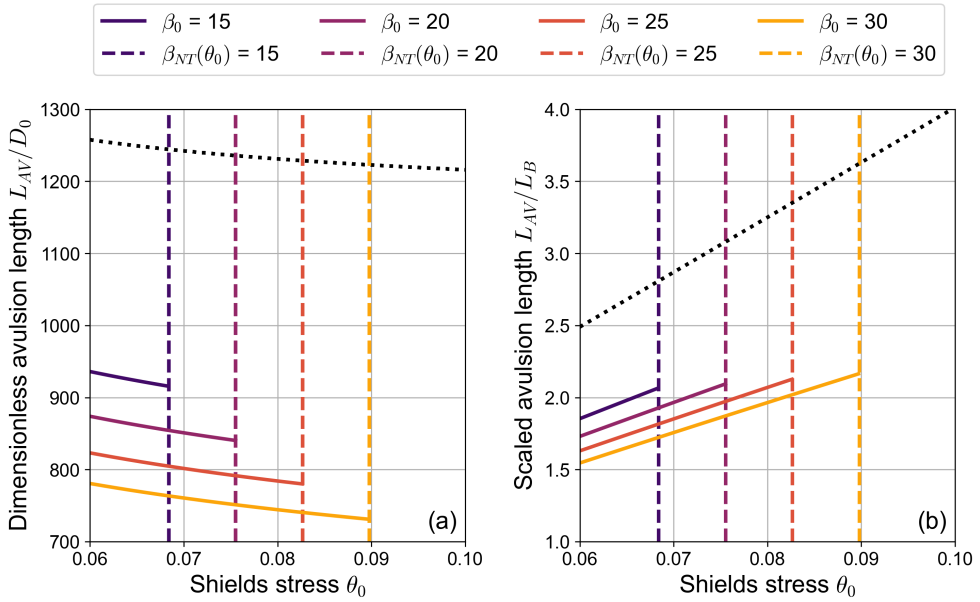


Figure 7.3: Dependence of (a) the dimensionless avulsion length L_{AV}/D_0 and (b) the scaled avulsion length L_{AV}/L_B on the Shields stress θ_0, for different values of the aspect ratio β_0, as obtained from Equation (7.13). Vertical dashed lines indicate the value of the Shields stress for which $\beta_0 = \beta_{NT}$, thus representing the boundary of the region of validity of the analytical model. The dotted line indicates the upper bound for L_{AV}, obtained by neglecting the β_0-dependent term $\Delta\eta_{BRT}$ ($C = 12$, transport formula by Meyer-Peter and Müller, 1948).

8 DISCUSSION AND CONCLUSIONS

The formulation of a new evolutionary model for a free bifurcation allowed us to study the equilibrium states in the so-called partial avulsion conditions, in which the flow velocity in one of the bifurcates is not sufficient to effectively transport sediments. In these conditions, the resulting equilibrium configuration turns out to be very different from that predicted by the Bolla Pittaluga et al. (2003) model. Specifically, the resulting long-term equilibrium solution is considerably more asymmetrical, and the inlet step is significantly higher. This happens because the bed slope of the shoaling branch is no longer able to adjust when sediment transport vanishes, while the dominant branch unavoidably undergoes a bed degradation process, which enhances both the inlet step and the discharge asymmetry. Bed degradation increases with the length of the branches, which therefore becomes a key control for the equilibrium configuration.

Consistently with Figure 4.1, partial avulsions occur when the aspect ratio of the main channel exceeds the threshold value β_{NT}. However, the actual value of the threshold displayed by simulations turns out to be slightly lower due to an overshoot phenomenon, i.e. in the transitory phase the discharge asymmetry reaches a value that exceeds the long-term equilibrium value. Moreover, the actual threshold for numerical simulations to undergo a partial avulsion may be further reduced with respect to the theoretical value β_{NT}, depending on the behaviour of the transport formula near critical conditions. For example, when considering the transport formula of Parker (1978), the bed evolution of the non-dominant branch "freezes" when the Shields stress is only slightly above the critical threshold $\theta_{cr} = 0.03$. This occurs because what actually determines the transition from a fully-active condition to partial avulsion is the ratio between the evolutionary timescales of the branches. Specifically, if the dominant branch degrades too quickly with respect to the other branch, it starts capturing more discharge than that foreseen by the BRT model, which rapidly leads to partial avulsion conditions. It is worth noting that, for the same reason, partial avulsions also occur when employing a transport formula that does not consider a critical threshold (e.g., Parker, 1990). In this case, the analytical threshold β_{NT} beyond which the BRT model doesn't work can no longer be defined. However, numerical simulations still show a threshold for β_0 above which partial avulsions occur. In these conditions, the shoaling branch practically freezes even though a minimal amount of sediment transport is still present, causing the bifurcation to reach a strongly unbalanced long-term configuration.

The analytical model developed in chapter 7 enables for computing the long-term state of bifurcations under conditions of partial avulsion, and for identifying the key parameters that control the transition between the different kinds of equilibrium configurations shown by numerical simulations and represented in Figure 6.5. When combined with the results of the BRT model, the analytical model allows us to draw a complete picture of the nature of the equilibrium solutions in the $\beta_0 - L/L_B$ parameters space, as illustrated in Figure 8.1. Specifically, for a given value of the reference Shields stress θ_0, four distinct regions are identified:

1. balanced solutions (i.e. $\Delta Q = 1/2$), occurring when the aspect ratio β_0 is lower than the length-independent critical threshold β_C;

2. unbalanced fully-active solutions, where at equilibrium both branches do actively transport sediment, occurring when β_0 lies between β_C and the no-transport threshold β_{NT};

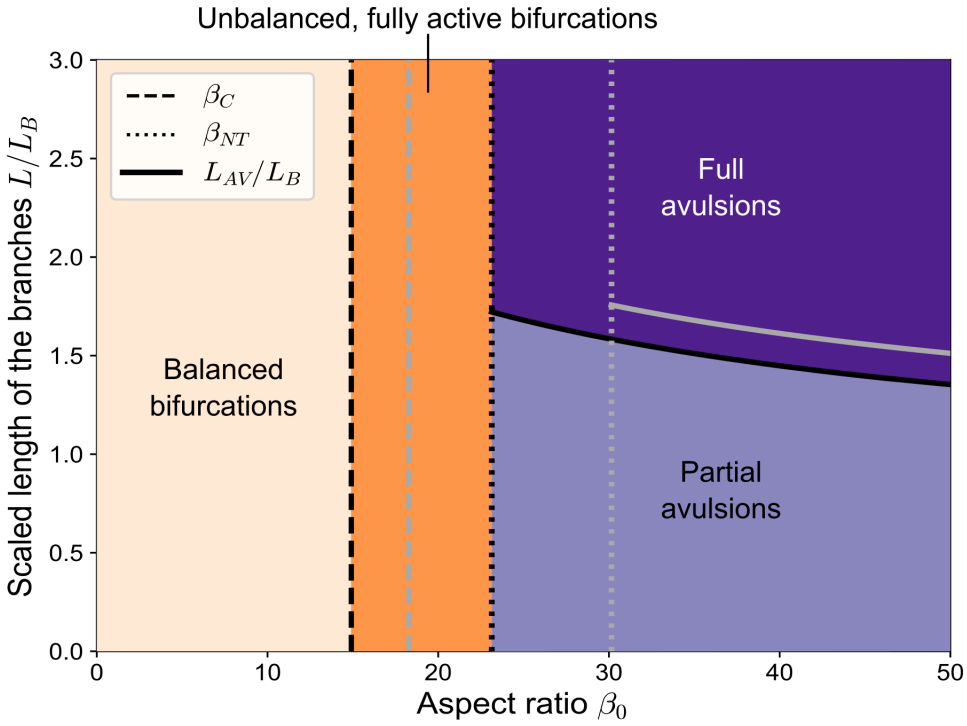


Figure 8.1: The different types of equilibrium configurations of a free bifurcation in the β_0 (aspect ratio) - L/L_B (scaled branch length) parameter space, resulting from the combination of the BRT model and our analytical model ($\theta_0 = 0.08$, transport formula of Meyer-Peter and Müller, 1948). The length of the bifurcates is scaled with the backwater length L_B, computed as $L_B = D_0/S_0$. The different line styles indicate the critical aspect ratio β_C, the aspect ratio of no-transport β_{NT} and the scaled avulsion length L_{AV}/L_B, as resulting from Equation (7.13). The grey lines show how these thresholds change when considering a slightly higher value of the Shields stress ($\theta_0 = 0.09$).

3. partial avulsion solutions, in which all sediments go in one branch, while a non-zero water discharge flows in the other, occurring when $\beta_0 > \beta_{NT}$ and the length of the branches is shorter than the threshold L_{AV};

4. full avulsions solutions, where one branch is abandoned and all the incoming water and sediment supplies are carried by the other branch, occurring when the aspect ratio is relatively large and the downstream branches are relatively long (i.e. $\beta_0 > \beta_{NT}$ and $L > L_{AV}$).

The threshold values β_C and β_{NT} increase as the Shields stress increases, and so does the scaled avulsion length L_{AV}/L_B, as discussed at the end of chapter 7.

A direct comparison between our model and experimental data is difficult, since available data from physical models are scarce and often focused on the effect of external forcing factors. For example, the laboratory experiments by Salter et al. (2019) were tailored to depositional environments and reproduced bifurcations with prograding branches, while Szewczyk et al. (2020) analysed the influence on the water discharge partition of changing the bifurcation angle, for values of the aspect ratio β_0 much smaller than the no-transport threshold β_{NT}. To the authors' knowledge, the laboratory experiments by Bertoldi and Tubino (2007) are the only ones that analysed how initially balanced "free" bifurcations develop unbalanced equilibrium configurations, possibly leading to partial or full avulsion. Considering this dataset, it is worth noting that the three experimental runs that resulted in a full avulsion featured an aspect ratio close to or larger than the no-transport aspect ratio β_{NT} and a length of the branches larger than the avulsion threshold L_{AV}, consistently with our model predictions.

As shown in Figure 8.1, when the downstream branches are sufficiently long, the degradation process can eventually lead to the complete abandonment of the shoaling branch, so that water and sediment fluxes are entirely conveyed in a single thread (full avulsion). The branch length at which full avulsion occurs (L_{AV}) is found to scale with the backwater length. This result is consistent with existing studies of river deltas that show how the distance of apex avulsions from the coastline scales with the backwater length (Chatanantavet et al., 2012; Jerolmack & Mohrig, 2007). It is worth remarking that previous studies found this scaling by analysing deposition induced by time-dependent flow discharge, while our study highlights the link between the backwater length and the full avulsion threshold by analysing the interplay between the downstream boundary condition and the incision required for the abandonment of the shoaling channel.

Our analysis provides a clear example of how the complete abandonment of one of the two branches can be caused by the incision of the dominant channel driven by an autogenic mechanism. In general, bed incision takes place whenever the bifurcation becomes unbalanced, as the resulting difference of the Shields stress between the two branches makes them overall more efficient in transporting sediments (Ferguson, 2003; Paola, 1996). Therefore, a smaller slope is sufficient to ensure equilibrium with the imposed sediment supply. This effect is further amplified when the water discharge asymmetry sharply increases due to a partial avulsion. This can provide a mechanistic interpretation of the so-called process of incisional avulsion (Mohrig et al., 2000; Slingerland & Smith, 2004), in which channel abandonment is preceded by headward erosion of the avulsed channel.

The tendency to abandon smaller branches can be seen as a general characteristic of rivers systems undergoing significant incision, as that produced by a lack of sediment supply. Specifically, discharge asymmetry of river bifurcations generally increases when the overall degradation rate is relatively rapid. In this case, the shoaling branch is not able to keep up with the erosion, thus becoming increasingly superelevated with respect to the dominant channel. This may provide a way to interpret the morphological evolution of braided rivers under conditions of reduced sediment availability, which typically lead to the simplification of the channel network and eventually to the transition to single-thread configurations (e.g., Germanoski & Schumm, 1993; Marti & Bezzola, 2006; Redolfi & Tubino, 2014).

The numerical and analytical results reported in Figure 6.3 and Figure 7.2 highlight the inadequacy of the BRT model to reproduce the strongly unbalanced long-term configuration of free bifurcations when a branch avulsion occurs, as already pointed out by Kleinhans et al. (2008). They also provide a new insight into the long-debated question on the role of the nodal condition for sediment partitioning. In fully active conditions, the inlet step between the downstream branches of an unbalanced bifurcation generates a lateral bed slope at the node, such that the transverse sediment flux Q_{sy} compensates the imbalance of transport capacities between the bifurcates themselves. The efficiency of this lateral deflection thus plays a key role in determining the equilibrium configuration of the bifurcation, as shown by the BRT model. On the contrary, under partial (or full) avulsion conditions the incoming sediment supply is entirely steered towards the dominant branch, regardless of the inlet step. After the shoaling branch gets morphodynamically inactive, the development of the inlet step between the bifurcates is entirely governed by the evolution of the dominant branch, and specifically by the changes of its bed slope and water depth that are necessary to attain a morphodynamic equilibrium.

Under this condition, the transverse flux of sediments Q_{sy} is mainly driven by flow exchange (the first term on the left-hand side of the nodal relationship 5.7), while the lateral deflection due to transverse slope (the second term on the left-hand side of Equation 5.7) plays a minor role in determining the equilibrium bifurcation asymmetry. As a result, the bed elevation gap between the node cells of the BRT model (see Figure 5.1) simply yields the residual contribution ensuring the condition $Q_{sy} = Q_{s0}/2$ at equilibrium, and it does no longer align with the downstream inlet

step. As can be seen in Figure 6.2, the resulting evolution of the dominant branch shows no discontinuity between the fully-active initial stages and the partial-avulsion long-term state. In fact, the transverse flux returned by Equation (5.7) produces a smooth transient behaviour in the dominant channel, and ensures mass conservation.

In general, the timescale of the adaptation of the bifurcation to its long-term state is much longer than that governing the first evolutionary stages, as shown for example by the lower-right panel of Figure 6.2. This happens because the dominant branch needs time to adapt its bed slope to the equilibrium value. In the meanwhile, other upstream or downstream effects may influence the evolutionary process of the bifurcation, namely the effect of changes in sediment supply, the adaptation of channel width, variations of the downstream water level (e.g. sea level rise). While our model can be straightforwardly extended to reproduce such effects, further investigation is needed to assess their relevance in determining the bifurcation configuration, depending on the characteristic timescales of the associated processes.

The present formulation is valid under conditions where sediment is dominantly transported as bedload. Although some promising approaches have been proposed (Iwantoro et al., 2021), a systematic understanding of the morphodynamics of channel bifurcations in suspension-dominated channels is still lacking, thus preventing a reliable extension of our model. However, we can expect that a similar scenario of transition to the avulsion condition also occurs for sand bed channels where most sediments are transported in suspension. In this case the higher values of the Shields stress are likely to be associated with a higher threshold β_{NT}, so that larger values of the aspect ratio may be needed to reach avulsion conditions.

Finally, it is worth noting that in this work we consider the water discharge to be constant in time. Therefore, the application of the model to unsteady flow conditions is only possible when flow variations are sufficiently slow to be represented as a sequence of quasi-steady states. To account for flow variability it would be possible to define an equivalent, formative value of Q, for example by considering the method of the effective discharge proposed by Wolman and Miller (1960), or to adopt a procedure similar to that recently proposed by Carlin et al. (2021) for alternate bars.

CONCLUSIONS

In this study we developed a novel 1-D numerical model for predicting the evolution of a river bifurcation. Based on numerical findings, we then built a new analytical model, specifically designed to reproduce the equilibrium configuration of a bifurcation under partial avulsion conditions. Coupling the latter model with that proposed by Bolla Pittaluga et al. (2003) provides a suite of analytical tools that covers the full range of possible long-term states of a free bifurcation in the controlling parameters space, namely the aspect ratio and the Shields stress.

The combined analysis of the numerical and analytical model yields the following conclusions:

- When the aspect ratio of the main channel exceeds the threshold value β_{NT}, the bifurcation undergoes partial avulsion conditions, in which the shoaling channel is no longer able to effectively transport sediments.

- Under partial avulsion conditions, the dominant channel is subject to degradation, while the morphological evolution of the other branch is inhibited. This produces a significant increase of the inlet step at the entrance of the bifurcates, further enhancing the water discharge entering the dominant channel. This autogenic positive feedback mechanism results in a highly unbalanced equilibrium configuration, whose long-term degree of asymmetry is influenced by the length of the downstream branches.

- When the dimensionless length of the bifurcates exceeds a threshold value L_{AV}, the discharge asymmetry tends to unity, which implies the complete abandonment of the shoaling channel (full avulsion). Such threshold length is found to scale with the backwater length.

Overall, this work allows us to draw for the first time a complete picture of conditions that may lead to the abandonment of one branch in "free" river bifurcations. This provides the basis for more detailed studies about the role of other factors – such as flow variability, sea level rise and bank erosion – in determining the long-term evolution of bifurcations. Furthermore, our study gives valuable insights for the design of sustainable river restoration interventions aimed at promoting the formation of rich, multi-thread channel patterns.

9 APPENDIX: COMPARISON WITH LABORATORY EXPERIMENTS

The available experimental datasets are not sufficient to allow a detailed verification of the new equilibrium model presented in this work. Data from physical models are scarce, and experiments were mainly focused on the analysis of the effect of specific "forcing" factors. For example, the laboratory experiments by Salter et al. (2019) were tailored to depositional environments and reproduced bifurcations with prograding branches, while Szewczyk et al. (2020) analysed the influence on water discharge partition of changing the bifurcation angle, for values of the aspect ratio β_0 much smaller than the no-transport threshold β_{NT}.

To the authors' knowledge, the laboratory experiments by Bertoldi and Tubino (2007) are the only ones that analyse how initially balanced "free" bifurcations develop unbalanced configurations, possibly leading to partial or full avulsion. Indeed, a specific analysis of their results seem to support our findings, as shown in Figure 9.1 where we report, for each experimental run, the computed values of β_0/β_{NT} and L/L_{AV}. Consistently with our predictions, they reveal that full avulsions (i.e. the complete closure of one of the branches) were observed in the three experimental runs in which β_0 was greater than (or closer to) β_{NT} and the channel length L was longer than the avulsion length L_{AV}.

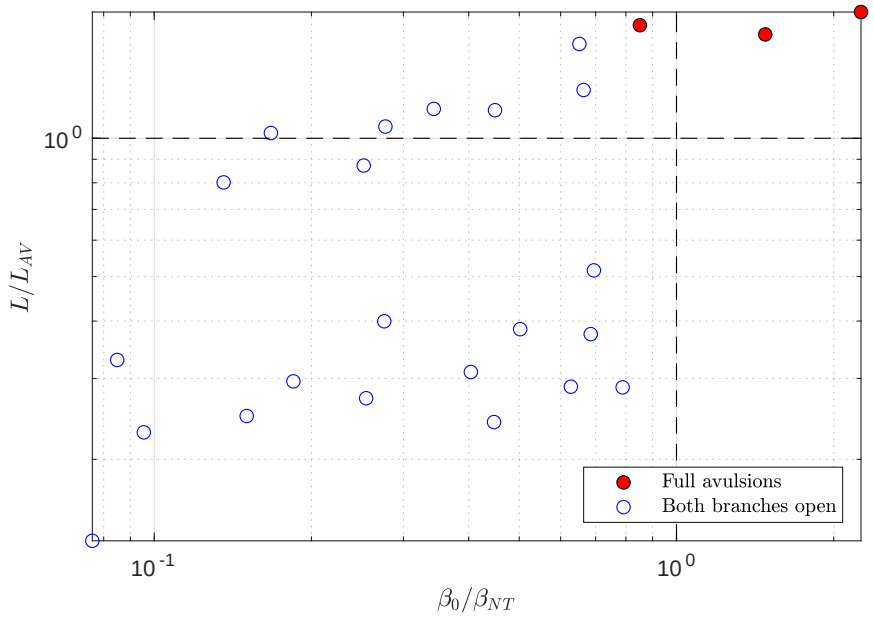


Figure 9.1: Results from the analysis of experimental data by Bertoldi and Tubino (2007). Consistently with our theory, experiments where full avulsions were observed (filled markers) fall in the region $\beta_0 > \beta_{NT}$ and $L > L_{AV}$.

Part III

HOW FAST DO BIFURCATIONS EVOLVE?

ABSTRACT

River bifurcations are the fundamental building blocks of a variety of fluvial environments such as braiding and anastomosed rivers, alluvial fans, and river deltas. Their long-term equilibrium configurations have been widely explored, together with the influence of several external forcing factors, whereas less attention has been devoted to investigate the characteristic timescale with which bifurcations evolve over time. In this work, we address this issue by combining the results of a 1-D numerical model with those obtained through a linear stability analysis that accounts for the length of bifurcates. Numerical results show that the timescale of the adaptation of water and sediment partition at the bifurcation node is much shorter than the time required to achieve the long-term equilibrium of the bifurcates. We find that the nodal point evolution becomes faster as the value of the width-to-depth ratio increases above the critical threshold for the bifurcation stability, while it gets slower as the length of the bifurcates increases. The timescale becomes independent of the branch length when this length exceeds a threshold value above which the effect of the downstream boundary condition no longer affects the evolution of the bifurcation node. The analysis of a large dataset of gravel-bed bifurcations reveals that the evolutionary timescale of most of them is larger than that of natural flow variations. Moreover, the rate at which the water and sediment partitioning at bifurcations changes over time is generally smaller than the fluctuation rate of sediment transport caused by the migration of bars in the upstream channel, especially for bifurcations with long branches.

The content of this part has been submitted to the journal Earth Surface Processes and Landforms, and is currently under review. Reference: Barile, G., Redolfi, M., and Tubino, M.: Time scales of River Bifurcations.

10 INTRODUCTION

The evolution of dynamical systems is determined by the combination of various processes acting on different timescales. River systems are no exception, as their evolutionary trajectories are controlled by the relative rates of different morphodynamic processes and by the rate of change of external forcings. Recognizing a hierarchy of time (and spatial) scales is crucial to explain the occurrence of the variety of sedimentary patterns observed in fluvial environments, while it also provides a powerful tool to identify suitable modelling approaches for specific morphodynamical problems (Seminara, 2010). A notable example is the key assumption of instantaneous adaptation of the flow field and bed topography to planform changes, on which theoretical models of the evolutionary trajectories of river meanders are commonly based (Bogoni et al., 2017; Eke et al., 2014; Monegaglia et al., 2019; Seminara et al., 2001).

Jerolmack and Mohrig (2007) provided a straightforward example of application of scaling analysis to channel branching in depositional rivers, arguing that the relative velocity of bank migration, as compared to that of channel sedimentation, determines whether a river preferably evolves towards a single-thread or a multi-thread configuration. The ratio between the timescales of bank erosion and riverbed evolution was also found to govern the response of the bankfull geometry of developing meandering reaches (Monegaglia & Tubino, 2019; Parker et al., 2011).

Other studies investigated the role exerted by the variability of external forcings on individual fluvial processes, such as the relationships between the time variability of sediment supply and the avulsion timescale in braided rivers (Ashworth et al., 2004) and the impact of sea-level rise (Chadwick et al., 2020; Liang et al., 2016) and of the hydrological regime (Brooke et al., 2022) on avulsions in alluvial fans and river deltas. In all the mentioned studies the timescale of the external forcing was scaled with the sediment transport rate, which sets a system-specific reference timescale.

In general terms, this kind of analysis is based on a methodological distinction between the external factors acting at the boundaries and the internal morphodynamic responses, the identification of which depends on the specific process under investigation, and on the recognition of their respective timescales. Hence, the definition of the intrinsic timescales of morphodynamic processes is a fundamental prerequisite to determine the capability of external factors to affect the evolutionary trajectories of fluvial systems. This is the case of migrating alternate bars in gravel-bed rivers, as the intrinsic timescale of bar development (i.e. the reciprocal of the bar growth rate) is often comparable with the duration of formative flood events (Tubino, 1991). Building upon this result, Carlin et al. (2021) showed that the dependence on the flow discharge of the intrinsic rate of change of bar amplitude, as obtained from the weakly nonlinear theory of Colombini et al. (1987), plays a crucial role in determining the response of river bars to the hydrological regime, and ultimately controls their long term average characteristics.

Contrary to the aforementioned fluvial environments, the analysis of the characteristic timescale of river bifurcations has received less attention, although their long-term behaviour and equilibrium configurations have been extensively investigated in the last decades. A key feature emerging from field observations is that natural bifurcations are likely to display unbalanced equilibrium configurations, in which one of the two branches carries the larger fraction of the incoming water and sediment discharge (Edmonds & Slingerland, 2008; Kleinhans et al., 2013; Zolezzi et al., 2006).

The mechanism through which bifurcations develop these configurations has been widely analysed theoretically by means of the quasi-2D nodal point relation for

sediment partitioning originally proposed by Bolla Pittaluga et al. (2003), hereafter referred to as BRT. The main outcome of these analyses is that bifurcations can spontaneously evolve toward unbalanced configurations due to an intrinsic instability mechanism, within a wide range of values of the control parameters (hydraulic geometry and sediment size), even in the absence of external forcings and with a symmetric planform configuration. A clear evidence of this mechanism was also provided by the flume experiments of Bertoldi and Tubino (2007). In real-world bifurcations such inherent morphodynamic response is likely to be affected by a variety of external forcings, such as alternate bars (Bertoldi et al., 2009; Le, Crosato, Mosselman, & Uijttewaal, 2018), variable water and sediment supply (Mendoza et al., 2022; Miori et al., 2006b), tides (Ragno et al., 2020; Wagner & Mohrig, 2019), prograding branches (Salter et al., 2018) and vegetation growth (Burge, 2006). The influence of these factors on river bifurcations has been studied so far by either focusing on specific case studies or analysing the long-term equilibrium configurations. A key aspect revealed by these studies is that the mark of the intrinsic instability mechanism can also be seen in the equilibrium states of bifurcations subject to nonuniform boundary conditions, such as those determined by a curved upstream reach or by a downstream imposed slope advantage (Redolfi et al., 2019). Thus, while it is known how external factors can compete or cooperate with the intrinsic response of bifurcations to determine their equilibrium states, the time required to achieve these states and the role of these factors in the transient stage still await for a quantification.

Previous field observations and numerical analyses have provided some information on the evolutionary timescale of bifurcations. On one hand, a field study of Bertoldi (2012) on a gravel-bed braided reach of the Tagliamento River (Italy) suggested that bifurcations may evolve on a timescale similar to that of bar migration and flood duration. On the other hand, based on field observations in an anabranching river, Burge (2006) argued that the evolutionary timescale of bifurcations depends on the formation mechanism, ranging from swift changes in their morphology for bifurcations formed after neck cutoffs, to slow to no evolution for bifurcations generated by central bars deposition. These observations are suggestive of a dependence of the transient behaviour of bifurcations on the length of the bifurcates, which is known to control the equilibrium states of bifurcation-confluence units (Ragno et al., 2021). As for numerical studies, Delft3D simulations performed by Kleinhans et al. (2008) showed that the evolutionary timescale of bifurcations is of the order of decades, thus much slower than that of "local" morphological changes at the bifurcation node. This result has been recently confirmed by the numerical simulations performed by Gao et al. (2024), who analysed the evolution of an idealized bifurcation subjected to dredging. In their study, the authors pointed out that the rate at which the bifurcation evolved towards its equilibrium configuration was very slow, namely of the order of 10^2 times the timescale set by the reference transport capacity (i.e. the Exner timescale).

The above results, although not providing an exhaustive description of the timescale of bifurcations and of its dependence on flow conditions and planform geometry, raise further relevant questions on the matter. How fast is the adaptation of flow and sediment partition at the node, as compared with the time needed to achieve the overall equilibrium of the system? How does the length of the bifurcates affect the speed of this adaption process?

The role of the length of the downstream branches on the evolutionary timescale of bifurcations was first analysed by Miori et al. (2006a). To do so, they used a simplified unsteady model in which the ratio between the channel slopes of the bifurcates was assumed to be constant over time. Therefore, their model was unable to reproduce the effect of local slope changes at the inlets of the distributaries caused by the variation of the water and sediment fluxes delivered by the bifurcation node (i.e. the "boundary layer" effect described for single channels by Wong and Parker, 2006). Local changes in bed slope caused by the uneven partition of water

and sediment were also observed in previous numerical simulations of evolving bifurcations (Barile, Redolfi, & Tubino, 2024; Kleinhans et al., 2008). Given the sensitivity of equilibrium configurations to an imposed slope advantage (Redolfi et al., 2019), one might expect such local changes to also play a relevant role in the transient behaviour of bifurcations.

In this work, we try to address the questions formulated above by analysing the time evolution of a simple, unforced symmetrical bifurcation. More specifically, we aim at quantifying how the intrinsic timescale of bifurcations depends on the key controlling parameters and on modelling choices. This is accomplished by formulating an unsteady morphodynamic model, based on the quasi-2D nodal point relation of Bolla Pittaluga et al. (2003), in which the full coupling between the node and the downstream channels evolution is retained. This model is then used to analyse the evolution of an initially balanced bifurcation that evolves towards an unbalanced configuration. The governing system of equations is first solved using the fully nonlinear numerical scheme formulated in Barile, Redolfi, and Tubino (2024). Then, the system is analysed through a novel, theoretical approach based on a linear, spatially and temporally resolved solution of the model equations.

We analyse model outputs by first providing an operative definition of the intrinsic timescale of bifurcations. Then, we explore its dependence on the governing parameters, namely the flow conditions in the upstream channel and the length of the bifurcates. Lastly, we compare this timescale with those of some external forcings that most influence the evolution of gravel-bed bifurcations, namely the migration of bars in the upstream channel and the time variability of the flow discharge.

11 MODEL FORMULATION

We consider a bifurcation composed of three branches having a rectangular cross-section and fixed banks, with the downstream bifurcates having the same length. The system is fed with constant water and sediment supplies, and a fixed water level is imposed at the downstream boundary of the domain. When the sum of the widths of bifurcates equals the upstream channel width, this system admits of a simple steady state solution in which the flow and the sediment transport are uniform in all branches and the bed slope, the depth and the unit water and sediment discharge are identical in the three channels, regardless of the respective widths of bifurcates. We take this equilibrium solution as the initial state of the system, and we then analyse how it evolves in time by applying a small perturbation to the transverse bed slope between the node cells. Without loss of generality, in the following we will assume the widths of the downstream channels to be equal, which implies that water and sediment discharge are split equally between the downstream branches in the initial state. We term the examined configuration "unforced" because the downstream water level is set at the value corresponding to the initial uniform conditions.

To make our problem dimensionless, we scale the variables with the geometric and hydraulic parameters of the reference flow (i.e. the initial uniform flow in the upstream channel), here denoted with the subscript o. The resulting dimensionless variables read (starred variables refer to dimensional quantities):

$$x := \frac{x^*}{W_0^*/2},\ t := \frac{t^*}{T_E^*},\ (\eta, D) := \frac{(\eta^*, D^*)}{D_0^*},\ U := \frac{U^*}{U_0^*},\ q := \frac{q^*}{q_0^*},\ q_s := \frac{q_s^*}{q_{s0}^*},\ L := \frac{L^*}{D_0^*}, \tag{11.1}$$

where x^* is the longitudinal coordinate, t^* is time, W^* is the channel width, η^* is the bed elevation, D^* is the flow depth, U^* is the flow velocity, q^* is the flow discharge per unit width, q_s^* is the transport capacity per unit width, and L^* is the length of the bifurcates. The dimensionless time t is defined by scaling t^* with the dimensional timescale T_E^* of the bed evolution defined by the Exner equation

$$T_E^* := (1-p)\frac{W_0^* D_0^*}{2\, q_{s0}^*}, \tag{11.2}$$

where p is the bed porosity.

We compute the unit transport capacity in terms of the local value of the Shields stress θ as:

$$q_s^* = \sqrt{\Delta g D_s^3}\,\Phi(\theta),\ \theta = \frac{U^{*2}}{c^2 \Delta g D_s}, \tag{11.3}$$

where Δ and D_s are the relative submerged density and the grain diameter of sediment particles, respectively, g is gravity, and c is the Chézy coefficient. In the following the latter parameter is assumed to be constant, though the analysis can be readily extended to include its dependence on the local relative roughness. To compute the bedload function Φ we use the formula proposed by Parker (1978).

The mathematical model is based on the solution of the one-dimensional shallow water flow equations and Exner sediment continuity equation, and adopts a quasi-

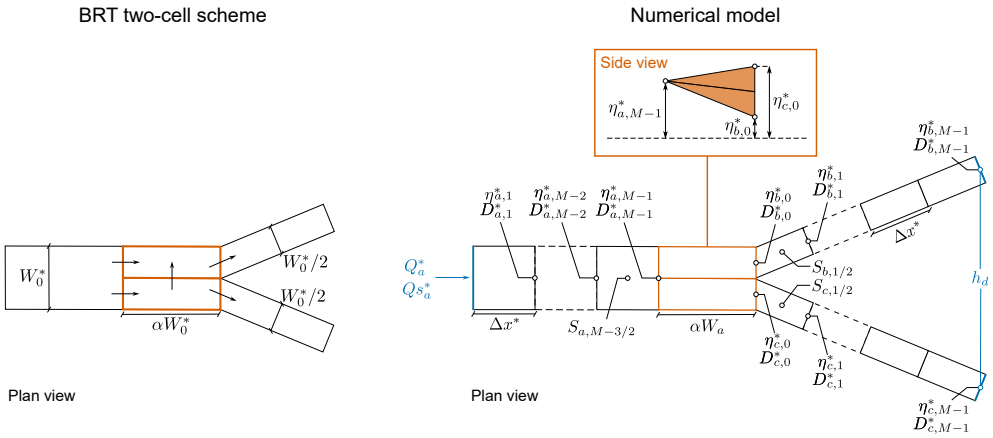


Figure 11.1: Sketch of (a) the two-cell scheme adopted to compute the transverse fluxes of water and sediments and (b) the spatial discretization and boundary conditions of the numerical model. The side view describes the triangular step approach used to model the bed elevation along the node cells.

steady approximation for the hydrodynamics. The governing equations can be expressed in dimensionless form as:

$$U\frac{\partial U}{\partial x} + \frac{1}{Fr_0^2}\left(\frac{\partial D}{\partial x} - \beta_0 S\right) + \frac{\beta_0 U^2}{c^2 D} = 0, \tag{11.4a}$$

$$\frac{\partial (UD)}{\partial x} = 0, \tag{11.4b}$$

$$\frac{\partial \eta}{\partial t} + \frac{\partial q_s}{\partial x} = 0, \tag{11.4c}$$

where $S = -\partial \eta^*/\partial x^*$ is the local bed slope, Fr_0 is the reference Froude number, and β_0 is the reference half-width to depth ratio (hereafter, aspect ratio).

The formulation of the internal conditions at the bifurcation node closely follows the two-cell approach originally introduced by Bolla Pittaluga et al. (2003), which accounts for the transverse flux of water (q_y) and sediments (q_{sy}) just upstream the node (see Figure 11.1). Assuming the downstream branches (b and c) to have half the width of the upstream channel (a), the water and the sediment balance within each node cell, once expressed in dimensionless form, read:

$$q_b = q_a + 2\alpha q_y, \quad q_c = q_a - 2\alpha q_y, \tag{11.5}$$

$$2\alpha \frac{d\eta_b^N}{dt} = q_{sa}^O - q_{sb}^I + 2\alpha q_{sy}, \quad 2\alpha \frac{d\eta_c^N}{dt} = q_{sa}^O - q_{sc}^I - 2\alpha q_{sy}, \tag{11.6}$$

where the cell length has been computed as αW_0^*, where α is an order-1 parameter, and the superscripts O and I denote the upstream and the downstream end of each cell, respectively, while η^N is the mean bed elevation within each cell (see Figure 11.1), say for cell b,

$$\eta_b^N = \frac{\eta_a^O + \eta_b^I}{2}. \tag{11.7}$$

According to the BRT model, the sediment exchange between the two cells results from the combined effect of water exchange and gravity due to the transverse bed slope. Thus, the transverse flux of sediment can be given the following dimensionless form:

$$q_{sy} = q_{sa}^O \left[\frac{q_y}{q_a} - \frac{r}{\beta_0 \sqrt{\theta_a}}\left(\eta_b^N - \eta_c^N\right)\right], \tag{11.8}$$

where θ_a is the Shields parameter of the upstream incoming flow and r is an empirical coefficient that measures the gravity effect (Baar et al., 2018).

The model requires the definition of the cell length, i.e. of the parameter α, for which different estimates have been adopted in the literature based on empirical calibrations (see Table 1 of Redolfi, 2023). Physically, the cell length should correspond to the longitudinal spatial scale of two-dimensional effects on flow and bed topography induced by the unequal hydro-morphodynamical response of bifurcates. A first theoretical estimate of α was given by the two-dimensional linear analysis of Redolfi et al. (2016), where it was shown that the critical value of β_0 above which the symmetrical balanced solution becomes unstable, leading to unbalanced equilibrium solutions, coincides with the resonant value β_R that discriminates between prevailing downstream or upstream morphodynamic influence (Zolezzi & Seminara, 2001). Based on this result, and adopting a suitable scaling of the bifurcation cell length that incorporates the dependence of β_R on the Chézy coefficient, Redolfi (2023) provided the following estimate of α:

$$\alpha = \frac{\pi^2}{16}\frac{c^2}{\beta_0}. \tag{11.9}$$

We note that the triangular step approach adopted herein implies that the bed elevation difference between the node cells in Equation (11.8) is computed as $(\eta_b^N - \eta_c^N)$, which is half the value $(\eta_b^I - \eta_c^I)$ used in most applications of the BRT model. Therefore, our results are consistent with those of previous works provided we multiply the coefficient α by a factor two.

By substituting (11.8) into (11.6), and recalling that the scaling reported in Equation (11.1) implies that $q_a = 1$, we obtain:

$$2\alpha\frac{d\eta_b^N}{dt} = q_{sa}^O\left[q_b - \frac{2\alpha r}{\beta_0\sqrt{\theta_a}}\left(\eta_b^N - \eta_c^N\right)\right] - q_{sb}^I, \tag{11.10}$$

$$2\alpha\frac{d\eta_c^N}{dt} = q_{sa}^O\left[q_c + \frac{2\alpha r}{\beta_0\sqrt{\theta_a}}\left(\eta_b^N - \eta_c^N\right)\right] - q_{sc}^I. \tag{11.11}$$

To complete the set of nodal conditions, we impose the water level at the node to be the same in all branches.

Finally, we note that the values of five dimensionless parameters are required to define the initial configuration in dimensionless form, namely the aspect ratio β_0, the Shields stress θ_0, the length of the bifurcates L, the dimensionless grain size $d_{s0} = D_s/D_0^*$ and the Chézy coefficient c, since the Froude number Fr_0 can be retrieved from the relationship

$$Fr_0^2 = c^2\Delta d_{s0}\theta_0, \tag{11.12}$$

which holds for uniform flow conditions. The results presented in the following sections have been obtained for different combinations of β_0 and L, and fixed values of $\theta_0 = 0.08$, $d_{s0} = 0.01$ and $c = 12$.

11.1 NUMERICAL IMPLEMENTATION

We adopt the same numerical model described in Barile, Redolfi, and Tubino (2024), to which we refer to for further details. To integrate Equations (11.4) in space and time, we use the finite-difference scheme depicted in Figure 11.1, in which each of the three branches is discretized by means of M nodes, each identified by means of the index $i = 0 \ldots M-1$. The morphodynamic evolution of the system is modelled by first computing the flow discharge and water depth along the channels and then updating their bed elevation profiles, according to a decoupled approach. Starting from an initially balanced configuration, we apply a small asymmetric perturbation to the bed elevation of the downstream branches, and we let the bifurcation evolve autonomously over time until a long-term equilibrium condition is achieved. In the following, we briefly describe how the time evolution of the bifurcation is implemented in the numerical model.

The hydrodynamic conditions of the branches are evaluated by means of the gradually-varied flow equation, which can be readily derived by combining Equations (11.4a)-(11.4b) as

$$\frac{dD}{dx} = \frac{\beta_0}{1 - Fr^2}\left(S - \frac{Fr^2}{c^2}\right), \quad Fr^2 = Fr_0^2 \frac{q^2}{D^3}. \tag{11.13}$$

At any given time step, the flow discharge in the downstream branches is unknown. Thus, the flow partitioning at the bifurcation node is computed beforehand through an iterative procedure, which relies on the fact that the bed elevation (and therefore the bed slope S) is known at any point of the three branches from the previous time step. Starting from a first guess of the unit discharges q flowing in the bifurcates, Equation (11.13) is integrated in the upstream direction in both channels by means of a fourth-order Runge-Kutta scheme. The integration starts from the water depth at the downstream end of each branch, which is computed as the difference between the fixed water level and the bed elevation known from the previous time step. The procedure is then repeated by iterating over q using the Newton-Raphson method, until the water level at the inlet of the branches is the same.

Given the flow discharge flowing in each branch, we retrieve the water-surface profile for each branch for the current iteration. We then compute the Shields stress and the associated transport capacity at each node. Finally, the bed elevation is updated to the following time step by integrating Equation (11.4c) according to an upwind approach, where the computation of the spatial derivative of the bed elevation takes into account that bed perturbations travel downstream in subcritical conditions.

12 LINEAR ANALYSIS

A closed-form solution of the governing system of equations derived in chapter 11 can be obtained by means of a linear model. The linear analysis takes as reference state the initial equilibrium solution, in which water and sediment are equally distributed in the bifurcates, and flow and sediment transport are uniform in all branches. Previous studies considered a simplified approach, where the evolution of the downstream branches was modelled as a sequence of uniform-flow states (Bolla Pittaluga et al., 2015; Salter et al., 2018). This is justified when analysing the stability of equilibrium solutions, because in their neighbourhood the evolution is so slow that the downstream channels have enough time to adapt their slope over the entire length, to the point that stability can be analysed also considering a fully-steady approach (Redolfi et al., 2016). However, as will be discussed later, this assumption is not appropriate to determine the timescale of the bifurcation evolution. To overcome this limitation, we need to derive a linear solution that takes into account the spatial and temporal evolution of the downstream branches.

To this aim, we first derive the linear solution for a single branch subject to small-amplitude perturbations set at the channel boundaries. We then analyse the stability of the bifurcation by coupling this solution with the nodal point conditions.

12.1 LINEAR SOLUTION FOR DOWNSTREAM CHANNELS

The objective of this section is to determine the solution for a single channel, the boundary conditions of which are slightly perturbed with respect to the reference state. We assume that the small-amplitude perturbation of the boundary conditions has a well-defined time structure. Specifically, we consider a perturbation in the harmonic form $e^{\omega t}$, where

$$\omega = \Omega + i\chi \tag{12.1}$$

is a complex frequency, the real part of which (Ω) is the growth rate of the perturbation, while the imaginary part (χ) is the angular frequency, representing an oscillation in time. This assumption does not limit the generality of the solution, because any variation of the boundary conditions in time can be expanded as a sum of harmonic components, whose respective solutions can be determined separately and then recombined thanks to the linear character of the analysis. We note that the timescale of the imposed perturbation must be sufficiently slow to fulfil the quasi-steady hypothesis adopted herein.

Following the standard approach of linear analysis, each variable is expanded in the form:

$$X = X_0 + \delta X_1, \tag{12.2}$$

where X_0 is the reference state and δ measures the amplitude of perturbation. Substituting into the governing system (11.4), expanding in Taylor series around $\delta = 0$ and neglecting higher order terms, we obtain the following linear system:

$$\begin{aligned}
&\frac{\partial U_1}{\partial x} + \frac{1}{Fr_0^2}\frac{\partial}{\partial x}(\eta_1 + D_1) + \frac{\beta}{c^2}\left[2U_1 - D_1\right] = 0,\\
&\frac{\partial U_1}{\partial x} + \frac{\partial D_1}{\partial x} = 0, \qquad\qquad ,\\
&\frac{\partial \eta_1}{\partial t} + 2\Phi_T\frac{\partial U_1}{\partial x} = 0,
\end{aligned} \tag{12.3}$$

where the coefficient

$$\Phi_T = \frac{\theta_0}{\Phi_0}\frac{\partial \Phi}{\partial \theta} \tag{12.4}$$

measures the sensitivity of the sediment transport rate to variations of the Shields stress.

The linear system (12.3) admits solutions of the form:

$$(\eta_1, U_1, D_1) = (\tilde{\eta}, \tilde{U}, \tilde{D}) e^{\lambda x + \omega t} + \text{c.c.}, \tag{12.5}$$

where c.c. denotes the complex conjugate, λ is a complex wavenumber and ω is fixed by the time variation of the boundary conditions. On substituting from (12.5) into the linear system (12.3), we obtain the following system of linear algebraic equations:

$$\begin{bmatrix} \frac{\lambda}{{Fr_0}^2} & \lambda + 2\frac{\beta_0}{c^2} & \frac{\lambda}{{Fr_0}^2} - \frac{\beta_0}{c^2} \\ 0 & \lambda & \lambda \\ \omega & 2\Phi_T \lambda & 0 \end{bmatrix} \times \begin{bmatrix} \tilde{\eta} \\ \tilde{U} \\ \tilde{D} \end{bmatrix} = \begin{bmatrix} 0 \\ 0 \\ 0 \end{bmatrix}. \tag{12.6}$$

This system admits three linearly-independent, non-trivial solutions, characterized by three different eigenvalues λ_k ($k = 1, 2, 3$), which can be given the form:

$$(\tilde{\eta}_k, \tilde{U}_k, \tilde{D}_k) = \tilde{D}_k (e_k, u_k, 1) \quad (k = 1, 2, 3), \tag{12.7}$$

where the constants $\tilde{D}_k$ are determined by the boundary conditions. The expressions of the eigenvalues λ_k and of the coefficients e_k and u_k are reported in Appendix A. It is worth noting that one solution is of a degenerate type, being characterized by $\lambda = 0$ and by a vanishing perturbation of the bed elevation. From a physical point of view, this solution reproduces a uniform perturbation of flow velocity and depth caused by a change in the water discharge.

The overall solution for the perturbations, say for the bed elevation, is then given by the following linear combination:

$$\eta_1 = \left[\tilde{D}_1 e_1 e^{\lambda_1 x} + \tilde{D}_2 e_2 e^{\lambda_2 x} + \tilde{D}_3 e_3 e^{\lambda_3 x}\right] e^{\omega t} + \text{c.c.} \tag{12.8}$$

The three boundary conditions that are required to compute the unknown coefficients $\tilde{D}_k$ depend on the specific problem under investigation. For example, to analyse the effect of sea level rise, we may consider a perturbation of the downstream water level, with fixed (i.e. unperturbed) water and sediment supplies. Conversely, to study the effect of alterations of the sediment availability, we may impose a perturbation of the sediment discharge at the channel inlet, while keeping the downstream water level unperturbed. For the specific case of the downstream branch of a bifurcation, it is of interest to determine the solution driven by a perturbation of the bed elevation set at the channel inlet, having the form

$$\eta_1 = \eta_1^I = \hat{\eta}^I e^{\omega t} + \text{c.c.} \quad (x = 0), \tag{12.9}$$

while assuming the upstream and downstream water levels unperturbed:

$$\eta_1 + D_1 = 0 \quad (x = 0, \quad x = L). \tag{12.10}$$

Substituting from Equation (12.8) into the boundary conditions (12.9) and (12.10) gives the following linear algebraic system:

$$\begin{aligned} &\tilde{D}_1(e_1 + 1) + \tilde{D}_2(e_2 + 1) + \tilde{D}_3(e_3 + 1) = 0, \\ &\tilde{D}_1(e_1 + 1)e^{\lambda_1 L} + \tilde{D}_2(e_2 + 1)e^{\lambda_2 L} + \tilde{D}_3(e_3 + 1)e^{\lambda_3 L} = 0, \\ &\tilde{D}_1 e_1 + \tilde{D}_2 e_2 + \tilde{D}_3 e_3 = \hat{\eta}^I. \end{aligned} \tag{12.11}$$

The solution of the above system provides the unknown coefficients $\tilde{D}_k$ as functions of the characteristics of the applied perturbation ($\hat{\eta}^I$ and ω) and of the channel

length L. We note that in the limit case of a vanishing perturbation of the inlet bed elevation the trivial (unperturbed) solution is retrieved.

Once the solution is determined, it is possible to compute the associated perturbations of the unit water discharge (q_1) and of the sediment transport capacity (q_{s1}) at the channel inlet, which are fundamental ingredients in the analysis of the evolutionary timescale of bifurcations presented in the next section. By adopting a structure similar to Equation (12.9), we can write those quantities as

$$q_1^I = q_\eta \, \eta_1^I, \qquad q_{s1}^I = q_{s\eta} \, \eta_1^I. \tag{12.12}$$

The expressions of the coefficients q_η and $q_{s\eta}$ are reported in chapter 15.

12.2 COUPLED SOLUTION FOR THE BIFURCATION–DOWNSTREAM CHANNELS SYSTEM

To derive the coupled solution for the bifurcation-downstream channels system we first linearize the nodal point conditions. Recalling the decomposition (12.2), from the water balance (11.5) we obtain:

$$q_{b1} = -q_{c1}. \tag{12.13}$$

Similarly, from the mass balance equations (11.10) and (11.11), by considering the linear terms only, we derive the following relations:

$$2\alpha \frac{d\eta_{b1}^N}{dt} = q_{b1} + q_{sa1}^O - q_{sb1}^I - \frac{2\alpha r}{\beta_0 \sqrt{\theta_0}} \left(\eta_{b1}^N - \eta_{c1}^N \right), \tag{12.14}$$

$$2\alpha \frac{d\eta_{c1}^N}{dt} = q_{c1} + q_{sa1}^O - q_{sc1}^I + \frac{2\alpha r}{\beta_0 \sqrt{\theta_0}} \left(\eta_{b1}^N - \eta_{c1}^N \right). \tag{12.15}$$

Finally, the condition of equal water level H at the entrance of the bifurcates gives

$$H_{b1}^I = H_{c1}^I. \tag{12.16}$$

From a linear perspective, the coupling between the single-channel solution and the nodal point relations is facilitated by symmetry considerations. Specifically, the instability process can be studied by considering a perfectly antisymmetric solution, in which the perturbation in channel c is equal and opposite to that in channel b (i.e. $\eta_{b1} = -\eta_{c1}$, $D_{b1} = -D_{c1}$, $q_{b1} = -q_{c1}$, $q_{sb1} = -q_{sc1}$) and the solution in channel a is unperturbed ($\eta_{a1} = 0$, $D_{a1} = 0$, $q_{a1} = 0$, $q_{sa1} = 0$). It is immediate to verify that this solution satisfies (12.13) and (12.16). Moreover, it implies that once the sediment continuity equation (12.14) for cell b is satisfied, the corresponding continuity equation (12.15) for cell c is also ensured. Finally, if the solution for channel b satisfies the system, the same is also valid for the opposite solution for channel c. These considerations allow us to derive the coupled solution by considering only half of the system (i.e. cell b and channel b).

Given the above specifications, and setting $\eta_{b1}^N = \eta_{b1}^I/2$ according to Equation (11.7), we can express Equation (12.14) in terms of quantities evaluated at the inlet of channel b as:

$$\alpha \frac{d\eta_{b1}^I}{dt} = q_{b1}^I - q_{sb1}^I - 2\frac{r\alpha}{\beta_0 \sqrt{\theta_0}} \eta_{b1}^I, \tag{12.17}$$

while an identical relation is obtained from Equation (12.15) for channel c.

If we consider a perturbation of the bed elevation at the channel inlet of the form (12.9), the associated response of the sediment and water discharges at the inlet can be computed using Equation (12.12). On substituting into Equation (12.17) and simplifying η_{b1}^I we obtain the following dispersion relation:

$$\alpha\omega + 2\frac{r\alpha}{\beta_0 \sqrt{\theta_0}} - q_\eta(\omega) + q_{s\eta}(\omega) = 0, \tag{12.18}$$

which can be numerically solved to determine the complex frequency ω as a function of the parameters of the reference state and of the length of the bifurcates.

The stability of the initial reference configuration depends on the sign of the real part of ω, i.e. on the growth rate Ω. A negative value of Ω implies that the linear perturbation decays over time and the reference state is stable, while a positive value means that the bifurcation evolves towards an unbalanced configuration, characterized by an uneven distribution of the water and sediment discharge in the bifurcates. It is worth noting that for all the unstable cases (i.e. when $\beta_0 > \beta_R$), the imaginary parts of the three eigenvalues λ_k ($k = 1, 2, 3$) and of the complex frequency ω are found to vanish, which implies that the solutions of the problem do not oscillate in space or time. From the linear analysis we then derive the following estimate of the evolutionary timescale of bifurcations:

$$T_{BIF} = \frac{1}{\Omega}. \tag{12.19}$$

13 RESULTS

13.1 TRANSIENT BEHAVIOUR OF BIFURCATIONS

Consistent with the results of previous analyses, both the linear model and the numerical simulations predict that any perturbation of the reference balanced configuration is amplified over time, i.e. its growth rate Ω is positive, when the aspect ratio β_0 exceeds the critical threshold β_R. The latter parameter depends on the values of Shields stress and Chézy coefficient of the reference configuration (as shown in Figure 6 of Redolfi et al., 2019).

In the following, we first outline the morphodynamic evolution of super-critical bifurcations towards their long-term unbalanced configuration, as it results from the outcomes of the numerical simulations. We use the subscripts b and c to denote the "dominant" and "non-dominant" branch, respectively, and we define the discharge asymmetry ΔQ as:

$$\Delta Q := \frac{W_b^* q_b^* - W_c^* q_c^*}{W_0^* q_0^*} = \frac{1}{2}(q_b - q_c)\,. \tag{13.1}$$

As the bed elevation gap between the two cells (i.e. the "inlet step") develops, the water and sediment discharge carried by the dominant branch increase over time, while they both decrease for the other branch. These variations cause an unbalance between the sediment supply and the transport capacity in both branches, leading to aggradation in the non-dominant branch and erosion in the dominant branch.

The morphological evolution of a bifurcation with relatively short branches ($L = 2 \cdot 10^2$) is described in the upper panels of Figure 13.1, which show the bed elevation profiles — plotted at different time steps of the simulation— along with the bed slope of the bifurcates and the discharge asymmetry. From the very beginning of the simulation, as the initial small perturbation starts being amplified, the bed slopes at the inlets of the bifurcates take two diverging trajectories, as shown in Figure 13.1b. Specifically, the inlet bed slope of the aggrading, non-dominant branch increases due to local deposition, while the bed slope at the inlet of the dominant branch decreases due to erosion. The resulting exponential growth (decay) of the bed slope at the inlet of the non-dominant (dominant) branch in the initial stage resembles the typical behaviour of unstable linear dynamical systems. This evidence suggests that the assumption of equal and constant bed slopes, as employed in previous studies, is not fulfilled even for small perturbations of the balanced configuration.

The initial response of the inlet bed slopes provides negative feedback to the water and sediment partition at the node, since a larger bed slope at the inlet of the non-dominant branch increases its ability to capture water and sediments from the node (and vice versa for the dominant branch). As will be shown later, this effect slows down the evolution of the bifurcation, making the resulting timescale much longer than that obtained by assuming the constancy over time of the bed slope of bifurcates.

As the bifurcation further develops, the inlet bed slope of the non-dominant branch reaches a maximum point and then starts decreasing, while the dominant branch keeps eroding, further decreasing its inlet bed slope. Meanwhile, the asymmetry in the water and sediment discharge and the inlet step keep increasing monotonically, and attain values that are close to those corresponding to the long-term equilibrium solution predicted by the BRT model (Figure 13.1c). It is worth noting that this happens before the bifurcates have reached their overall morphodynamic equilibrium, i.e. a constant bed slope and uniform flow conditions.

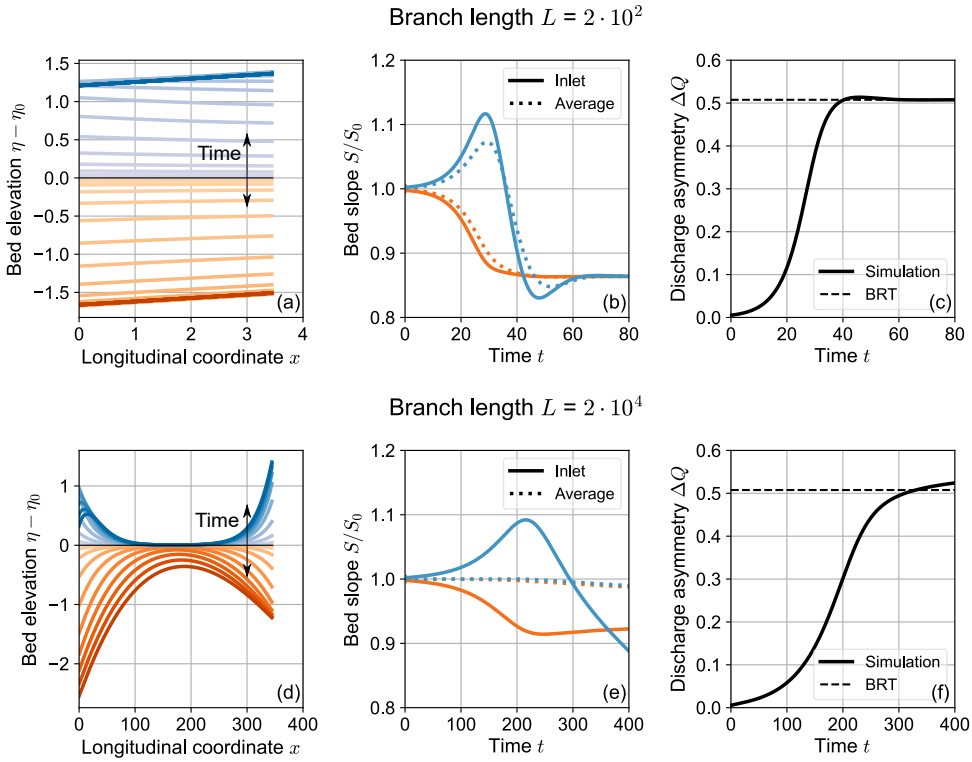


Figure 13.1: Spatio-temporal morphological evolution of the bifurcates in two simulations having the same reference flow and geometry, except for the length of the branches L. The two colours in panels (a,b,d,e) refer to the two bifurcates, namely the aggrading, "non-dominant" branch and the eroding, "dominant" branch. The upper panels illustrate a simulation with short branches ($L = 2 \cdot 10^2$), while the lower panels are referred to a simulation with long branches ($L = 2 \cdot 10^4$). (a,d) The scaled bed elevation profiles of the bifurcates retrieved for different time steps throughout the simulation, obtained by subtracting the initial bed profile η_0. (b,e) The inlet (solid lines) and average (dotted lines) bed slope of the branches, scaled with the reference slope S_0. (c,f) The discharge asymmetry ΔQ (defined in Equation 13.1) between the bifurcates (solid line) and the long-term equilibrium value computed by means of the BRT analytical model (dashed line). The scaled aspect ratio of both simulations is equal to $(\beta_0 - \beta_R)/\beta_R = 0.45$.

In the following stage the partitioning of water and sediment between the bifurcates does not change significantly throughout the simulation, let aside a small "overshoot" with respect to the final equilibrium value. Meanwhile, both branches keep adapting their bed slope to the water and sediment supply delivered by the bifurcation node, progressively evolving towards their long-term equilibrium bed slope, which matches that predicted by the BRT model.

By looking at the evolutionary trajectory of a bifurcation with much longer branches ($L = 2 \cdot 10^4$), reported in the lower panels of Figure 13.1, one can readily see that the evolution of the inlet bed slopes during the first phase of numerical simulations does not change qualitatively with respect to the simulation with shorter branches. Moreover, as in the case of short branches, the discharge asymmetry ΔQ reaches approximately its long-term equilibrium value when the inlet bed slope of the non-dominant branch peaks, therefore well before the overall equilibrium configuration of the bifurcation is established.

Contrary to the evolution of the inlet bed slopes of the bifurcates, the trend of the average bed slopes does show a significant dependence on the length of the branches, due to the spatial variability of the morphological evolution of the bifurcates. For relatively short branches, the aggradation and degradation processes occur homogeneously along the whole length of both branches. Although the variation of the bed slope is larger near the inlet of the branches, as shown by Figure 13.1b, the resulting bed elevation profiles remain almost linear throughout the simulation (Figure 13.1a), leading the inlet and the average bed slope to follow qualitatively similar trends over time. On the contrary, in the case of long branches the aggradation and degradation processes are not uniformly distributed along the branches. In fact, the morphological processes induced in the bifurcates by changes in the water and sediment supply are concentrated near the upstream and downstream end of the branch, leaving the middle reach of the non-dominant branch unperturbed (Figure 13.1d). At the upstream end of the branch, a downstream-migrating depositional wave generates a sequence of concave-up bed profiles. At the same time, the bed elevation at the branch inlet increases over time as the corresponding node cell keeps aggrading. After reaching its peak value, the inlet bed slope of the branch starts decreasing (as in the simulations with shorter branches, Figure 13.1b,e), while the depositional wave further migrates downstream. At the opposite side of the channel, the bed elevation profile is influenced by the downstream boundary condition of constant water level. This condition implies that, as the water discharge decreases, the transport capacity decreases over time near the channel outlet, generating an upstream-migrating depositional wave that reduces the local bed slope. While the two aggradational waves propagate in the non-dominant branch, two analogous albeit erosional waves generate at both ends of the dominant branch (Figure 13.1d), leading its bed elevation profile to become convex upward. Due to the combined, counteracting effect on the local bed slope of these aggradational and erosional waves, the average bed slopes of both bifurcates remain almost constant during the first evolutionary phase of the bifurcation (Figure 13.1e).

The bed elevation profiles observed in the bifurcation with long branches suggest that the morphodynamic evolution of the bifurcates is driven by two distinct unsteady processes, namely the changes in the water and sediment supply determined by the evolution of the bifurcation node and the feedback triggered by the downstream boundary condition. Contrary to the bifurcation with long branches (Figure 13.1d), the bifurcation with short branches shows homogeneous erosion and deposition along its bifurcates (Figure 13.1a), suggesting that the two processes start interacting since the very beginning of its morphodynamic evolution. As discussed in the following, this evidence suggests that the downstream boundary condition and the length of the bifurcates play a relevant role in determining the timescale of bifurcations with short branches.

We note that simulations in which the sediment transport ceases in one branch, as it occurs at large values of the reference aspect ratio β_0, display in the first evolutionary

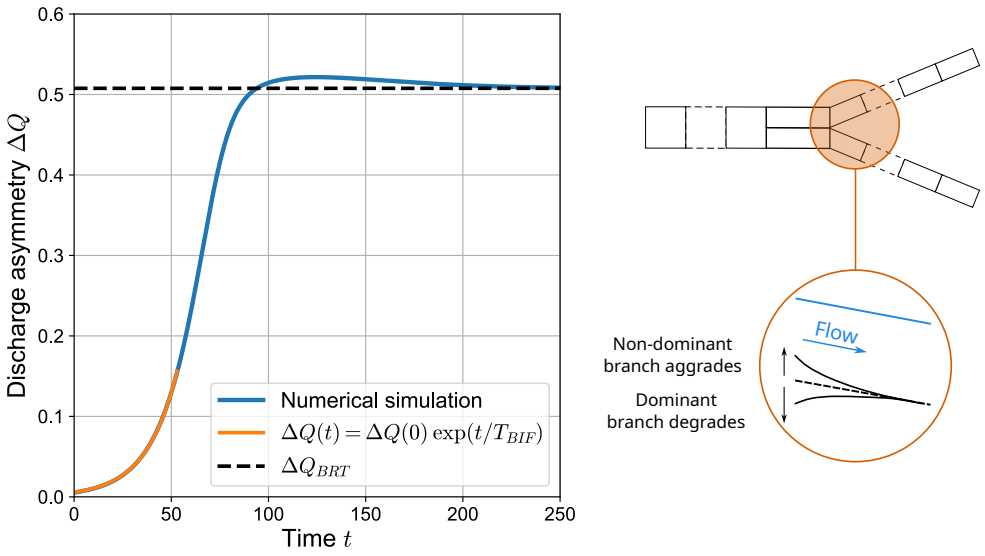


Figure 13.2: Computation of the bifurcation timescale T_{BIF} from the results of numerical simulations: T_{BIF} is computed as the value that makes the exponential function described in Equation (13.2) the best fit for the first stage of the $\Delta Q(t)$ curve returned by the numerical simulation. The sketch in the circle describes the physical process the timescale refers to. Simulation parameters: $L = 1000$, $(\beta_0 - \beta_R)/\beta_R = 0.45$.

stage a behaviour that resembles that described so far for bifurcations where both branches actively transport sediments. However, the long-term equilibrium does not match that predicted by the BRT model and may change considerably with the branch length, ranging from the partial to the complete closure of one branch (Barile, Redolfi, & Tubino, 2024).

13.2 THE BIFURCATION TIMESCALE

Based on the results of the numerical simulations reported in Figure 13.1, the transient behaviour of a bifurcation evolving from an initial balanced unstable configuration to an unbalanced equilibrium configuration can be divided into two phases, each of which is characterized by a specific timescale. Regardless of the length of the bifurcates, the time required by the distribution of the water and sediment fluxes delivered by the node to reach a value close to the final equilibrium is much shorter than that needed to achieve the overall morphodynamic equilibrium of the downstream branches.

If we consider the first phase of the process, an estimate of the inherent timescale (T_{BIF}) of adaptation to equilibrium of water and sediment partitioning at the node can be obtained both on the basis of the linear analysis (Equation 12.19), and by analysing the initial growth rate of the discharge asymmetry retrieved from the numerical simulations. To do so, we compute the timescale T_{BIF} as the value that ensures the best fit between the exponential function

$$\Delta Q(t) = \Delta Q(0)\, e^{t/T_{BIF}} \tag{13.2}$$

and the numerical results (Figure 13.2).

The resulting values of T_{BIF} are reported in Figure 13.3 as a function of the branch length L, for different values of the scaled aspect ratio $\epsilon = (\beta_0 - \beta_R)/\beta_R$, which provides a measure of the distance of the reference aspect ratio β_0 from the critical value for the stability of balanced bifurcations. The results of both the numerical simulations and the analytical model, which exhibit a very good agreement, show

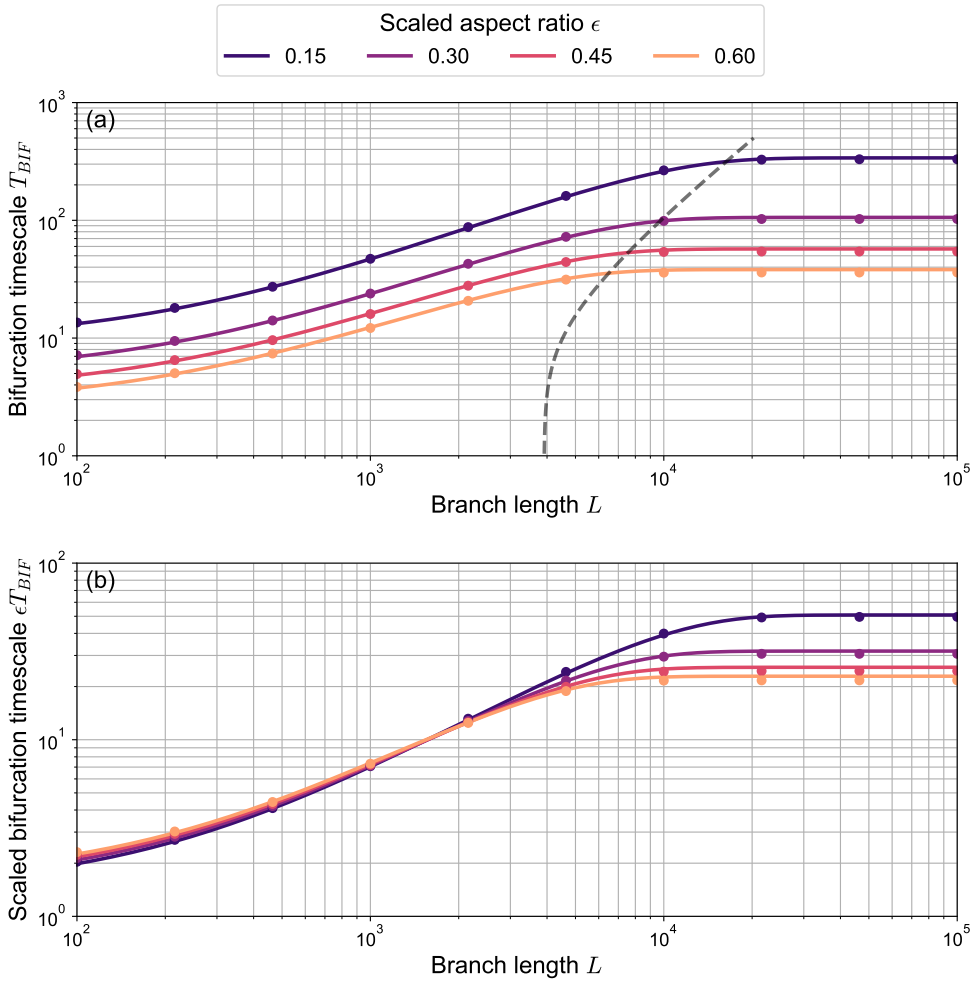


Figure 13.3: Bifurcation timescale T_{BIF} as a function of the dimensionless length of the branches L, for different values of the distance from critical conditions $\epsilon = (\beta_0 - \beta_R)/\beta_R$. Solid lines show the results of the linear model, while dots indicate the values returned by the numerical simulations. The dashed line indicates the "long branches" threshold L_{LB}, as derived by means of the linear model (Equation 13.5). When the timescale T_{BIF} is multiplied by the parameter ϵ, as in panel (b), the curves collapse on a single curve for small values of L.

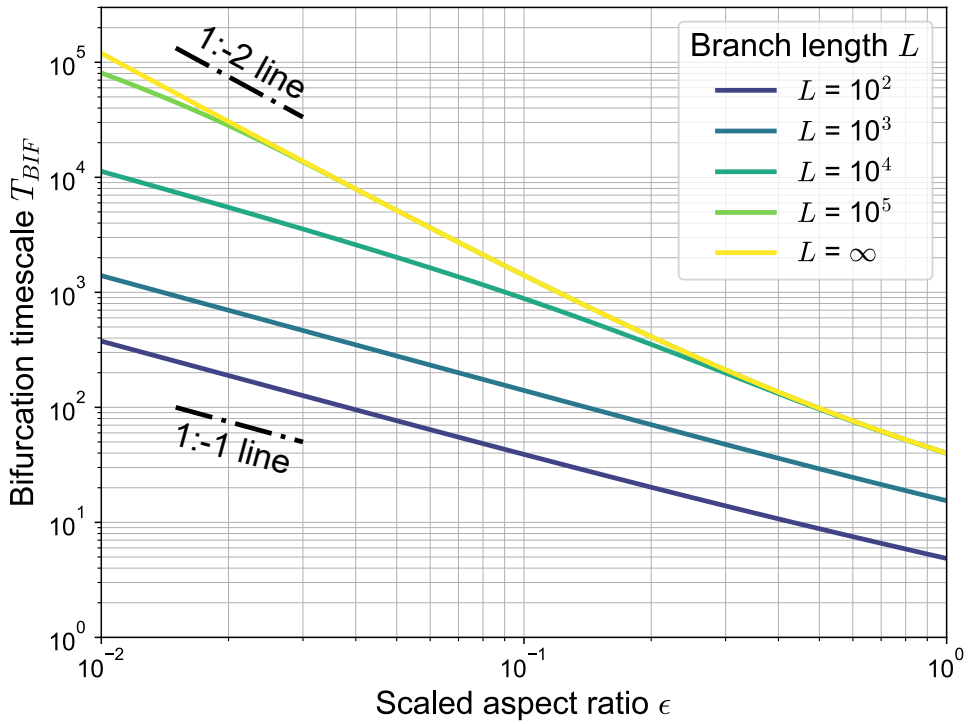


Figure 13.4: Dependence of the dimensionless bifurcation timescale T_{BIF} on the scaled aspect ratio $\epsilon = (\beta_0 - \beta_R)/\beta_R$, computed using the linear model for different values of the dimensionless length of the branches L.

that T_{BIF} decreases as the parameter ϵ gets larger. In the parameter space explored in the Figure ($\epsilon \in [0.15, 0.6]$, $L \in [10^2, 10^5]$), T_{BIF} ranges from 10^0 to 10^2, i.e. 1 to 100 times the Exner timescale (defined as in Equation 11.2).

The bifurcation timescale T_{BIF} markedly depends on the branch length, as highlighted in Figure 13.3. For low values of L, and regardless of the value of ϵ, T_{BIF} exhibits a nonlinear increase with the branch length. We note that in this case the downstream boundary condition affects the morphodynamic evolution of the bifurcates up to their inlet, as shown by panels a-b of Figure 13.1. For longer branches, the curves $T_{BIF}(L)$ reach a plateau for any value of the scaled aspect ratio, revealing that T_{BIF} becomes independent of the branch length. This asymptotic value of T_{BIF} represents the evolutionary timescale of bifurcations with "long branches" (depicted in the lower panels of Figure 13.1), in which the downstream condition does not affect the first evolutionary stage at the inlet of the bifurcates. The above results reveal that the influence of the downstream condition speeds up the adaptation to equilibrium of the water and sediment distribution at the node.

Concerning the dependence of the bifurcation timescale T_{BIF} on the scaled aspect ratio ϵ, Figure 13.3b reveals that by multiplying T_{BIF} by ϵ the residual dependence on ϵ becomes negligible for small values of L, which implies that in the limit of short branches the dependence of T_{BIF} on the scaled aspect ratio is well described by the relation

$$T_{BIF} \sim 1/\epsilon. \tag{13.3}$$

We note that Equation (13.3) implies that as $\epsilon \to 0$ (i.e. as $\beta_0 \to \beta_R$) T_{BIF} goes to infinity, i.e. the growth rate vanishes.

For long branches, T_{BIF} exhibits a different dependence on ϵ, as shown by the logarithmic plot of Figure 13.4, where the relationship between T_{BIF} and ϵ obtained via the linear model is reported for different lengths L of the bifurcates. The curve corresponding to the asymptotic limit of "long branches" ($L \to \infty$) has a slope value of -2 when ϵ is small, which indicates an inverse quadratic dependence of T_{BIF} on

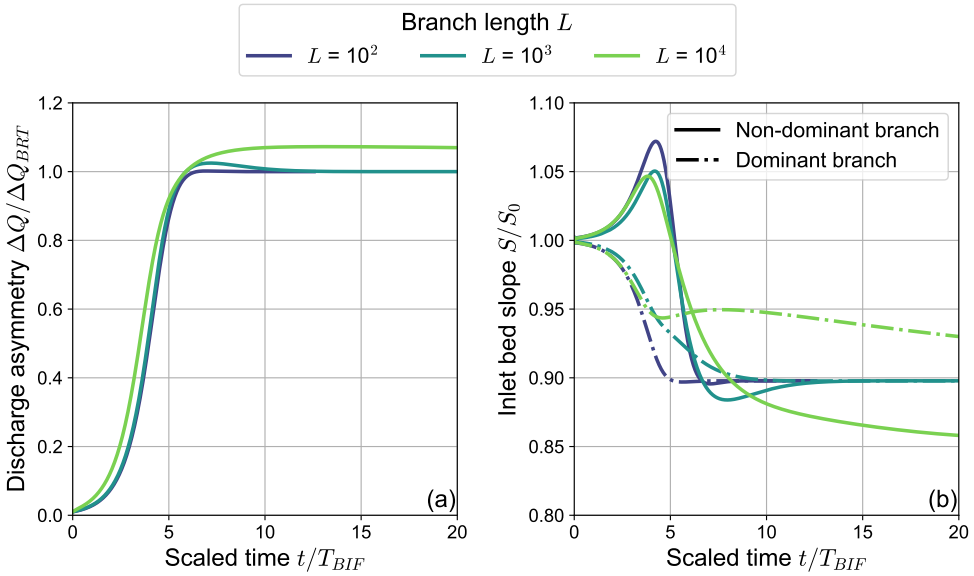


Figure 13.5: Time evolution of (a) the water discharge asymmetry and (b) the bed slope at the inlet of the bifurcates, retrieved from three different numerical simulations, spanning three orders of magnitude for the branch length L. The time variable t is normalized with the timescale T_{BIF}. The scaled aspect ratio of all simulations is equal to $\epsilon = (\beta_0 - \beta_R)/\beta_R = 0.3$.

ϵ. Furthermore, its slope in the log-log plot decreases as ϵ increases, reaching a value between -2 and -1. For low values of L, the curves $T_{BIF}(\epsilon)$ behave according to Equation (13.3) regardless of the value of ϵ. The same behaviour is displayed by the curves corresponding to bifurcations with long branches only at small values of ϵ, while they approach the asymptotic limit of "long branches" as ϵ gets larger.

As outlined in the previous section, simulation results provide clear evidence of the presence of two distinct stages in the transient behaviour of bifurcations. Specifically, the two stages can be identified by analysing the results of numerical simulations in terms of the time variable rescaled by T_{BIF}, as done in Figure 13.5 for the discharge asymmetry ΔQ and for the scaled bed slope S/S_0 at the inlet of the bifurcates. Considering simulations with different values of L (spanning three different orders of magnitude), these curves tend to collapse in the first evolutionary stage, which lasts approximately 5 T_{BIF}. Within this time span, both the inlet step and the discharge asymmetry attain their long-term equilibrium values. On the contrary, the evolutionary trajectories display a marked residual dependence on L in the second stage, during which the downstream branches adapt their slopes to the long-term equilibrium value, while the incoming water and sediment discharge remain nearly constant. Specifically, as described by Figure 13.5b, the longer the branches, the larger the difference between the bed slope resulting from the first phase and that reached in the long term. Therefore, the adaptation process is longer for bifurcations with longer branches.

13.3 INSIGHTS ON THE MORPHOLOGICAL RESPONSE OF THE BIFURCATES

The linear model derived in chapter 12 allows for an in-depth analysis of the transient behaviour of an evolving bifurcation by investigating the role of the two main processes that influence the morphological evolution of the bifurcates, namely the changes in the distribution of water and sediment discharge delivered by the upstream node and the feedback exerted by the downstream boundary condition.

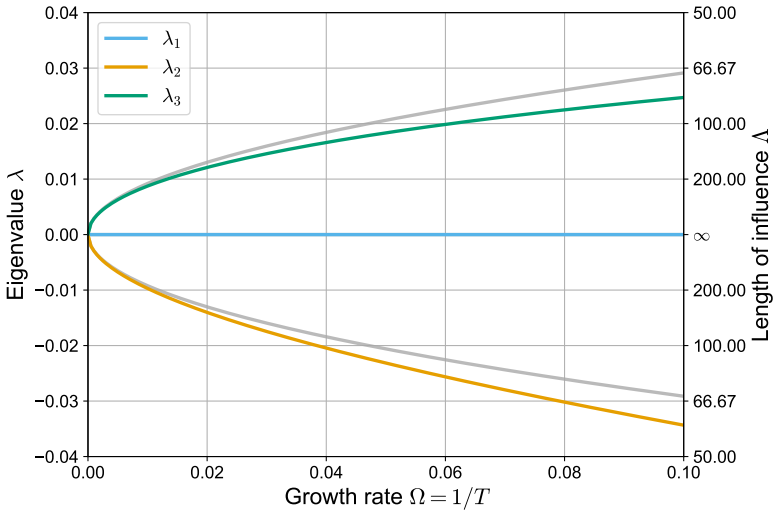


Figure 13.6: The three spatial eigenvalues λ_k $(k = 1, 2, 3)$ and the corresponding lengths of influence Λ_k (computed according to Equation 13.4) as functions of the growth rate $\Omega = 1/T$ of the imposed perturbation (Equation 12.9), considering a vanishing angular frequency χ. When $\chi = 0$ and $\Omega > 0$, all eigenvalues are found to be real (i.e. no spatial oscillations). The gray lines represent the values calculated by means of the diffusive solution.

To do so, we find convenient to explore the response of any of the two downstream branches by separating the effects of the perturbations of the water and sediment supply. Furthermore, we assume that the channel is long enough to prevent the downstream boundary condition from affecting the evolution of the bifurcation node, thus considering the case of a bifurcation with "long" branches.

In general, the linear model allows for setting an arbitrary perturbation of the upstream boundary condition by choosing a value of the complex frequency ω (see Equation 12.1). However, the solution of the dispersion relation (12.18) suggests that in the case of an evolving bifurcation node with $\beta_0 > \beta_R$ the three eigenvalues λ_k $(k = 1, 2, 3)$ and the complex frequency ω are real numbers. We then take $\chi = 0$ and assume an arbitrary and positive value of the growth rate Ω, or equivalently of the timescale $T = 1/\Omega$. We note that in the case of a bifurcation the actual value of the perturbation timescale T corresponds to T_{BIF} and results from coupling the response of the downstream channels with that of the bifurcation node (see chapter 12). Figure 13.6 describes how the three eigenvalues λ_k depend on the growth rate Ω. It is worth noting that λ_2 and λ_3 show similar values but opposite sign, which indicates that the length of influence of the upstream and downstream boundary conditions is comparable. The nearly parabolic shape of the curves suggests that the spatial scale roughly depends on the square root of the timescale, which is a characteristic feature of diffusive processes.

Let us first consider the case of a decrease in the incoming water discharge (for a fixed sediment supply), i.e. of a negative value of the perturbation of the unit discharge q_1^I. The resulting distributions along the channel of the perturbations of flow and bed elevation are reported in Figure 13.7a. We note that the linear solution captures the same features displayed by the results of numerical simulations with long branches (see Figure 13.1d). Specifically, the response of the channel is composed of three distinct phenomena.

1. In the central part of the channel the bed is nearly unperturbed, and the flow remains uniform. However, both the water depth and the flow velocity perturbations are negative, to accommodate the decrease in the water discharge. This effect is associated with the null eigenvalue λ_1, which produces a spatially invariant perturbation.

2. In the downstream part of the channel the bed aggrades to accommodate the downstream boundary condition, which prescribes an unperturbed water surface elevation. Due to the decrease in the water discharge, the downstream water level produces a M1-type backwater profile, which leads to flow deceleration and sediment deposition. Recalling the structure of the linear solution (Equation 12.5), this effect manifests itself as an exponentially decaying perturbation in the upstream direction associated with the positive eigenvalue λ_2.

3. In the upstream part of the channel, the bed aggradation is due to the decrease in the sediment transport capacity, which outpaces that of the sediment supply. The extent of the upstream deposition corresponds to the so-called "boundary layer", as described by Wong and Parker (2006). This effect is associated with the negative eigenvalue λ_3, which produces an exponentially damped solution in the downstream direction.

Unlike the previous case, the effect of a decrease in sediment supply (given a fixed water discharge), i.e. of a negative value of the perturbation of the unit sediment discharge q_{s1}^I, remains confined within the upstream part of the channel, as shown in Figure 13.7b. In this case the only non-vanishing linear solution is that associated with the negative eigenvalue λ_3, which produces local bed degradation and a consequent slight decrease in the water velocity. It is worth highlighting that analogous results are obtained by increasing the water and sediment supply, except for the fact that the sign of all perturbations is reversed. Therefore, for a given value of the timescale T the linear solution for the two bifurcates is identical, except for the sign of perturbations.

The results described above allow us to compute the minimum branch length L_{LB} for which the bifurcation node evolves independently of the downstream boundary condition, i.e. for which the bifurcation displays the "long branches" behaviour. To do so, we define the parameters

$$\Lambda_k = \frac{2}{|\lambda_k|}, \quad k = 2, 3, \tag{13.4}$$

which measure the length of influence of the boundary conditions, i.e. the distance from the downstream (Λ_2) and the upstream (Λ_3) end of the bifurcates, respectively, at which the amplitude of the perturbations produced by the boundary conditions decay by a factor $e^{-2} \simeq 0.135$ (see Figure 13.7). For a given value of the perturbation timescale T, the threshold length L_{LB} can thus be estimated as

$$L_{LB} = \Lambda_2 + \Lambda_3. \tag{13.5}$$

As reported in Figure 13.3a, the "long branches" threshold L_{LB} computed using Equation (13.5) accurately identifies, for the different values of the scaled aspect ratio ϵ, the value above which the bifurcation timescale no longer depends on the length of the branches L. We note that the lengths of influence Λ_2 and Λ_3 increase as the growth rate of the perturbations decreases, as shown in Figure 13.6. Therefore, the smaller the parameter ϵ, the larger the value of L_{LB}. In other words, when the aspect ratio β_0 is closer to the critical value β_R, i.e. for slowly evolving bifurcations, a greater branch length is required to meet the "long branches" asymptotic behaviour.

The response of the downstream branches of an evolving bifurcation is a combination of those displayed in the two panels of Figure 13.7, since both the water and sediment supply change in each bifurcate over time as a result of the evolution of the inlet bed elevation. If we consider the non-dominant aggrading branch, a positive perturbation of the bed elevation (η_1) set at the inlet implies a negative perturbation of the unit water (q_1) and sediment (q_{s1}) discharges, as described in Figure 13.8a. We note that q_1 is constant along the branch, while the reduction in transport capacity, i.e. the absolute value of q_{s1}, locally increases along the upstream and downstream

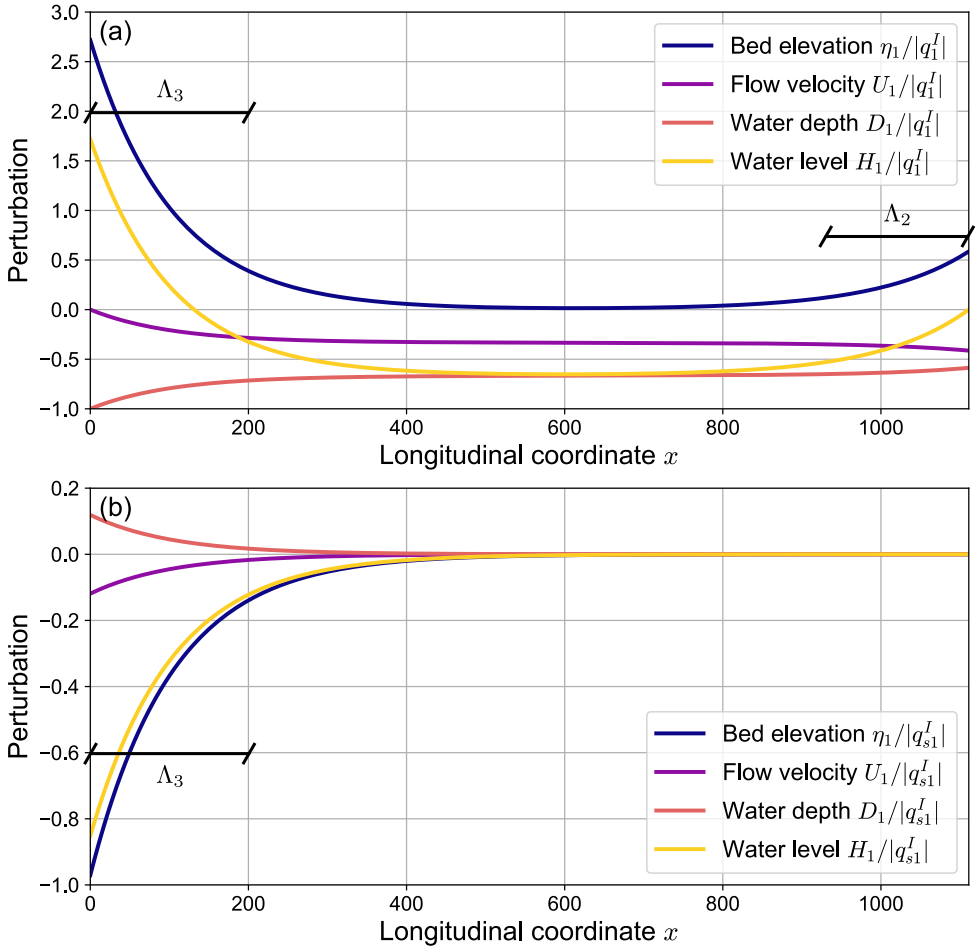


Figure 13.7: Spatial structure of the linear solution for a "long" channel ($L = 2 \cdot 10^4$) subject to a reduction of (a) the upstream water discharge and (b) the sediment supply. The different lines describe the trends along the bifurcate of the perturbations of the bed elevation η_1, flow velocity U_1, water depth D_1 and free-surface elevation H_1, scaled by the absolute values of the imposed (a) unit discharge q_1^I and (b) unit sediment supply q_{s1}^I perturbations at the channel inlet. Example with perturbation timescale $T = 10^2$.

parts of the branch, where bed aggradation occurs. The bed slope perturbation S_1 varies accordingly to the bed profile perturbation, shifting from positive values in the steeper upstream reach to negative values in the milder downstream reach and vanishing in the middle reach, where also the bed elevation is unperturbed.

Overall, the perturbation of the transport capacity is notably larger than that of the flow discharge, as also shown in Figure 13.8b, where the values of q_1 and q_{s1} computed at the inlet of the non-dominant branch are reported for different values of the scaled aspect ratio ϵ. We note that such an overreaction of the transport capacity to changes in the inlet bed elevation is necessary to ensure a positive value of the growth rate, i.e. the evolution of the bifurcation towards an unbalanced state. In fact, when $\epsilon > 0$ Equation (12.18) reduces to:

$$\alpha\Omega = q_\eta - q_{s\eta} - \frac{2r\alpha}{\beta_0\sqrt{\theta_0}}. \tag{13.6}$$

According to Equation (12.12), both q_η and $q_{s\eta}$ are negative functions, because a positive (negative) perturbation of the bed level at the inlet implies a reduction (increase) of the water and sediment discharge in the non-dominant (dominant) branch. As the last term on the right-hand side of Equation (13.6) is invariably negative, this implies that $\Omega > 0$ requires $|q_{s1}| > |q_1|$.

Increasing the value of ϵ, the flow and sediment transport perturbations at the inlet decrease (as well as the difference between the two), while the bed slope gets larger (Figure 13.8c), i.e. the non-dominant, aggrading channel becomes steeper at the entrance. As the scaled aspect ratio ϵ vanishes the inlet bed slope is unperturbed, and the flow is locally uniform (i.e. the bed slope equals the energy slope, Figure 13.8c). This behaviour can be explained by recalling that in the limit $\Omega \to 0$ the length of influence Λ tends to infinity (Figure 13.6). As a result, any perturbation of the bed elevation propagates along the branch without showing any spatial variability. In this case, the solution coincides with that predicted by Miori et al. (2006a).

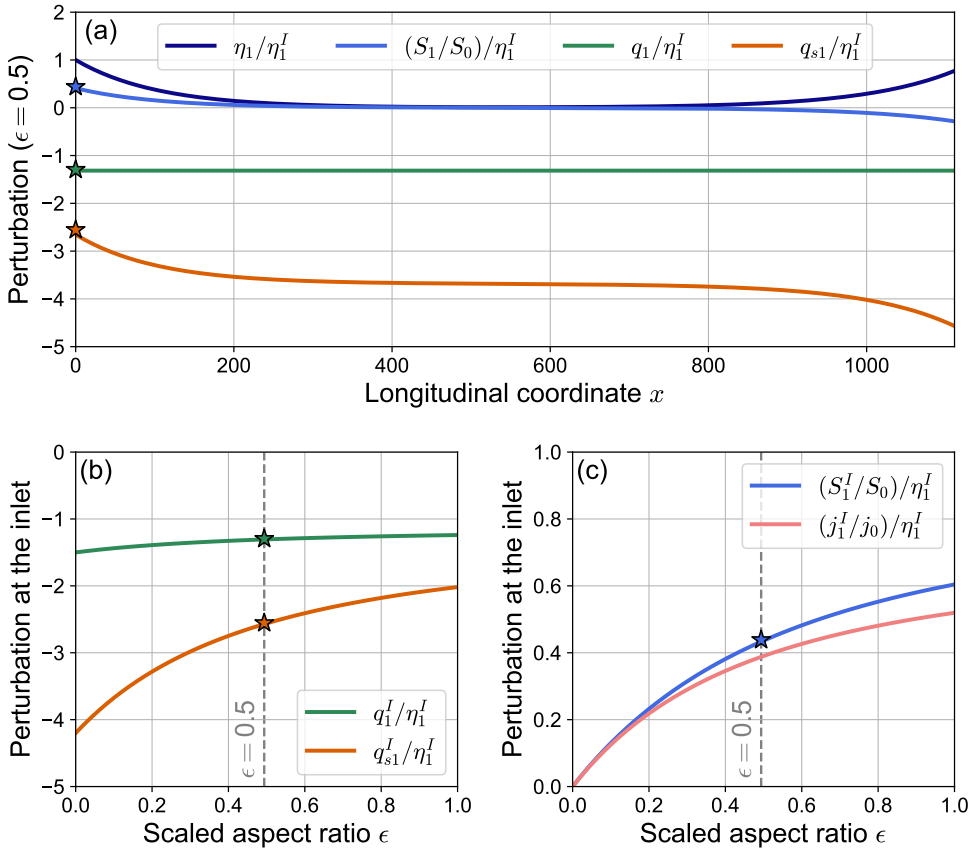


Figure 13.8: The response of the non-dominant branch of an evolving bifurcation, as returned by the linear model. The upper panel (a) shows the trends along the bifurcate of the perturbations of the bed slope S_1, the unit discharge q_1 and the unit transport capacity q_{s1}, associated with a perturbation of the bed elevation η_1 driven by the evolution of the bifurcation node, for a given value of the scaled aspect ratio $\epsilon = 0.5$. The lower panels focus on the perturbations at the inlet of the branch and show the dependence on the scaled aspect ratio ϵ of (b) the unit discharge q_1^I and the transport capacity q_{s1}^I, and (c) the bed slope S_1^I and the energy slope j_1^I. The vertical dashed lines in the lower panels mark the scaled aspect ratio $\epsilon = 0.5$ adopted in the upper panel, which corresponds to a bifurcation timescale equal to $T_{BIF} = 10^2$. In all panels, perturbations are divided by the perturbation of the inlet bed elevation η_1^I; both the bed slope and the energy slope are scaled with the corresponding reference values (S_0, j_0).

14 DISCUSSION AND CONCLUSIONS

14.1 BIFURCATION TIMESCALE AND FLOW VARIABILITY

The results of numerical simulations presented in chapter 13 highlight the existence of two distinct phases in the transient behaviour of bifurcations, the first of which mainly concerns the local evolution of the bifurcation node. After the water and sediment partitioning at the node, as well as the bed elevation gap between the branches, have almost reached their equilibrium values, a second, longer phase develops in which the bifurcates adapt their bed slope to the equilibrium value set by the water and sediment discharge supplied by the node. The identification of these two phases and their respective timescales may help to reconcile the seemingly contradictory results of previous investigations, which had suggested that the (overall) evolution of bifurcations could be either very slow (Gao et al., 2024; Kleinhans et al., 2008) or very fast (Bertoldi, 2012).

The timescale of both phases is found to increase with the dimensionless branch length L, the second phase being increasingly longer than the first. When L exceeds a threshold value L_{LB} the downstream boundary condition no longer affects the adaptation of the water and sediment partitioning, and the evolutionary timescale of the bifurcation node attains a constant value. The analysis of the dataset of bifurcation-confluence units collected by Ragno et al. (2022b), which encompasses more than 60 gravel-bed bifurcations covering a relatively wide range of hydraulic conditions, suggests that this asymptotic condition is hardly met in real-world bifurcations. Their observed average lengths range between $10^2 - 10^3$ times the mean flow depth (Ragno et al., 2022b), while the resulting values of L_{LB} are in the range $10^3 - 10^4$.

In Figure 14.1 we report the dimensional value of the timescale T^*_{BIF} for all the gravel-bed bifurcations included in the dataset. The resulting values span from about 1 h up to several years, with a median value of 129 h. Our results clearly show that T^*_{BIF} decreases with the reference bed slope S_0; moreover, larger values of T^*_{BIF} are typically associated with wider channels. These trends can be explained by recalling that, according to Equation (11.1), we scaled the time variable with the Exner timescale T^*_E (defined in Equation 11.2), which depends primarily on both W^*_0 and S_0. In fact, T^*_E increases linearly with W^*_0, while increasing S_0 gives higher values of the unit transport capacity q^*_{s0} due to the increase in the reference Shields stress.

We note that the typical duration of floods in gravel-bed rivers is much shorter than the values of T^*_{BIF} we estimated, being in the order of several hours. This result implies that single flood events might be unable to produce significant morphological changes at the bifurcation node. Therefore, the long-term response of bifurcations is likely to depend on the average features of the flow regime rather than on the specific sequence of flood events, with different magnitude and duration. In this case, the effect of flow variability on bifurcations can be modelled following an approach similar to that adopted by Carlin et al. (2021) for river bars.

On the other hand, a different response might be displayed by bifurcations in which the timescale is comparable to that of flow variability. This is the case, for instance, of the gravel-bed bifurcations of the Ridanna Creek and of the Sunwapta River analysed by Zolezzi et al. (2006), which are characterized by a strongly daily signal due to glacier melt during summer. The bankfull geometry of the six bifurcations analysed by the authors is described in Table 14.1. They are characterized by a bankfull discharge Q^*_0 in the range $[4.5, 24.7]$ m^3/s, while they show similar values

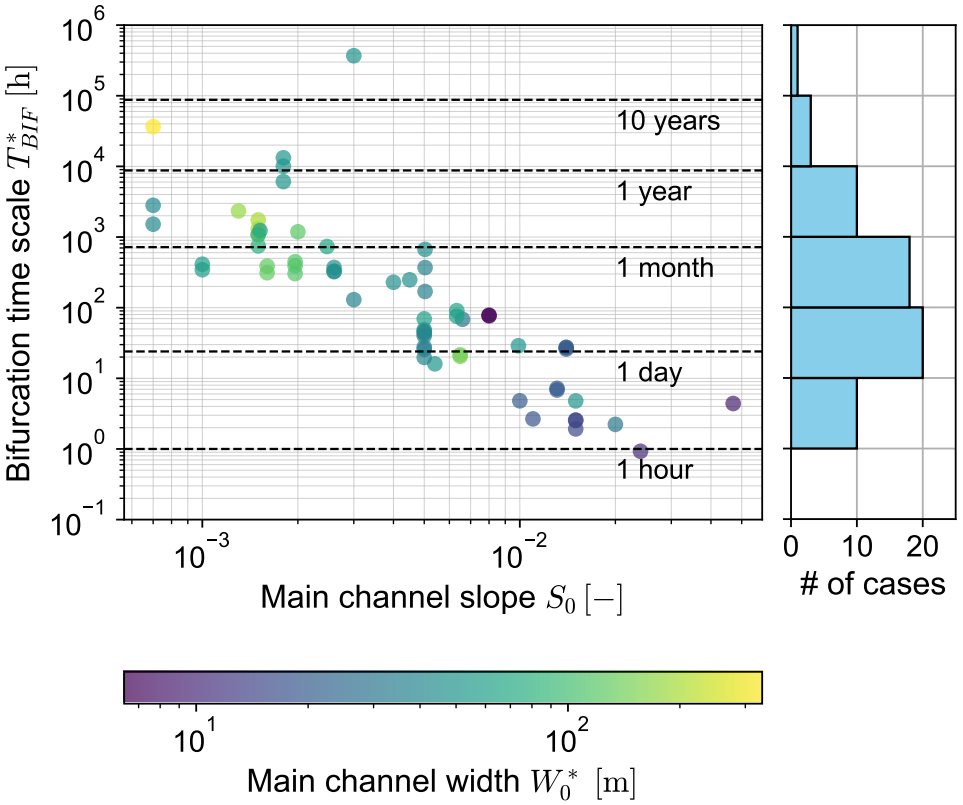


Figure 14.1: Timescale of the gravel-bed river bifurcations included in the dataset by Ragno et al. (2022b), computed by means of the linear analysis as a function of the upstream channel slope S_0. The colour scale indicates the upstream channel width W_0^*.

of channel width $W_0^* \sim 10^1$ m, bed slope $S_0 \sim 10^{-2}$, flow depth $D_0^* \sim 10^{-1}$ m and median grain size $D_{s50} \sim 10^{-2}$ m. Moreover, the lengths of the bifurcates, which we estimated using Figures 12 and 13 of the original article, are in the order of $L^* \sim 10^2$ m, which corresponds to $L \sim 10^2$ according to the scaling (11.1). Let aside one bifurcation in the Ridanna Creek, the length of the bifurcates is considerably lower than the "long-branches" threshold L_{LB}^*, suggesting that the characteristic timescales of these bifurcations might be highly influenced by the downstream conditions. After computing the scaled aspect ratio ϵ, for which we obtained values in the range $\epsilon \in [0.05, 1]$, we derived the dimensional timescale T_{BIF}^* of each bifurcation using the linear model. The resulting values, reported in Table 14.1, suggest that the evolutionary timescale of these bifurcations is typically of the order of a day, thus comparable to that of flow variability.

Table 14.1: Bankfull geometry and timescale of different bifurcations in the Ridanna and Sunwapta pro-glacial gravel bed rivers (data from Zolezzi et al., 2006).

	Rid. 1	Rid. 2	Rid. 3	Sunw. 1	Sunw. 2	Sunw. 3
Q_0^* [m^3/s]	24.7	19.5	6.3	10.3	7.5	4.5
W_0^* [m]	17.4	12.9	9.9	11.3	9.9	8
S_0	0.022	0.017	0.011	0.012	0.014	0.01
D_0^* [m]	0.6	0.68	0.45	0.53	0.44	0.38
D_{s50} [m]	0.1	0.08	0.05	0.04	0.04	0.04
L^* [m]	345	298	144	721	–	471
β_0	14.50	9.49	11.00	10.66	11.25	10.53
θ_0	0.075	0.079	0.053	0.088	0.079	0.058
L	575	438	320	1360	–	1239
ϵ	0.94	0.11	0.73	0.05	0.24	0.50
T_{BIF}^* [h]	1.7	17.3	12.6	133.5	–	16.7
L_{LB}^* [m]	450	2076	804	6300	1517	957

14.2 BIFURCATION TIMESCALE AND BAR EVOLUTION

Among the different forcing factors that may affect the evolutionary trajectories of gravel-bed bifurcations, the fluctuations of sediment supply caused by the migration of bars in the upstream channel play a relevant role (Burge, 2006; Ferguson et al., 1992). The problem has been tackled by Bertoldi et al. (2009), who investigated the role of bar migration on the equilibrium configurations of bifurcations by means of an analytical model and laboratory experiments. While their study focused on the long-term regime configurations arising from the bar-bifurcation interaction, here we analyse this interaction by comparing the timescales of the two processes.

According to Colombini et al. (1987), the formation of migrating bars and their morphometric properties are mainly controlled by the reference aspect ratio β_0. Specifically, bars form when β_0 exceeds a threshold value β_c, which depends on the reference Shields stress and grain roughness. This critical threshold is typically lower than the resonant value β_R (Seminara & Tubino, 1992), which corresponds to the critical threshold for the bifurcation stability. When $\beta_0 > \beta_c$, alternate bars form and migrate downstream with a given celerity, the inverse of which is employed in the following to estimate the timescale T_{BAR} of migrating bars. Moreover, the bar amplitude increases with β_0, slowing down the bar migration (Colombini et al., 1987). As β_0 exceeds a second threshold β_{NM}, this effect leads the bars to stop migrating.

The three threshold values β_c, β_R and β_{NM} define the four regions in the (β_0, θ_0) space depicted in Figure 14.2, each of which identifies a different scenario of interaction between migrating bars and bifurcations. When $\beta_0 < \beta_c$ migrating bars do not

form, and balanced bifurcations are stable. If $\beta_0 \in [\beta_c, \beta_R]$, the flow partitioning at bifurcations is likely to oscillate around an even configuration due to the influence of migrating bars that form in the upstream channel.

Let us now focus on the region $\beta_R < \beta_0 < \beta_{NM}$, in which both T_{BAR} and T_{BIF} are positive, and therefore bars interact with bifurcations evolving toward unbalanced equilibrium states. We first note that the timescales of bifurcation evolution and bar migration both depend on the aspect ratio β_0, but show different trends as β_0 increases. On the one hand, T_{BAR} increases monotonically with β_0, and goes to infinity as $\beta_0 \to \beta_{NM}$. On the other hand, $T_{BIF} \to \infty$ for $\beta_0 \to \beta_R$ and then decreases with β_0. As a result, the timescale ratio T_{BAR}/T_{BIF} vanishes as $\beta_0 \to \beta_R$ and goes to infinity as $\beta_0 \to \beta_{NM}$. Between these two thresholds, the timescale ratio increases monotonically with β_0 for a given value of the Shields stress θ_0.

The value of the timescale ratio is also affected by the length of the bifurcates L, which controls the bifurcation timescale T_{BIF} as described in Figure 13.3. However, changing L does not affect either the threshold values β_c, β_R and β_{NM} or the qualitative trend of T_{BAR}/T_{BIF} across the (β_0, θ_0) space. The role of the branch length emerges clearly when comparing the two panels of Figure 14.2, which show that by increasing L from 10^2 to 10^3 the ratio T_{BAR}/T_{BIF} decreases by nearly four times. However, even for relatively short branches, the timescale ratio remains smaller than 1 throughout the (β_0, θ_0) phase space, except in the region very close to the threshold of no migration β_{NM}, where the ratio tends to infinity. These results suggest that, generally speaking, the adaptation of the water and sediment partitioning at the bifurcation node is slower compared to bar migration. Similarly to the effect of flow variability on bifurcations, when $T_{BAR}/T_{BIF} \ll 1$ the bifurcation evolution is likely to be determined by the time-averaged amplitude and migration speed of bars. On the other hand, when the two timescales are closer, bifurcations can adapt more quickly to the morphological changes induced at the bifurcation node by bars, so that the flow partitioning closely follows the fluctuations in the water and sediment supply caused by bar migration.

Interestingly, the different areas of the (β_0, θ_0) space shown in Figure 14.2 are qualitatively similar to the regions of the same phase space identified by Bertoldi et al. (2009) to distinguish the different types of regime conditions arising from the interaction between migrating bars and bifurcations. Firstly, when $\beta_0 < \beta_c$ migrating bars do not form and bifurcations maintain balanced configurations. Next, when β_0 lies between β_c and β_R, migrating bars might produce periodic oscillations around the stable, balanced solution of the bifurcation, as in the "balanced" regime defined by Bertoldi et al. (2009). In the region $\beta_0 > \beta_R$ migrating bars form and interact with evolving bifurcations, which are expected to develop long-term unbalanced configurations. In this case the behaviour of the system depends primarily on the magnitude of T_{BAR}/T_{BIF}. Specifically, for low values of this ratio the "bar-dominated" behaviour likely prevails; in this regime, migrating bars cause the discharge asymmetry to oscillate around a balanced configuration, even though the intrinsic instability of the bifurcation would produce unbalanced configurations. Increasing the value of T_{BAR}/T_{BIF}, the bifurcation instability becomes dominant, possibly leading to the "bar-perturbed" scenario, in which one branch dominates and migrating bars only produce small oscillations around an unbalanced state.

It is worth highlighting that the interaction between bars and bifurcations does not merely depend on the characteristic timescales, but it is also controlled by the strength of the perturbation exerted by bars, i.e. by the bar amplitude. This effect was considered in the theoretical model of Bertoldi et al. (2009), which, however, did not spatially and temporally resolve the evolution of the downstream branches, and therefore could not account for the dependence of T_{BAR}/T_{BIF} on the branch length L. Further insight could be gained by coupling our unsteady model for the bifurcation and the downstream branches with nonlinear bar theories. We also note that different factors can slow down migrating bars in natural rivers, such as curvature (Tubino & Seminara, 1990) and grain sorting effects (Lanzoni & Tubino, 1999), as well as the

presence of the steady bar that forms upstream super-resonant bifurcations. The latter problem could be investigated by employing a fully two-dimensional model, such as that proposed by Redolfi et al. (2016).

14.3 COMPARISON BETWEEN DIFFERENT MODELS

Our analysis allows us to clarify the limits of validity of various approximate models that have been proposed so far to analyse the morphodynamic evolution of bifurcates. The comparison between the dependence of the evolutionary timescale of the bifurcation node T_{BIF} on the branch length, as predicted by different models, is presented in Figure 14.3.

The "long-branches" approximation corresponds to the asymptotic solution of our linear model for $L \to \infty$. In this case, the solution is simply given by the sum of a spatially decaying solution (associated with the positive eigenvalue λ_3) and a "uniform" perturbation (related to the null eigenvalue λ_1), because the influence of the downstream boundary condition is not felt by the evolving node. This approximation clearly returns a length-independent timescale that matches the asymptotic trend of the linear model when L is greater than the threshold value L_{LB}.

The "diffusive" approximation has been widely used in landscape evolution models, and was adopted by Salter et al. (2018) for modelling the morphodynamics of deltaic bifurcations. The solution is obtained by assuming a locally-uniform flow, which is justified when slope variations are so gentle that backwater effects are no longer relevant, so that flow conditions can be determined by considering the bed slope as a proxy for the energy slope. Therefore, the difference between the complete model and the diffusive approximation decreases as L increases, though never vanishes (Figure 14.3). As shown in Figure 13.6, the diffusive solution matches that of the complete model as $\Omega \to 0$, i.e. as the lengths of influence go to infinity.

The "single-cell" model was used by Bolla Pittaluga et al. (2003) to analyse the stability of the equilibrium solutions. It is based on modelling each downstream channel as a computational cell, characterized by single values of bed slope, water depth and flow velocity. The flow is assumed to be locally uniform, as in the diffusive model, and the channel slope to be constant along the branches, so that spatial variations are ignored. In this scheme, the output fluxes at the downstream end are given by the sediment transport capacity, while the sediment input in the branches is set by the BRT nodal point relation. Since this model considers the evolution of each bifurcate as a whole toward its long-term equilibrium, rather than the local evolution at the bifurcation node, it returns a longer timescale than that computed using our complete model for large values of the branch length (Figure 14.3). For bifurcations with short bifurcates, the single-cell model returns slightly smaller values than our model, due to the lack of spatial variability in its formulation, which prevents it from capturing the negative feedback exerted by the inlet bed slopes of the bifurcates.

A different approximation was introduced by Miori et al. (2006a) in their unsteady model of an evolving bifurcation, which was based on a "local" approach and assumed a constant ratio between the inlet bed slopes of the bifurcates. Like the "single-cell" model, this model does not account for spatial variations, thus neglecting the evolution of the inlet bed slopes and the related negative feedback. Moreover, the solution is given by a perturbation of the uniform flow with a fixed slope. The resulting timescale does not depend on the branch length, due to the local nature of the analysis. Consequently, the computed value is lower than that given by our linear solution and corresponds to that of Bolla Pittaluga et al. (2003) in the limiting case $L \to 0$, as shown in Figure 14.3.

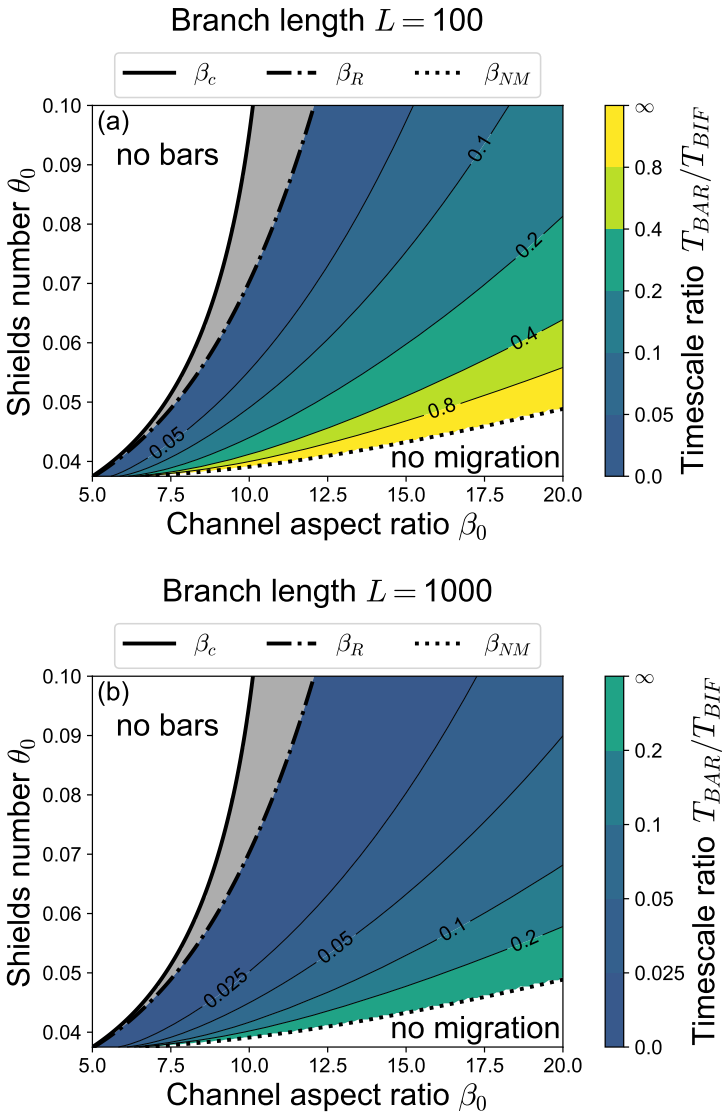


Figure 14.2: Comparison between the bifurcation timescale T_{BIF} and the timescale of bar migration T_{BAR} for different values of the reference aspect ratio β_0 and Shields stress θ_0 and for two values of the branch length L. The solid black lines indicate the critical condition for the formation of migrating bars (β_c), the dash-dotted lines indicate the critical threshold for bifurcation instability (β_R), and the dotted line is the threshold above which bars do no longer migrate (β_{NM}). The gray area between β_c and β_R corresponds to the region where migrating bars coexist with stable, balanced bifurcations.

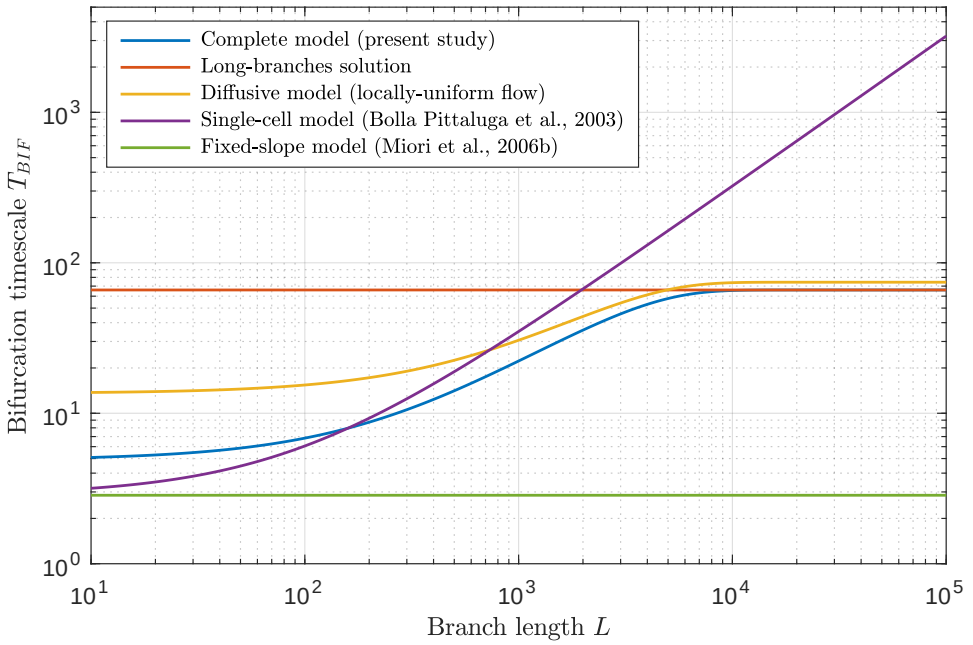


Figure 14.3: Timescale of bifurcation evolution as a function of the branch length L, considering different approaches for modelling the response of downstream branches. The scaled aspect ratio adopted for all models equals $\epsilon = 1.67$.

CONCLUSIONS

In this work, we investigated the transient behaviour of river bifurcations by means of an unsteady one-dimensional morphodynamic model, in which the partitioning of water and sediment is described using the nodal point relation of Bolla Pittaluga et al. (2003). We solved the governing equations using both the numerical scheme recently proposed by Barile, Redolfi, and Tubino (2024) and a novel linear analysis, in which we coupled the nodal point relation with a spatially and temporally varying solution for the downstream branches. The results obtained by means of this modelling framework allow us to draw the following conclusions.

- The water and sediment partition at the bifurcation node evolves on a much shorter timescale than that taken by the bifurcates to reach their long-term equilibrium bed slope.
- The evolutionary timescale of the bifurcation node, once scaled with the timescale of bed evolution set by the Exner equation, decreases as the half-width to depth ratio increases above the critical threshold for the bifurcation stability, while it increases with the length of the bifurcates.
- The condition of water level set at the downstream boundary speeds up the evolution of the bifurcation node when the length of the bifurcates is small. This effect vanishes as the branch length exceeds a threshold value, above which the bifurcation timescale no longer depends on the branch length. This threshold value, which can be predicted by means of the linear model, is found to be larger than the observed values of branch length in natural gravel-bed bifurcations, suggesting that downstream conditions always play a role in their evolutionary process.
- The values of the bifurcation timescale predicted for real-world gravel bed bifurcations span from approximately an hour for relatively narrow and steep reaches up to several years for wide and mild-sloping channels, with a median value of about a week. Hence, the rate of change in the partitioning of water

and sediments at bifurcations is typically much slower than the flow variations associated with the hydrological regime, especially for wide channels.

- The evolutionary process of bifurcations is typically slower than the migration of alternate bars. However, shorter bifurcates and lower values of the Shields stress of the upstream channel may lead the two processes to evolve on similar timescales.

15 APPENDIX: COEFFICIENTS ARISING FROM LINEAR ANALYSIS

The three eigenvalues of the linear system (12.6) can be expressed as functions of basic flow parameters and ω as follows:

$$\begin{aligned}\lambda_1 &= 0,\\ \lambda_{2,3} &= \frac{-\omega\left(1-{Fr_0}^2\right) \pm \sqrt{\omega^2\left(1-{Fr_0}^2\right)^2 + 24\,{Fr_0}^2\,\Phi_T\,\beta_0\,\omega/c^2}}{4\,\Phi_T}.\end{aligned} \tag{15.1}$$

Once these values are determined, the coefficients of Equation (12.7) can be simply calculated as:

$$\begin{aligned} e_1 &= 0, & u_1 &= 1/2,\\ e_{2,3} &= 2\Phi_T\frac{\lambda_{2,3}}{\omega}, & u_{2,3} &= -1.\end{aligned} \tag{15.2}$$

The coefficients $\tilde{D}$ are derived by properly imposing boundary conditions (12.11), which can be synthetically written in the form $\mathbf{A}\times\tilde{\mathbf{D}} = \mathbf{B}$, where the matrices are defined as:

$$\mathbf{A} = \begin{bmatrix} 1 & e_2+1 & e_3+1\\ e^{\lambda_1 L} & (e_2+1)e^{\lambda_2 L} & (e_3+1)e^{\lambda_3 L}\\ 0 & e_2 & e_3\end{bmatrix},\quad \tilde{\mathbf{D}} = \begin{bmatrix}\tilde{D}_1\\ \tilde{D}_2\\ \tilde{D}_3\end{bmatrix},\quad \mathbf{B} = \begin{bmatrix}0\\ 0\\ \hat{\eta}^I\end{bmatrix}. \tag{15.3}$$

The solution of this non-homogeneous linear system gives the following expression for the coefficients:

$$\begin{aligned}\tilde{D}_1 &= \frac{\hat{\eta}^I}{\det(\mathbf{A})}\left[(e_2+1)(e_3+1)e^{\lambda_3 L} - (e_3+1)(e_2+1)e^{\lambda_2 L}\right],\\ \tilde{D}_2 &= \frac{\hat{\eta}^I}{\det(\mathbf{A})}\left[(e_3+1)e^{\lambda_1 L} - (e_3+1)e^{\lambda_3 L}\right],\\ \tilde{D}_3 &= \frac{\hat{\eta}^I}{\det(\mathbf{A})}\left[(e_2+1)e^{\lambda_2 L} - (e_2+1)e^{\lambda_1 L}\right],\end{aligned} \tag{15.4}$$

which turn out to be directly proportional to the coefficient $\hat{\eta}^I$ that represents the magnitude of the perturbation of the inlet bed elevation.

The computation of the coefficients $\tilde{D}_k$ ($k = 1,2,3$) allows for deriving the dimensionless unit flow discharge q and the unit transport capacity q_s at the inlet of the channel as functions of the perturbation $\hat{\eta}^I$. We first note that the problem linearization (12.2) allows for writing q and q_s as

$$\begin{aligned} q &= 1+\delta q_1\\ q_s &= 1+\delta q_{s1}\end{aligned}, \tag{15.5}$$

where q_1 and q_{s1} indicate the perturbations of the two variables q and q_s with respect to the reference flow conditions ($q = 1$, $q_s = 1$). Recalling that the unit discharge is given by $q = UD$ and that the unit transport capacity is defined as in Equation (11.3), our linear approach allows us to write the corresponding perturbations q_1 and q_{s1} as

$$\begin{aligned} q_1 &= U_1 + D_1\\ q_{s1} &= 2U_1\Phi_T\end{aligned}. \tag{15.6}$$

The solution for the perturbation of flow velocity (U_1) and water depth (D_1) can be written in the exponential form described in Equation (12.5), which is a function of the coefficients e_k, u_k and $\tilde{D}_k$ (see Equation 12.7), computed according to Equation (15.2) and Equation (15.4), respectively. By considering the resulting functions for U_1 and D_1 at $x = 0$ and inserting them into Equations (15.6), we can write the inlet perturbations of the unit discharge (q_1^I) and unit transport capacity (q_{s1}^I) as

$$\begin{aligned} q_1^I &= q_\eta \hat{\eta}^I e^{\omega t} + \text{c.c.} \\ q_{s1}^I &= q_{s\eta} \hat{\eta}^I e^{\omega t} + \text{c.c.} \end{aligned}, \tag{15.7}$$

where the expressions for the coefficients q_η and $q_{s\eta}$ read

$$\begin{aligned} q_\eta &= (1+u_1)\frac{\tilde{D}_1}{\hat{\eta}^I} + (1+u_2)\frac{\tilde{D}_2}{\hat{\eta}^I} + (1+u_3)\frac{\tilde{D}_3}{\hat{\eta}^I}, \\ q_{s\eta} &= 2\Phi_T \left(u_1 \frac{\tilde{D}_1}{\hat{\eta}^I} + u_2 \frac{\tilde{D}_2}{\hat{\eta}^I} + u_3 \frac{\tilde{D}_3}{\hat{\eta}^I} \right). \end{aligned} \tag{15.8}$$

Part IV

WATER AND SEDIMENT DIVISION AT DELTAIC BIFURCATIONS: LESSONS FROM THE WAX LAKE DELTA (USA)

ABSTRACT

Bifurcations in river-dominated deltas are the main actors in the routing of water and sediments throughout the fluvial network. In spite of previous acknowledgments of their importance, we still lack a comprehensive framework on how bifurcation geometry affects the water and sediment partitioning. To investigate this issue, we firstly combine previously calibrated 2D hydrodynamic simulations on the Wax Lake Delta with a Lagrangian particle-tracking model, quantifying the partitioning of water and sediments with different buoyancy at five bifurcations and their correlations with differences in channel width, branching angle and inlet bed elevation between the downstream branches. We compare the sediment partitioning at bifurcations with available field data to validate our methodology. We then employ the same modelling tools on a simplified geometry, whose geometrical and hydraulic features resemble those of the bifurcations in the Wax Lake Delta. Model results show that the branching angle does not affect the partitioning of water and sediments. The combined effect of asymmetries in the channel width and inlet bed elevation is captured by a simple linear formula that accurately estimates the partitioning of water at bifurcations returned by the 2D calibrated hydrodynamic simulations. Our results also highlight the key role played by transverse gradients in the bathymetry of the upstream channel in determining the partitioning of sediments, suggesting that deeper portions of the cross-section of the upstream channel can cause a proportionately larger fraction of sediments with larger Rouse number to be routed towards the corresponding bifurcate.

The work presented in this part has been carried out during my four-months research period at the University of Texas at Austin, under the supervision of prof. Paola Passalacqua. The content of this part has been submitted to the Journal of Geophysical Research: Earth Surface and is currently under review. The submitted manuscript has been published as a preprint on the ESS Open Archive. What follows is the version re-submitted to the journal after the first round of review. Reference: Barile, G., Passalacqua, P., Kwon, S., Tubino, M.: Controlling factors on water and sediment partitioning at deltaic bifurcations [preprint], https://doi.org/10.22541/essoar.173159997.71559823/v1, 2024.

16 INTRODUCTION

Understanding how water and sediment split at deltaic bifurcations is crucial to foresee the morphodynamic evolution of river-dominated deltas across a variety of spatial and temporal scales (Edmonds et al., 2022), with noteworthy implications for delta management (Wang et al., 2003). Even if the overall long-term evolution of a delta is sustainable at the system scale, the dynamics of single units such as bifurcations can affect human communities at a smaller scale (Passalacqua et al., 2021), while also influencing the regional evolution of deltas (Kästner & Hoitink, 2020). Bifurcations in deltas manifest different morphometric properties and degrees of asymmetry (Edmonds & Slingerland, 2008), and it is still not clear which factors affect the partitioning of water and sediments and to what extent each factor can drive these divisions and thus the dynamics of the bifurcation.

Up to now, flow partitioning at bifurcations in network models of deltas has been estimated mainly by assuming that the water is split proportionately to channel widths (Tejedor et al., 2015). Hariharan et al. (2022) tested this assumption on a large dataset of field data, suggesting that a linear relationship between width and discharge has a better accuracy compared to other methods that rely on other remotely-sensed quantities. Regarding the division of sediments, several studies on the morphodynamics of branching systems also employed a simplified approach, assuming that the suspended load splits proportionately to water. This assumption was made to study bifurcations in lowland sandy rivers (Edmonds et al., 2011; Iwantoro et al., 2021; Kleinhans et al., 2008) and tested against field data (Dong et al., 2020; Sassi et al., 2013).

Although previous studies acknowledged the first-order control exerted by channel widths, the proposed methods to estimate water and sediment partitioning in complex networks neglect two possibly relevant controlling factors, namely differences in branching angles among the bifurcates and local differences in the bed elevations between the bifurcates. Bathymetric steps between the inlets of the channels are often observed in deltaic bifurcations (Figure 17.2 of the present work; Buschman et al., 2010; Edmonds and Slingerland, 2008) and several authors pointed out their influence on the partitioning of water and sediments at bifurcations, given the same widths of the downstream branches (Le, Crosato, Mosselman, & Uijttewaal, 2018; Meselhe et al., 2016; Slingerland & Smith, 1998). On the contrary, the effect of different branching angles on water partitioning has not been clarified by previous works, although several studies have considered the branching angle of the bifurcates with respect to the centreline of the upstream channel as a possible controlling factor on water partitioning (Burge, 2006; Dong et al., 2020). Specifically, Dong et al. (2020) argued that the branching angle is a good predictor for water partitioning, based on the estimates returned by weighting the channel width with the angle. However, the accuracy of their estimate was comparable to that obtained by simply assuming that the water splits proportionately to channel width. Concerning the partitioning of sediments, several studies discussed the role of different branching angles while analysing the so-called Bulle effect (Bulle, 1926), according to which a disproportionately larger fraction of sediments is routed towards a lateral channel that branches off a straight river reach. This effect has been confirmed by recent numerical (Dutta et al., 2017; Herrero et al., 2015) and analytical (Kästner & Hoitink, 2020) analyses. Consistently with the experimental results by Bulle, these studies suggested that larger branching angles can strongly increase the bedload supply to the side channel (van der Mark & Mosselman, 2013), as confirmed by the experimental results by Szewczyk et al. (2020). However, the Bulle effect is relevant when most sediments are

carried near the bed (Kästner & Hoitink, 2020). Moreover, the above investigations mostly considered bifurcations with no bathymetric steps at the entrance of side channels, consistently with Bulle's experimental setup. Thus, the relevance of these results for the partitioning of suspended sediments at deltaic bifurcations is limited. In fact, several 3D numerical simulations (Gaweesh & Meselhe, 2016; Ksiazek & Meijer, 2011) showed that changing the branching angle of man-made channel diversions does not affect the partitioning of fine silt and sand.

Contrary to the effect of different branching angles, the influence of bathymetric gaps between the bifurcates has been thoroughly investigated for gravel-bed bifurcations, where such steps are often observed in the field (Zolezzi et al., 2006). Laboratory experiments by Bertoldi and Tubino (2007) suggested that, under equilibrium conditions, the ratio between the flow discharges of the bifurcates linearly correlates with the bed elevation gap between the branches. Moreover, their results showed how a bifurcation where the downstream branches have the same width can display different degrees of asymmetry in the flow and sediment partitioning, ranging from a balanced to a strongly unbalanced configuration, up to branch closure. The bathymetry of their laboratory runs (retrieved after the system had reached equilibrium) was later used by Miori et al. (2012) to perform fixed-bed RANS simulations, which confirmed this linear correlation on both the actual bathymetry and on a synthetic geometry that preserved the same step in the bathymetry between the two channels. To evaluate the effects of bathymetric steps on sediment partitioning, Bolla Pittaluga et al. (2003) formulated a physically based nodal-point relationship for the sediment division that accounted for the gravitational effects on sediment transport exerted by transverse bed slopes. However, the relevance of these effects in suspended-load dominated systems has not been analysed yet.

Among other analyses on the division of suspended sediments, the seminal work by Slingerland and Smith (1998) explicitly included suspension in the model formulation. To do so, the authors derived an analytical nodal relationship for bifurcations with a variable bathymetric step. This relationship assumed that only the sediments transported in the upper portion of the water column are diverted into the lateral channel, thus suggesting that, in presence of bathymetric steps, sediments enter the side channel only when they are more distributed over the water column, i.e., when the Rouse number is relatively low. Interestingly, their nodal relationship implies an explicit dependence of the sediment partitioning on the bathymetric step, which however has not been investigated neither by the authors nor by following studies. Generally speaking, the behaviour of sediments with different Rouse numbers and the possible controls on their division at bifurcations still lacks a complete understanding.

In this work, we investigate the dependence on the branching angle, channel width, and bathymetric steps of the partitioning of water and sediments in the suspended-load dominated bifurcations of the Wax Lake Delta (hereinafter WLD). To do so, we firstly analyse the results of previously calibrated hydrodynamic simulations of the WLD to evaluate the influence of width, inlet elevation and branching angle on the division of water at each bifurcation. We then employ a Lagrangian particle-tracking model to evaluate the division of sediments with different buoyancy at each bifurcation, comparing the resulting sediment partitioning against available data on sediment concentration, which we spatialize by means of a partial least squares regression model. Lastly, we employ the same modelling tools to compute the division of water and particles on a synthetic geometry, which we develop taking as reference the geometrical properties of the bifurcations in the WLD. By means of this analysis we evaluate the effect of different branching angles, channel width and bathymetric step on the division of water and sediments, aiming at generalizing our findings to similar fluvial environments.

17 METHODS

17.1 THE ANUGA AND DORADO NUMERICAL MODELS

In the present study, we employed the ANUGA numerical model (Roberts et al., 2015) to solve the 2D shallow-water equations and compute the flow discharge partitioning at bifurcations, both in the Wax Lake Delta and on bifurcations with a synthetic geometry. The model comes in the form of a Python package, and its computational domain can either be retrieved from available bathymetry or generated by means of a built-in module. The governing equations are then solved over time using an unstructured grid with triangular elements. We refer to the ANUGA documentation for further details on the numerical methodology adopted by the model.

To analyse the partitioning of sediments and other particles at bifurcations we employed the Lagrangian particle-tracker model `dorado` (Hariharan et al., 2020). In the following, we will briefly describe the methodology adopted; a more in-depth description of the model can be found in both Hariharan et al. (2020) and in the `dorado` documentation. The `dorado` model requires a priori knowledge of the flow field, which can be retrieved from any 2D hydrodynamic model. In our analysis, we employed the flow field retrieved from the ANUGA simulations, as done in previous studies (Tull et al., 2022; Wright, Hariharan, et al., 2022). Given the flow field, namely the map of the water depth and flow velocity across the domain of interest, the model reprojects the information on a Cartesian grid, in which the particles are then routed. The path of each particle along the grid is computed as a weighted random walk, using an approach similar to the `DeltaRCM` model (Liang et al., 2015). Specifically, the model considers the influence of the local flow direction and water depth to compute the routing direction of each particle. At each time step, the model firstly retrieves the flow direction vector $\widehat{\mathbf{F}}$ for each cell containing a particle as

$$\mathbf{F} = \gamma \, \nabla\eta + (1-\gamma) \, q_w \tag{17.1}$$

where $\gamma \in [0,1]$ is a user-defined parameter, $\nabla\eta$ is the water-surface gradient unit vector and q_w is the momentum unit vector. In `DeltaRCM`, the term γ is needed to account for the effect of local transverse gradients in the free surface on the particle routing direction. However, when using more accurate hydrodynamic models such as ANUGA it is recommended to assume $\gamma < 0.05$, given the reliability of the computation of the inertial terms; here we use $\gamma = 0$ (Wright, Hariharan, et al., 2022). Given the flow direction unit vector of the cell containing the particle, each neighbouring cell i is then assigned a weight w_i, which is computed as

$$w_i = \frac{h_i^\theta}{\Delta_i} \max\left(0, \widehat{\mathbf{F}} \cdot \widehat{\mathbf{d}_i}\right) \tag{17.2}$$

where h_i is the water depth of cell i, Δ_i is the D8 cellular distance (i.e., the Euclidean distance between the centroids of two neighbouring cells), $\widehat{\mathbf{F}} = \mathbf{F}/|\mathbf{F}|$ is the flow direction unit vector, $\widehat{\mathbf{d}_i}$ is the unit vector pointing towards cell i and the exponent θ quantifies the dependence of the downstream routing direction (i.e., of the weight w_i) on the water depth of cell i. Lastly, the weights w_i of the neighbouring cells are normalized by their sum to compute the probability for the particle to be routed towards each of those cells.

In the simulations presented in this work we employed three values for the parameter θ, namely $\theta = (0, 1, 2)$, corresponding to surfactants, water and sand, respectively. It is worth remarking that simulations with $\theta = 1$ also model the

behaviour of passively transported particles, such as solutes and washload (Wright, Hariharan, et al., 2022). Higher values of θ lead to a higher dependence of the particles routing direction on the local water depth, simulating topographic steering effects on the transported sediments. Overall, θ can be considered a proxy for the Rouse number of the transported sediments, as shown by the conceptual model developed by Wright, Hariharan, et al. (2022).

17.2 DEFINITION OF THE ASYMMETRY INDICATORS

In the following, both the water and sediment fluxes and the possible controlling factors of each bifurcation will be described in terms of dimensionless variables indicating the degree of asymmetry shown by the bifurcates. Specifically, we define the generic asymmetry indicator ΔX for the variable X as

$$\Delta X = \frac{X_L - X_R}{X_L + X_R}, \tag{17.3}$$

where the subscripts L and R refer to the left and right branches, respectively. We employ this formulation for the channel width asymmetry ΔW, the angle asymmetry $\Delta\Phi$, the water depth asymmetry ΔD and the water (ΔQ) and sediment (ΔQ_S) asymmetries. Contrary to the other asymmetry indicators, we define the bathymetric step as the difference in the inlet bed elevation of the bifurcates scaled with the sum of their water depths:

$$\Delta\eta := \frac{\eta_L - \eta_R}{D_L + D_R}. \tag{17.4}$$

To compute its value for the analysed bifurcations, we assume the relation

$$\Delta\eta = -\Delta D, \tag{17.5}$$

which can be derived straightforwardly by assuming an equal water surface elevation between the branches. To test this hypothesis, we measured the differences in water level at the inlets of the downstream branches of the bifurcations we analysed, finding that these differences were two orders of magnitude lower than the water depth.

The sign of the generic asymmetry indicator ΔX suggests what would be the "dominant" branch if there were no other factors influencing the water and sediment partitioning. For example, positive values of channel width asymmetry ΔW mean that the left branch is wider, thus more likely to capture the larger fraction of the incoming water and sediments, meaning positive values of the asymmetry indicators ΔQ and ΔQ_S. However, the same relation is not true for the angle and bathymetry asymmetry indicators: in fact, positive values of the angle asymmetry $\Delta\Phi$ mean that the left branch has a higher branching angle, thus less likely to be the "dominant" one. Thus, we use $-\Delta\Phi$ as asymmetry indicator for the angle to look for possible correlations with the water and sediment asymmetry. Analogously, we use $-\Delta\eta$ to evaluate the effect of a step in the bathymetry.

17.3 LOCAL ANALYSIS OF THE BIFURCATIONS IN THE WAX LAKE DELTA

In this study we analyse five bifurcations belonging to the Wax Lake Delta (WLD), located in coastal Louisiana, US (Figure 17.1). Its very recent development started in the 1970s, and resulted from river engineering interventions along the Atchafalaya River (a distributary of the Mississippi River). Despite its anthropogenic origin, the Wax Lake Delta is not currently subjected to anthropic pressures and evolved

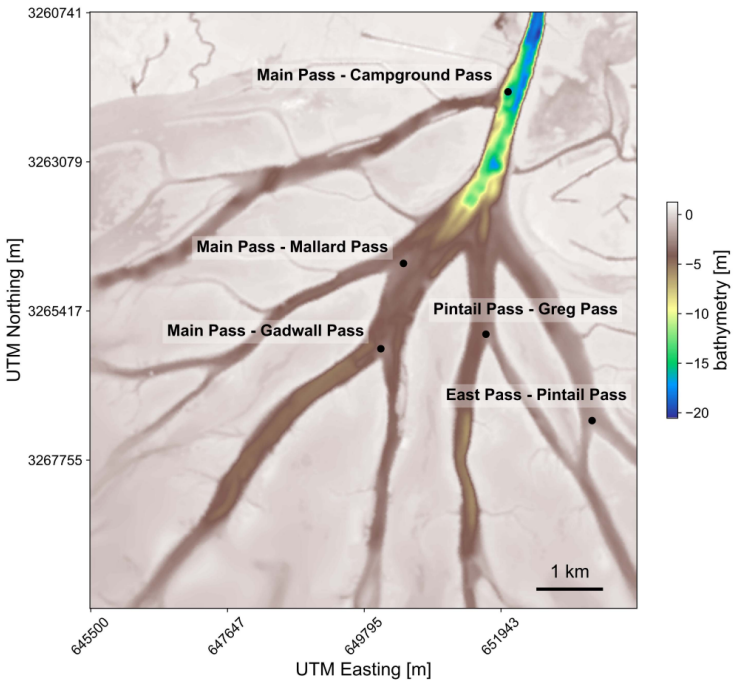


Figure 17.1: Overview of the analysed bifurcations in the Wax Lake Delta. The name of each bifurcation follows the rule "Left Branch - Right Branch", where left and right are defined with respect to the flow direction of the upstream channel. The background image shows the bathymetry data used in this study (Denbina et al., 2020)

spontaneously in the past decades, making it a remarkable case study for future delta management interventions (Kim et al., 2009; Paola et al., 2011). The WLD is considered a river-dominated delta, with a median flow rate at the apex equal to 2900 m^3 s^{-1} (Shaw et al., 2013) and a microtidal range of about 25 cm (Wright, Hariharan, et al., 2022). The distributaries of the delta are characterized by intense sediment transport, which mainly consists of very fine sediments (Nghiem et al., 2023) with a lower fraction of sand (Wagner & Mohrig, 2019). The heavy sediment load has led the different distributaries of the delta to steadily prograde in the past years (Shaw et al., 2018). Thus, the bifurcations analysed in this work are not in equilibrium conditions.

Using the flow field returned by the ANUGA simulations and the outputs of the `dorado` simulations, we focused on five bifurcations in the WLD (Figure 17.1), aiming at evaluating how water and sediments split at each of them and which of their geometrical features is likely to control these partitionings. As potentially controlling factors, we considered differences in channel width, bed elevation at the channel inlet and branching angle. Consistently with the local approach of `dorado`, we limited our analysis to the surroundings of each bifurcation node, using a reference cross-section for each branch. For each bifurcation, we placed the two cross-sections of the bifurcates at the same distance from the bifurcation node. At the inlet of the downstream branches, the bed and water surface elevation profiles along the cross-sections are more irregular than the downstream reaches. Therefore, placing the cross-sections at the very beginning of each bifurcate would affect the accuracy of our estimates of the average channel width and flow depth. For this reason, we placed the cross-section slightly downstream (Figure 17.2), making sure that the distance of each cross-section from the channel inlet was lower than the width of the upstream channel. Given the limited longitudinal variability in the geometry and flow field along the bifurcates further downstream, we do not expect the exact location of the transects to significantly affect our results. This local approach also

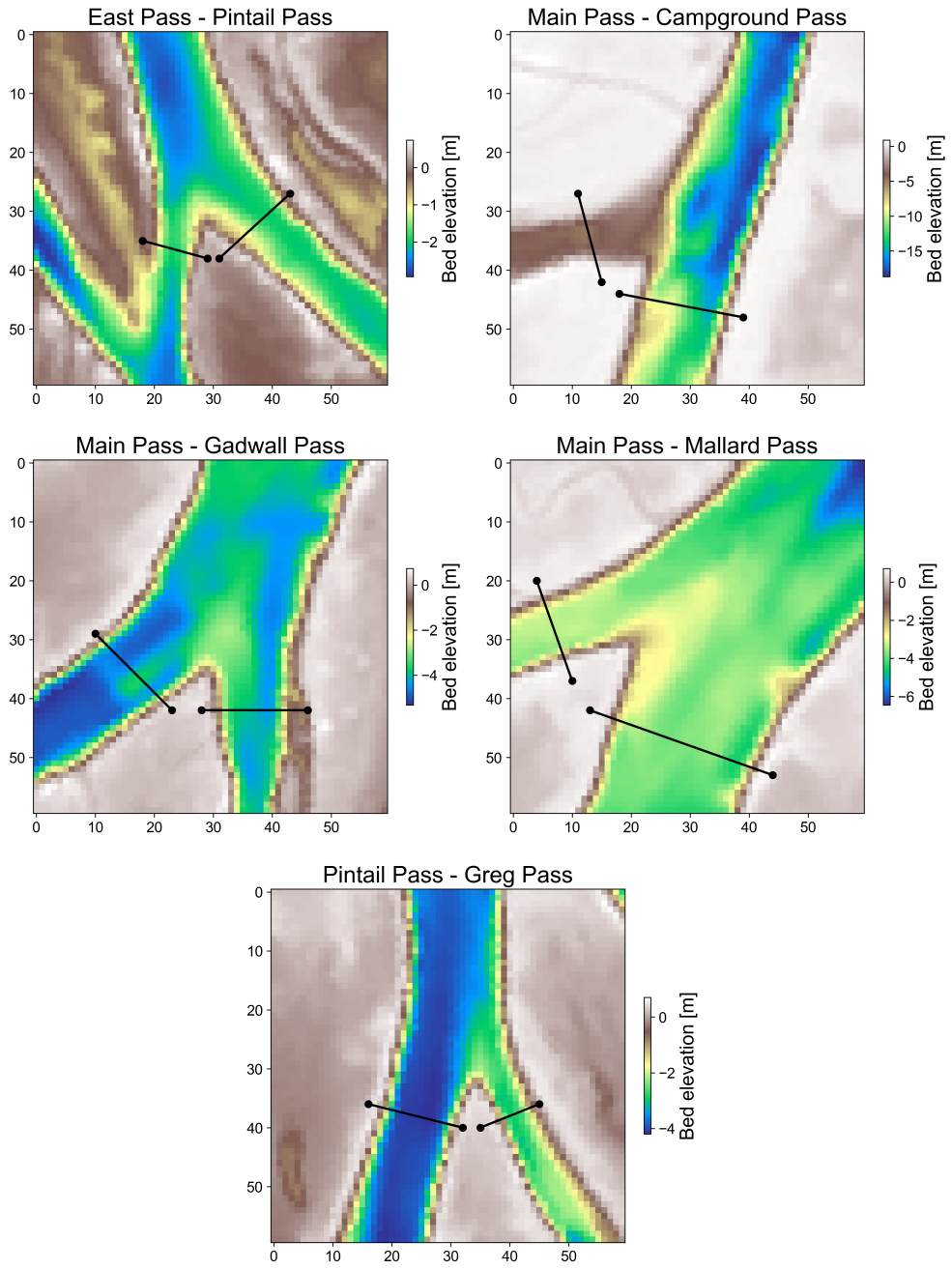


Figure 17.2: Bathymetry of the analysed bifurcations and transects used to compute the average width and depth and the flow discharge of each bifurcate. The bathymetry is the same used by Wright, Hariharan, et al. (2022), which is here reprojected on the Cartesian grid we used for the `dorado` simulations. Note the different boundaries of the colour scale for the bifurcation between Main Pass and Campground Pass, which shows considerably larger gradients in the bed topography compared to the others. The axes refer to the cell number, the size of which is equal to 25 m.

allowed us to neglect the channel-island overbank flow, which may affect the estimate of the flow discharge partitioning between the bifurcates.

For each cross-section, we estimated the channel width, the average water depth and the flow discharge using the bathymetry and flow field returned by the ANUGA numerical model, both projected on `dorado`'s Cartesian grid. First, we identified the "effective" cross-sections corresponding to each transect by excluding the grid cells where the water depth was negligible, discretizing the transects with a spatial step of 1 m. We then computed the top width of the cross-section and retrieved the water depth and flow direction for each point. Lastly, we retrieved the discharge flowing through each transect by numerical integration over the cross-section. Concerning the partitioning of sediments, we used the number of particles crossing a transect during the `dorado` simulations as a proxy for the sediment flux entering each branch.

To compute the bifurcation angles, we used available satellite images and followed the approach proposed by Coffey and Shaw (2017). However, they estimated the angle between the bifurcates, while for the purpose of our study we estimated the angle describing the deviation of the mean flow direction of each branch with respect to the upstream channel, analogously to Dong et al. (2020). Moreover, contrary to Coffey and Shaw (2017), we did not average the angle of each branch over a pre-determined length. Instead, we considered the local orientation of the branch with respect to the centreline of the upstream channel, to better capture possible 2D local effects of the branching angle on the flow field at the bifurcation node, which may influence the particle routing. Contrary to the average local width and depth at the branch inlet, the estimate of the branching angle is not affected by irregular shapes of the bed and water surfaces. Thus, we estimated the local orientation of the inner bank of each bifurcate starting from the bifurcation apex.

17.4 SETUP OF DORADO SIMULATIONS FOR THE WAX LAKE DELTA

To compute the flow field and the water discharge partitioning at each bifurcation, we used the outputs of previously calibrated hydrodynamic simulations performed for the whole Wax Lake Delta by Wright, Passalacqua, et al. (2022); we refer to that publication for further details. The bathymetric map used by the authors has a 10 m resolution and was created by merging data coming from different measurement campaigns in the field (Denbina et al., 2020). The bathymetry was then used to build the unstructured grid, with a spatial resolution of around 25 m for hydrodynamically active areas. The model was then calibrated using water level measurements, both in high-flow and low-flow conditions, corresponding to the NASA's Delta-X project Spring and Fall measurement campaigns, respectively. In the present study we considered one simulation for each campaign: the simulation at high-flow conditions was characterized by a total incoming discharge at the delta apex equal to $Q_{TOT} = 5148.3\ m^3/s$, while in that performed at low-flow conditions the total inflow was equal to $Q_{TOT} = 1646.3\ m^3/s$. We projected the flow field of each simulation on a Cartesian grid with a cell size of 25 m, in order to employ it to run the `dorado` simulations.

For each hydrodynamic simulation we performed different particle-tracking simulations with `dorado`, by releasing a single batch of particles at the apex of the delta and routing the particles until all of them exited the delta. Each batch consisted of 30,000 particles; we chose this number after a dedicated sensitivity analysis, in which we performed a series of simulations on the same flow field with increasing values of the number of particles released. At the chosen value the sediment partitioning at bifurcations stopped changing with the number of particles. We ran three sets of `dorado` simulations corresponding to three values of its parameter θ, in order to estimate how surfactants, water and sand split at each bifurcation. We used the

flow field associated with a single time step of the ANUGA simulation for both the high-flow and low-flow conditions, thus neglecting the effect of tides and daily variations of the inflow discharge on the partitioning of particles. While we expect the tidal influence to be non-negligible in low-flow conditions and for bifurcations closer to the delta foreset, variations in the incoming flow discharge showed a negligible influence on our results, as will be described in the following sections. Lastly, we checked that the number of particles exiting the upstream channel was equal to the sum of those entering the downstream branches, to make sure that the overbank flow of particles did not affect the estimate of the partitioning.

17.5 COMPUTATION OF SEDIMENT FLUXES FROM TOTAL SUSPENDED SOLID MEASUREMENTS IN THE WAX LAKE DELTA

To validate the sediment partitioning at bifurcations simulated by `dorado`, we estimated the suspended sediment load (SSL) using remote sensing data and the ANUGA simulations. Specifically, we used the Suspended Sediment Concentration (SSC) maps estimated from NASA's Airborne Visible–Infrared Imaging Spectrometer-Next Generation (AVIRIS-NG) during the Spring and Fall 2021 campaigns of NASA Delta-X (Fichot & Harringmeyer, 2023). These maps, which we retrieved using a partial least squares regression (PLSR) model, provide high-resolution (< 5 m) surface SSCs within 0.5 m of the water surface (Harringmeyer et al., 2024). Additionally, following the index concentration method (Santini et al., 2019), we converted the remotely sensed SSC to depth-averaged SSC by multiplying it by a ratio (=1.27) between surface and depth-averaged SSCs, estimated from in-situ measurements at WLD (Nghiem et al., 2025).

We then computed the sediment fluxes by multiplying velocity and water depth distributions during the flight time of AVIRIS-NG given by the calibrated ANUGA model to the depth-averaged SSC maps. For this computation, we reprojected ANUGA's results into SSC maps to match the spatial dimension. These sediment flux maps show detailed partitioning patterns under conditions dominated by river plumes (Spring, Figure 17.3) and tides (Fall). The flux maps of the whole area for both campaigns are reported in chapter 21.

To compute the SSL for each bifurcate, we generated transects perpendicular to the channel centrelines at 50 m intervals, restricting their lengths based on the water surface area identified by AVIRIS-NG. We then horizontally integrated the flux values across each transect. The channel width was then estimated from the water surface area identified by AVIRIS-NG. This approach provides continuous SSL estimates along the distributary channels within WLD. Lastly, we computed the average SSL for each channel considering a 600 m stretch both upstream and downstream of the bifurcation transects (Figure 17.1). We then used the resulting average SSL to calculate the sediment partitioning ΔQ_S^{RS} for each bifurcation according to Equation (17.3), using the average SSL of each channel to evaluate the sediment flux of each branch, i.e., using the formula

$$\Delta Q_S^{RS} = \frac{SSL_L - SSL_R}{SSL_L + SSL_R} \tag{17.6}$$

where SSL_L and SSL_R are the average SSL of the left and right branch, respectively. To determine the uncertainty in the resulting values of ΔQ_S^{RS}, we applied error propagation of the SSLs of the bifurcates (SSL_L, SSL_R) and total upstream sediment

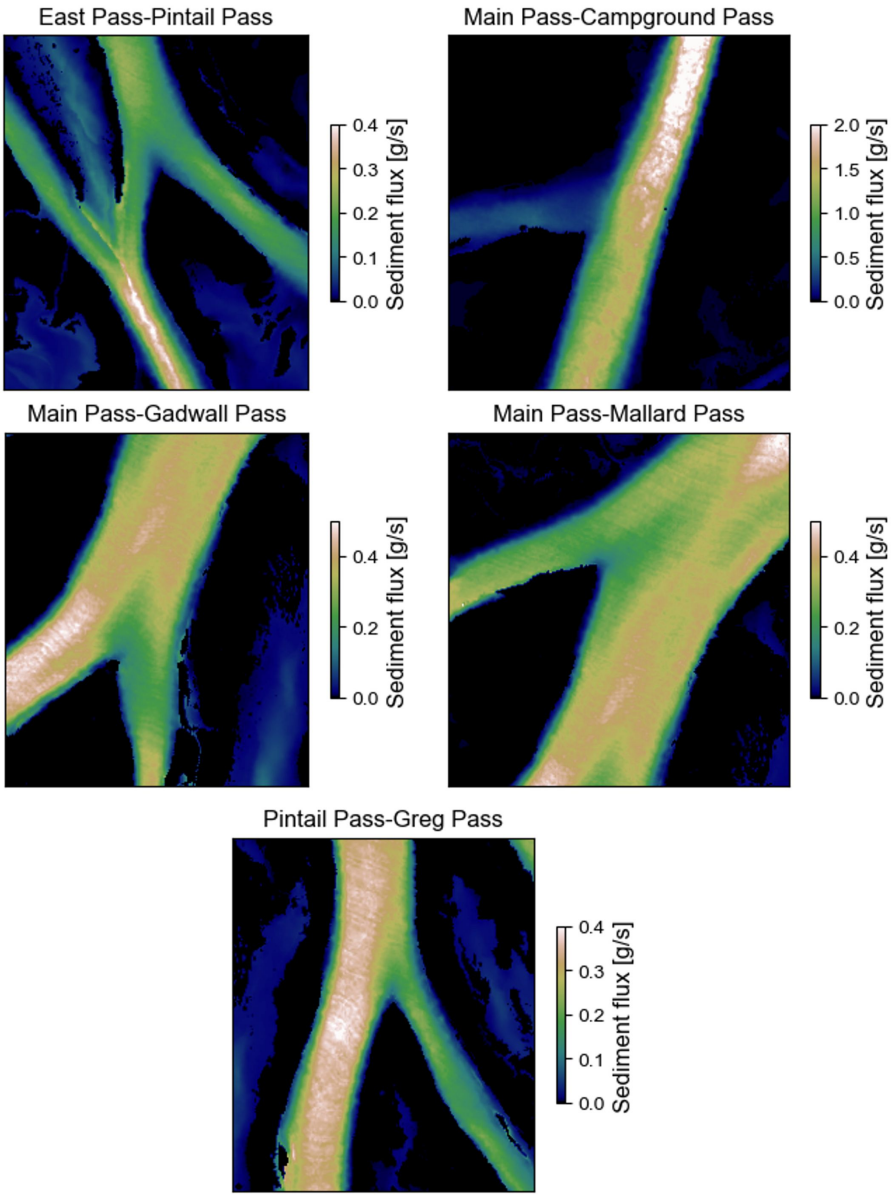


Figure 17.3: Estimated suspended sediment flux of the analysed bifurcations in the Spring campaign. Note the different colour scale for the Main-Campground bifurcation.

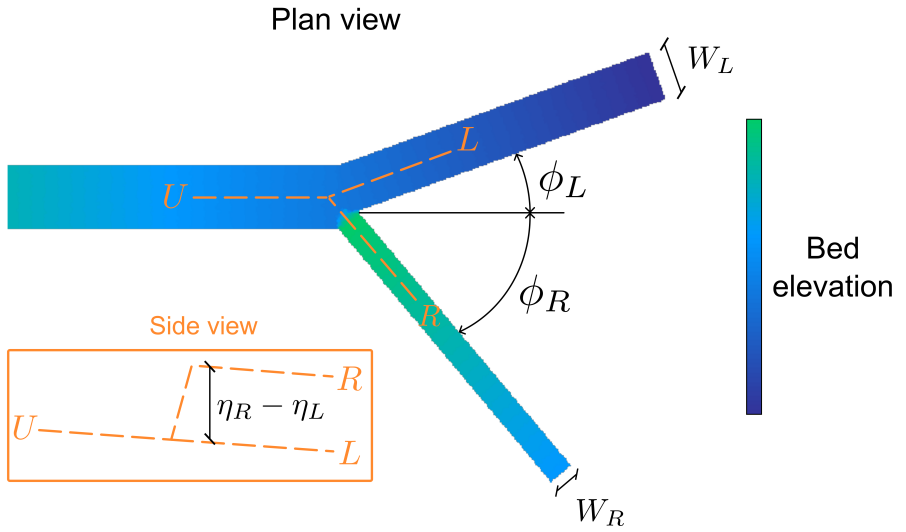


Figure 17.4: Plan and side views of the synthetic geometry, showing the bathymetry with a step with a height $\eta_R - \eta_L$ at the inlet of the narrower channel. The schematic is not to scale.

load SSL_U (=$SSL_L + SSL_R$) in Equation (17.6) to compute the standard deviation (Ku, 1966) as follows:

$$\sigma_{\Delta Q_S^{RS}} = \sigma_{\frac{SSL_L - SSL_R}{SSL_U}} = \frac{\sqrt{\sigma^2_{SSL_L} + \sigma^2_{SSL_R} + \left(\frac{\mu_{SSL_L} - \mu_{SSL_R}}{\mu_{SSL_U}}\right)^2 \sigma^2_{SSL_U}}}{|\mu_{SSL_U}|}, \tag{17.7}$$

where $\sigma_{\Delta Q_S^{RS}}$ is the standard deviation of the sediment partitioning ΔQ_S^{RS}, σ_{SSL_L}, σ_{SSL_R}, and σ_{SSL_U} are the standard deviations of SSL_L, SSL_R, and SSL_U respectively, and μ_{SSL_L}, μ_{SSL_R}, and μ_{SSL_U} are their respective mean values. The term $\left(\frac{\mu_{SSL_L} - \mu_{SSL_R}}{\mu_{SSL_U}}\right)^2 \sigma^2_{SSL_U}$ accounts for the contribution of the standard deviation of SSL_U to $\sigma_{\Delta Q_S^{RS}}$, and $|\mu_{SSL_U}|$ normalizes the overall standard deviation.

17.6 SIMPLIFIED GEOMETRY

In order to extend our results to other deltaic contexts, we employed the same numerical tools we used for the Wax Lake Delta on a domain representing an idealized deltaic bifurcation, which we generated using an ANUGA's built-in module. This simplified geometry allowed us to broadly explore the parameter space defined by the different geometrical properties of bifurcations, and to identify the potentially governing factors on water and sediment partitioning. First, we fixed some of the main geometric and hydraulic parameters of the reference bifurcation (reported in Table 17.1) so that it could resemble those of the Wax Lake Delta. Then, we generated 126 different configurations to explore the different combinations of the potential governing factors ΔW, $\Delta\eta$ and $\Delta\Phi$, considering the ranges shown by the bifurcations in WLD (and reported in Figure 18.1). We performed an ANUGA simulation for each configuration assuming a constant inflow discharge, and extracted the resulting long-term equilibrium flow field. We then used this flow field to perform three `dorado` simulations for each configuration, corresponding to the same three values used for the WLD bifurcations (i.e., $\theta = 0, 1, 2$). Lastly, we computed the water and sediment partitioning using the same procedure adopted for the bifurcations in the Wax Lake Delta. In the following, we provide further details on the geometry of the different configurations of the simplified geometry and on the boundary conditions adopted.

Table 17.1: Fixed geometrical and hydraulic parameters of the generated domains used for all numerical simulations on the synthetic geometry. See Figure 17.4 for a visual representation of the geometrical variables W and Φ.

Upstream channel width W_U	500 m
Total width of the bifurcates $W_L + W_R$	600 m
Channels bed slope S_U	10^{-5}
Flow discharge Q_U	883 m^3/s
Manning coefficient n	0.012 s $m^{-1/3}$
Total bifurcation angle $\Phi_L + \Phi_R$	70°

The channels composing the synthetic bifurcations were all characterized by a rectangular cross-section and constant bed slope S_U and Manning coefficient n. As boundary conditions, we fixed a constant inflow Q_U to the upstream channel and a transmissive boundary condition at the downstream end of the bifurcates. To determine the input flow discharge Q_U, which was kept constant for all configurations, we first performed a linear fitting of the correlation between channel width and flow discharge for the bifurcates of the WLD, using the outputs of the high-flow ANUGA simulation. We then computed the value corresponding to the chosen width of the upstream channel $W_U = 500$ m. To define the planform geometry of the bifurcates, we first estimated the average local widening at bifurcations in the WLD, i.e., the sum of the widths of the downstream channels scaled with the width of the upstream channel. We then used the resulting value (=1.2) to retrieve the total width of the bifurcates $W_L + W_R = 600$ m. Regarding the branching angles of the downstream channels, we assumed their sum to be constant and equal to 70 degrees. This value is representative of deltaic bifurcations, as shown by the analysis by Coffey and Shaw (2017). It is worth noting that, as outlined by previous numerical studies (Thomas et al., 2011), the sum of the branching angles does not influence the water partitioning.

The simplified geometry features an upward ramp at the inlet of the narrower channel with a variable height $\eta_L - \eta_R$ (Figure 17.4), resembling the bathymetric step we observed in some of the bifurcations in the Wax Lake Delta (e.g., the Main Pass-Camp ground Pass and the Pintail Pass-Greg Pass bifurcations, Figure 17.2). Following the results by Miori et al. (2012), we assumed this simplified implementation of bathymetric steps to be representative of those observed in the field. According to the bathymetry of the Wax Lake Delta, steps in the riverbed elevation are found only in bifurcations with evident differences in the downstream channel widths. Furthermore, in these bifurcations the narrower channel always has a higher inlet bed elevation, while the bathymetry of the wider channel shows no discontinuities with that of the upstream channel. Consistently with these observations, we explored the effect of bathymetric steps only on bifurcations with $\Delta W \geqslant 0.3$, and we set the bed elevation at the inlet of the wider channel to be equal to that at the outlet of the upstream channel. We defined the height of these steps by means of the asymmetry indicator $\Delta\eta$, which we computed a posteriori for each configuration using Equation (17.5). The resulting values of $\Delta\eta$ were found to be in the range $(0, 1/3)$, which includes the values of $\Delta\eta$ observed in the WLD except for the Main-Campground bifurcation (Figure 18.1).

We note that our simplified geometry does not include transverse gradients in the bathymetry of the upstream channel, although they are observed in the bathymetry of the WLD bifurcations (Figure 17.2). By making this choice we aimed at evaluating whether the flux partitioning mainly depends on the geometry of the downstream channels, as argued by previous studies on the partitioning of water and sediments at bifurcations (Dong et al., 2020; Slingerland & Smith, 1998). However, transverse gradients in the bathymetry of the upstream channel could affect the partitioning of sediments, as suggested by previous works on bifurcations in gravel-bed rivers (Bolla Pittaluga et al., 2003).

18 RESULTS

18.1 BIFURCATIONS IN THE WAX LAKE DELTA

18.1.1 Asymmetries computed using ANUGA and `dorado`

Based on the results of the 2D hydrodynamic simulations performed with ANUGA, we firstly computed the flow discharge partitioning ΔQ for the analysed bifurcations. Then, we used the results of the `dorado` simulations to retrieve the particle partitioning ΔQ_S at each bifurcation for the different values of `dorado`'s parameter θ. We recall that, according to the formulation of the `dorado` model, the particle partitioning obtained by using $\theta = 1$ corresponds to the partitioning of both water and passively transported sediments. Given the resulting values of ΔQ and ΔQ_S for the five bifurcations, we looked for possible correlations with the differences in the channel width, branching angle and inlet bed elevation among the bifurcates (Figure 18.1).

Concerning the water discharge asymmetry ΔQ, a first relevant result is that bifurcations with larger width and depth asymmetry consistently show a more unbalanced partitioning of water. The only exception is the Main-Gadwall bifurcation, which shows a remarkable asymmetry in the water partitioning while having a negligible difference between the channel widths and a relatively small bathymetric step (compared to other bifurcations). This counter-intuitive result can be explained by considering that Main Pass narrows considerably further downstream, possibly causing backwater effects that affect the water partitioning.

Regarding the bifurcation angle, in three out of the five analysed bifurcations the downstream channels have similar branching angles, resulting in a negligible angle asymmetry $\Delta\Phi$. Interestingly, the left channel of the Main-Gadwall bifurcation (i.e., Main Pass) has a larger branching angle, while it carries the larger fraction of the incoming flow discharge. On the other hand, the opposite happens for the Main-Campground bifurcation, where the non-dominant branch (i.e. Campground Pass) has both a larger branching angle and a lower flow discharge. Overall, these results suggest that there is not a correlation between a difference in the branching angles between the bifurcates and the asymmetry in the flow discharge partitioning.

Concerning the particle partitioning, the division of passively transported sediments (i.e., `dorado` simulations with $\theta = 1$) matches that of flow discharge returned by ANUGA simulations, consistently with `dorado`'s model formulation. Regarding the effect of θ, we observe that larger values may either increase or decrease the asymmetry of the particle partitioning ΔQ_S. Specifically, ΔQ_S increases for the Main-Campground, Main-Mallard and Pintail-Greg bifurcations, meaning that the partitioning of coarser sediments ($\theta = 2$) is more unbalanced than that of water ($\theta = 1$). This increase is consistent with the bathymetric step among the bifurcates: by increasing the dependence of the particles preferential routing direction on the water depth, i.e., by increasing θ, a larger fraction of the incoming particles are routed towards the deeper channel, leading to an increase in ΔQ_S. We note that the results of our `dorado` simulations for these bifurcations are consistent with the field observations performed by Shaw et al. (2013), who estimated the bedrock exposure and identified sand deposits in different branches of the Wax Lake Delta by means of boat-mounted sensors. For each of the three bifurcations, they found evidence of sand deposits in the dominant branch and percentages of bedrock exposure close to unity in the non-dominant branch, suggesting a strongly asymmetric partition of sand with respect to water. This finding is consistent with our estimates of the

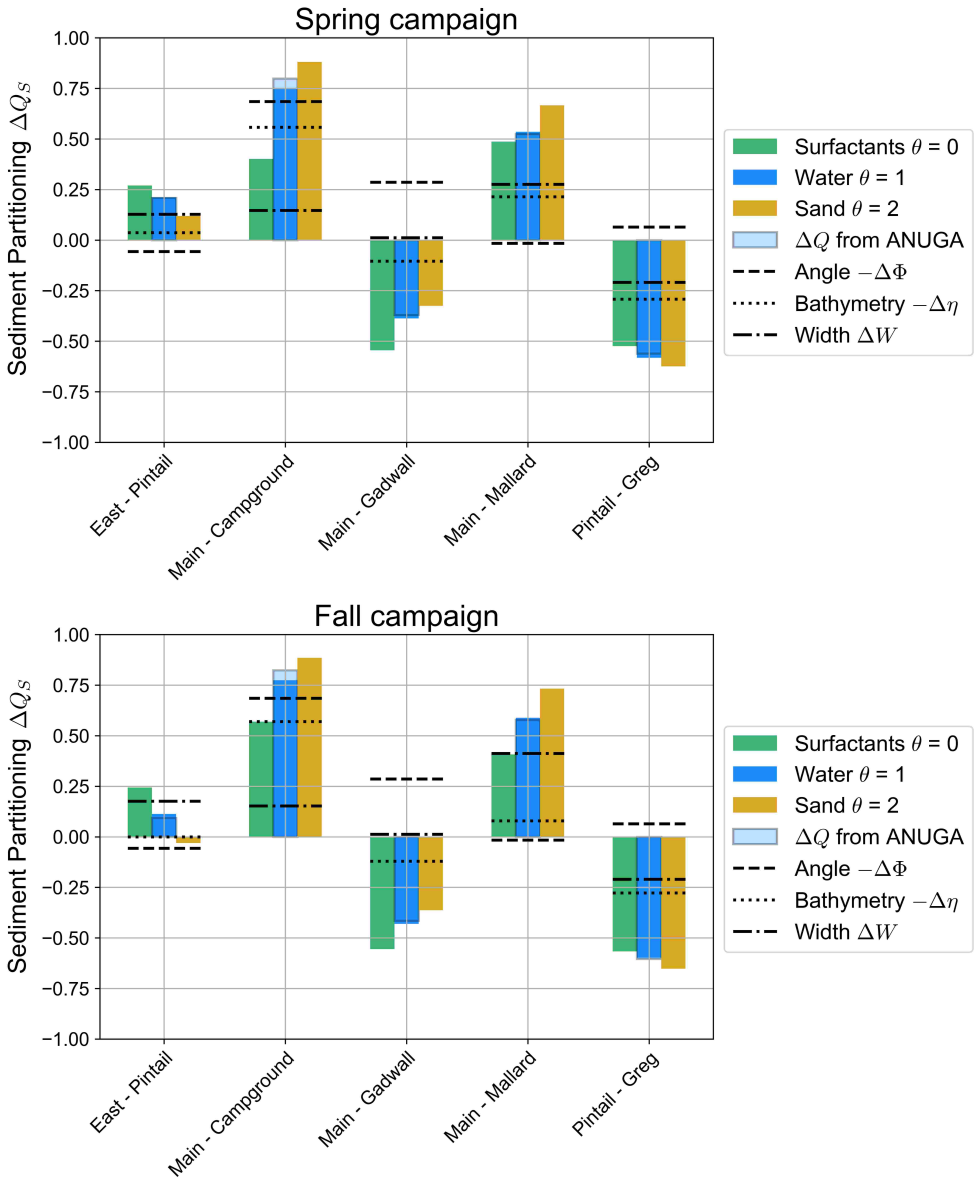


Figure 18.1: Sediment partitioning ΔQ_S at the five bifurcations of the Wax Lake Delta for two different flow conditions, retrieved from the `dorado` simulations we performed with different values of θ. Black lines indicate the potential controls on sediment partitioning, namely the angle asymmetry $\Delta\Phi$ (dashed line), the bathymetric step $\Delta\eta$ (dotted line), and the channel width asymmetry ΔW (dash-dotted line). Note that the bins referring to the flow partitioning ΔQ retrieved from the ANUGA simulations overlap those of `dorado` simulations performed with $\theta = 1$ for all bifurcations except Main-Campground.

sediment partitioning ΔQ_S for different values of θ, according to which a proportionately larger fraction of sand is directed towards the dominant branch for each of the three bifurcations (i.e., $|\Delta Q_S(\theta = 2)| > |\Delta Q_S(\theta = 1)|$).

On the contrary, for both the East-Pintail and Main-Gadwall bifurcations ΔQ_S decreases as θ increases. Contrary to the bifurcations described above, for these bifurcations the dependence of ΔQ_S on θ is not consistent with the bathymetric step between the downstream channels, since a proportionately lower fraction of sand is routed towards the deeper channel. Interestingly, the dependence of ΔQ_S on θ of the five bifurcations can be explained by observing the bathymetry of the upstream channel. In fact, by looking at the bathymetry maps (Figure 17.2, Figure 21.2), one can readily see that the East-Pintail and Main-Gadwall bifurcations are the only ones showing a transverse gradient in the bathymetry of the upstream channel such that the deeper area is located in front of the branch carrying the lower fraction of particles. On the other hand, bifurcations where $|\Delta Q_S(\theta = 2)| > |\Delta Q_S(\theta = 1)|$ show a transverse bed slope such that the deeper area corresponds to the branch carrying the larger fraction of particles. Thus, we argue that larger values of θ lead a fraction of the incoming particles to be routed towards the deeper area of the upstream channel, whose bathymetry transverse gradients affect the particle partitioning despite any possible bathymetric steps between the downstream channels.

Notably, the incoming flow discharge does not seem to affect considerably the partitioning of water and sediments. In fact, the water asymmetry ΔQ and particle partitioning ΔQ_S computed for the high-flow and low-flow conditions (corresponding to the Spring campaign and Fall campaign, respectively) are almost identical (Figure 18.1). The only difference between the two campaigns concerns the partitioning of surfactants (i.e., `dorado` simulations with $\theta = 0$) at the Main-Campground bifurcation, which is more balanced in high-flow conditions, possibly due to localized overbank flow at the bifurcation node.

18.1.2 Comparison with remote sensing estimates

Overall, the sediment partitioning tendency is similar between the `dorado` simulations and the flux map (Figure 18.2). The `dorado` simulations with $\theta = 1$ (representing water) yield results more closely aligned with the flux map than those with $\theta = 2$ (representing sand). This result is likely due to the fact that most of the sediment supplied to the Wax Lake Delta is primarily very fine (silt-clay), thus behaving more passively in the flow (Nghiem et al., 2025).

When comparing the results of the two campaigns, the estimates of the sediment partitioning ΔQ_S shows good agreement for the Spring campaign (Figure 18.2). In contrast, for the Fall campaign, the `dorado` simulations overestimate sediment asymmetries compared to the remote sensing estimates, particularly at the East-Pintail and Main-Campground bifurcations. We attribute this difference to the strong cohesiveness of the sediment supplied to the Wax Lake Delta (Shaw et al., 2013).

In Spring, the higher flow rate (5148.3 m^3/s at the apex) results in advection-dominated transport, while in Fall, the cohesive properties of the sediment influence more sediment transport due to the lower flow rate (1646.3 m^3/s at the apex). The clay fraction was also higher in the Fall campaign than in the Spring campaign (Nghiem et al., 2023). Cohesive properties lead to the aggregation of flocs, resulting in high uncertainty in the shear stress and settling velocity (Cortese et al., 2024). This result is consistent with the flux map showing larger variation during the Fall campaign. Additionally, this cohesive mechanism is strongly influenced by vegetation (Lauzon & Murray, 2018), which is more dominant during the Fall campaign, potentially leading to a difference between simulations and flux maps.

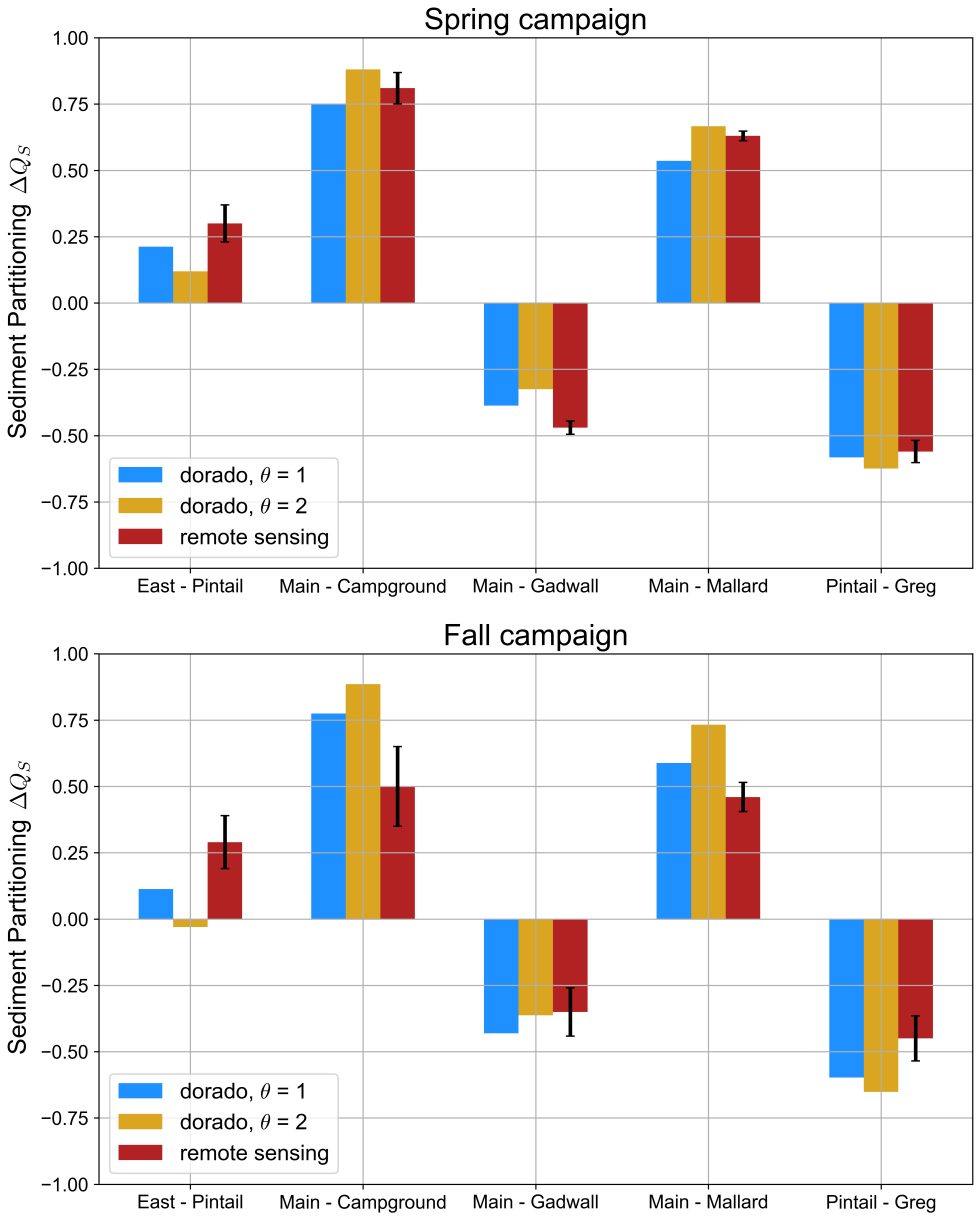


Figure 18.2: Comparison between the sediment partitioning ΔQ_S at the five bifurcations of the Wax Lake Delta retrieved from `dorado` simulations with θ=1 (passively transported sediments) and θ=2 (sand) and the sediment partitioning retrieved from remote sensing imagery and computed by means of Equation (17.6). The error bars show the uncertainty calculated using Equation (17.7).

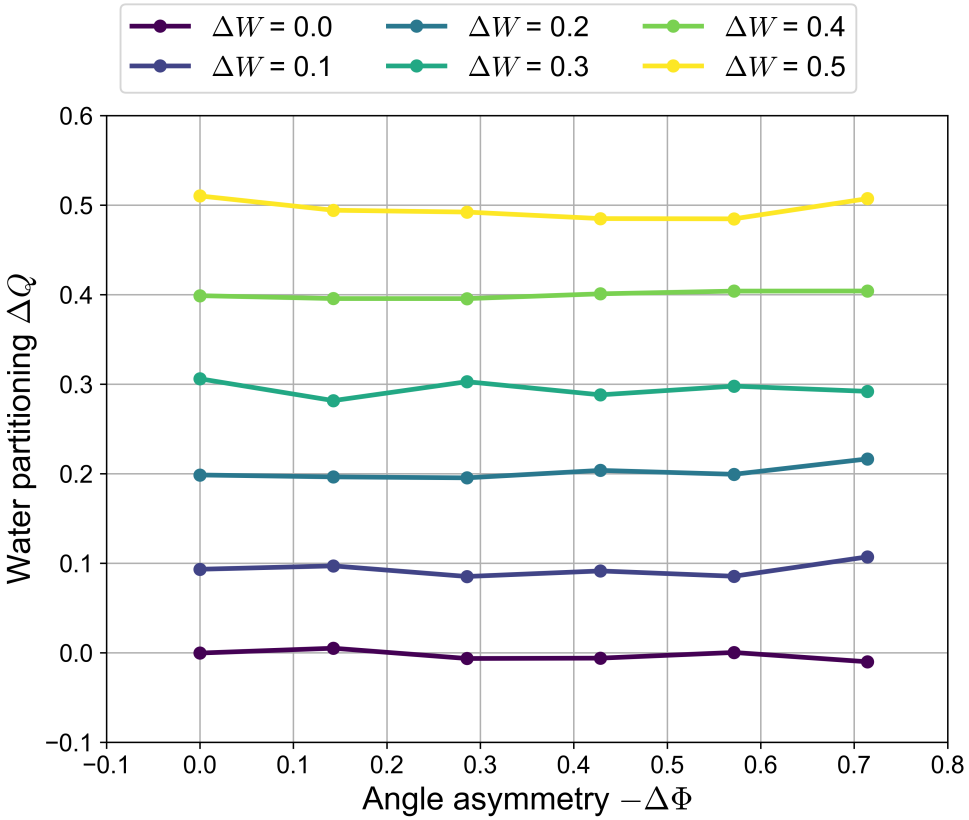


Figure 18.3: Flow discharge partitioning ΔQ given by the ANUGA simulations performed on the simplified geometry for different values of width asymmetry ΔW and angle asymmetry $\Delta\Phi$.

18.2 SIMPLIFIED GEOMETRY

The simplified geometry allows us to broadly explore the dependence of the water and sediment partitioning on the bifurcation geometry. In the following, we will present the results of the simulations we performed on the different configurations of the simplified geometry outlined in section 17.6. Specifically, we will discuss the dependence of the flow discharge asymmetry ΔQ and of the particle partitioning ΔQ_S on three asymmetry indicators, namely the branching angle asymmetry $\Delta\Phi$, the width asymmetry ΔW, and the bathymetric step $\Delta\eta$.

Firstly, we analyse the dependence of the water partitioning ΔQ on the angle asymmetry $\Delta\Phi$, considering the configurations without a bathymetric step (i.e., with $\Delta\eta = 0$) and with different values of the width asymmetry ΔW. Notably, simulation results clearly suggest that the angle asymmetry does not affect water partitioning (Figure 18.3). Furthermore, the results show that water is partitioned proportionally to the channel width (i.e., $\Delta Q = \Delta W$) when there is no bathymetric step, in agreement with the widely employed width-based estimator of the flow discharge (Hariharan et al., 2022).

For a given value of the width asymmetry ΔW, larger bathymetric steps $\Delta\eta$ further increase the flow discharge asymmetry ΔQ (Figure 18.4). Moreover, simulations done on bifurcations with the same values of ΔW and $\Delta\eta$ but different angle asymmetries $\Delta\Phi$ show negligible differences in ΔQ, highlighting that the angle asymmetry does not affect the water partitioning even in the presence of a bathymetric step. These results confirm our observations on the water partitioning at the bifurcations in the Wax Lake Delta, whose flow discharge asymmetry ΔQ shows a clear dependence on the width asymmetry ΔW and the bathymetric step $\Delta\eta$, and a negligible role of the angle asymmetry $\Delta\Phi$ (Figure 18.1).

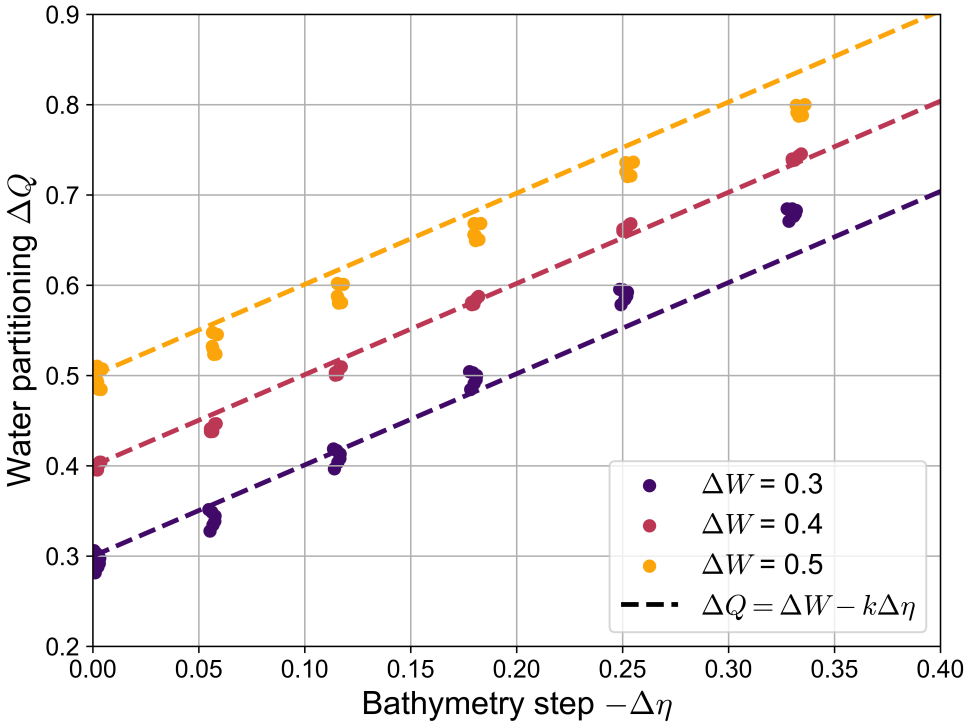


Figure 18.4: Flow discharge partitioning ΔQ given by the ANUGA simulations performed on the simplified geometry for different values of width asymmetry Δ*W* and bathymetric step Δη. Dashed lines indicate the values of ΔQ returned by the simplified relationship reported in Equation (18.1), using k = 1.01. The groups of points sharing the same values of Δ*W* and similar values of Δη refer to simulations performed with different values of angle asymmetry ΔΦ.

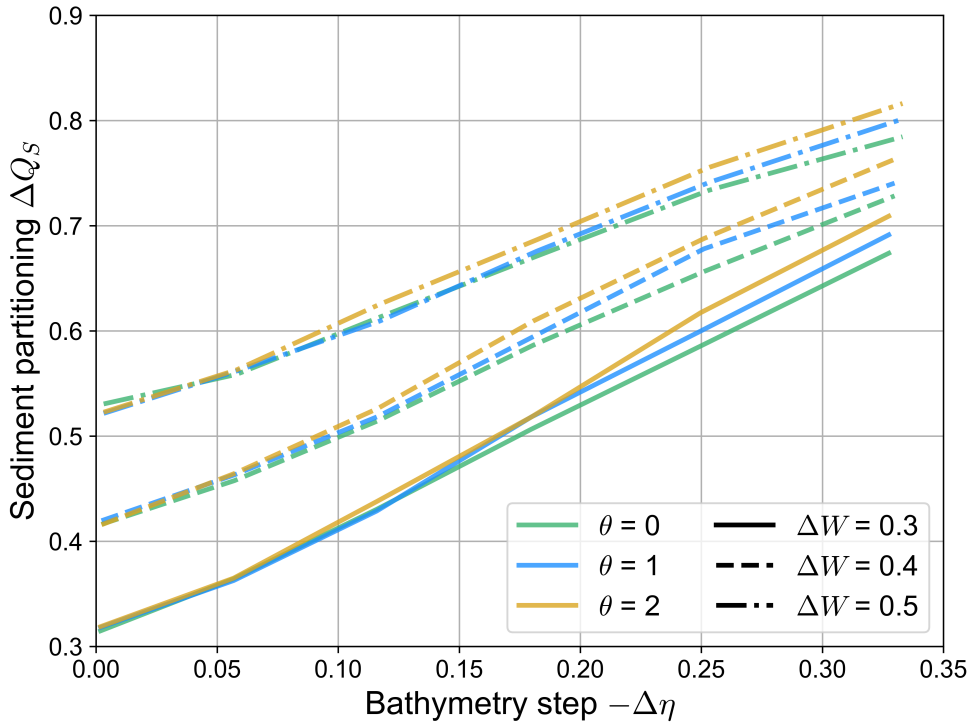


Figure 18.5: Sediment partitioning ΔQ_S retrieved from the `dorado` simulations on the simplified geometry, using different values of the bathymetric step $\Delta\eta$ in the downstream channels and of the parameter θ. The particle partitioning ΔQ_S for each combination of $\Delta\eta$, ΔW and θ is computed as the average between the partitioning returned by simulations having different values of $\Delta\Phi$.

According to simulation results on the simplified geometry, the influence of $\Delta\eta$ and ΔW on the water discharge partitioning ΔQ can be expressed by means of a simple relationship of the form

$$\Delta Q = \Delta W - k\Delta\eta, \tag{18.1}$$

where the best-fit value of the parameter k for our numerical simulations is $k = 1.01$ (Figure 18.4). It is worth noting that the linear dependence of ΔQ on the bathymetric step $\Delta\eta$ shown by Equation (18.1) is consistent with the experimental findings of Bertoldi and Tubino (2007) and the numerical simulations by Miori et al. (2012), both referred to gravel-bed bifurcations. The flow discharge asymmetry ΔQ resulting from Equation (18.1) matches almost exactly that resulting from the numerical simulations for lower values of the bathymetric step $\Delta\eta$. However, numerical results suggest that the best-fit value of k decreases as ΔW increases. In other words, given the same range of the bathymetric step, simulations with lower values of ΔW show a faster dependence of ΔQ on $\Delta\eta$.

Analogously to the analyses performed on the Wax Lake Delta bifurcations, the particle partitioning for `dorado` simulations having $\theta = 1$ matches the flow discharge partitioning ΔQ retrieved from the ANUGA hydrodynamic simulations. Thus, according to our results the branching angle does not affect the partitioning of passively transported sediments, being the relationship between the sediment partitioning ΔQ_S and the angle asymmetry $\Delta\Phi$ analogous to that shown in Figure 18.3. To evaluate the partitioning of sediments and other components, we evaluated the changes in the particle partitioning ΔQ_S for each idealized bifurcation resulting from varying `dorado`'s parameter θ. Simulation results reveal that the sediment discharge asymmetry ΔQ_S is weakly dependent on θ, regardless of the differences in branching angle and bathymetric step between the downstream channels (Figure 18.5). For larger values of the bathymetric step, ΔQ_S slightly increases as θ increases, due to

the larger influence of the local water depth on the preferential routing direction. As will be discussed in the following section, we believe that this result is a consequence of the chosen bathymetry of the simplified geometry, which does not include any transverse bed slope in the upstream channel (Figure 17.4).

19 DISCUSSION AND CONCLUSIONS

The combined use of the 2D hydrodynamic model ANUGA and the Lagrangian particle-tracking module `dorado` allowed us to estimate the division of water and sediments at five bifurcations in the Wax Lake Delta (WLD), and to investigate the role of different geometrical properties of bifurcations. Our analyses on the WLD show that bifurcations with large width asymmetries and bathymetric steps display a larger asymmetry in the flow distribution between the bifurcates, while differences in the branching angles do not seem to affect the flow partitioning. The sediment partitioning at the different bifurcations returned by the `dorado` simulations satisfactorily reproduces the partitioning of Suspended Sediment Load estimated using field data and remotely sensed images, although showing some discrepancies at low-flow conditions (see subsection 18.1.2). The results of the analyses on the WLD were confirmed and extended by the simulations performed with the same modelling tools on a synthetic geometry of a deltaic bifurcation, which allowed us to quantify the sensitivity of water and sediment partitioning to differences in branching angles, channel widths and inlet bed elevations between the downstream channels. Simulation results confirm the well-known influence of the widths of the bifurcates on the partitioning of water and suspended sediments at bifurcations, showing that water splits proportionately to the channel widths when there are no discontinuities in the bathymetry of the three channels, whatever the difference between the branching angles of the bifurcates. Consistently with previous modelling studies on bifurcations, our results suggest that a step in the bathymetry between the inlets of the downstream channels can lead to a much more unbalanced partitioning of water and sediments, given the same widths of the bifurcates. Moreover, the simulations performed on the simplified geometry allow for quantifying the sensitivity of the flow discharge division on the height of the bathymetric step, for different values of the channel width asymmetry of the bifurcates.

The flow discharge asymmetry ΔQ resulting from the simulations performed on the synthetic geometry turned out to be reliably estimated by means of a simple linear combination of the differences in channel widths and average bed elevations of the branches. The resulting relation, described by Equation (18.1), shows that ΔQ linearly depends on the difference between the bed elevations according to a coefficient k, which is an order-1 parameter. As suggested by the numerical results, the best-fit value of k decreases with the width asymmetry ΔW. This dependence can be explained by adopting physics-based arguments: in fact, by employing uniform-flow rating curves at the inlet of the branches, a linear analysis of the equations provides the relation:

$$k \sim (1 - \Delta W^2). \tag{19.1}$$

The full derivation of Equation (19.1) is reported in chapter 20.

The simple formula reported in Equation (18.1) combines the well-established width-based partitioning (according to which $\Delta Q = \Delta W$) with previous evidence of the (linear) influence of bathymetric steps on flow discharge partitioning (Bertoldi & Tubino, 2007; Miori et al., 2012). To assess its accuracy, we used Equation (18.1) to estimate the flow partitioning at the bifurcations of the Wax Lake Delta, using the values of ΔW and $\Delta\eta$ derived from field data and comparing the resulting values of ΔQ against those retrieved from the calibrated numerical simulations performed by Wright, Passalacqua, et al. (2022). The simplified formula shows good agreement with the numerical simulations (Figure 19.1), considerably improving the estimate obtained via the width-based method. Specifically, the width-based predictor underestimates the flow discharge asymmetries resulting from the simulations, let aside

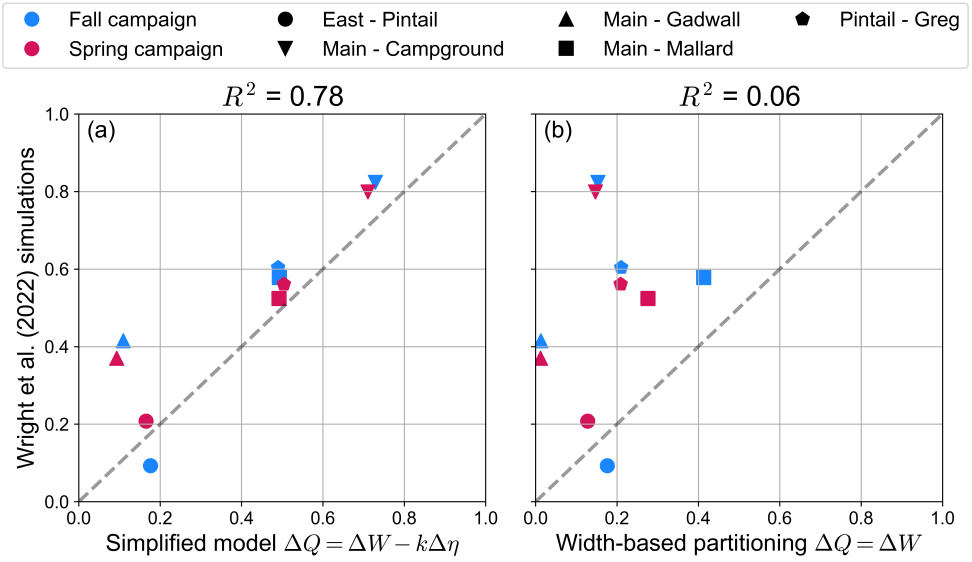


Figure 19.1: Comparison between the water discharge asymmetry ΔQ of the bifurcations in the Wax Lake Delta retrieved from Wright, Passalacqua, et al. (2022) and those computed using (a) the simplified formula $\Delta Q = \Delta W - k\Delta\eta$ we propose (using $k = 1.01$) and (b) the width-based estimator, i.e., $\Delta Q = \Delta W$.

the East-Pintail bifurcation, where there is no inlet step between the bifurcates. We note that the low accuracy of this predictor is likely affected by our point estimate of the inlet channel width, and may be improved by employing a reach-averaged estimation of the channel width, as done by previous studies (Dong et al., 2020; Hariharan et al., 2022). Furthermore, in our study we do not consider bifurcations with a large width asymmetry ($\Delta W > 0.5$), which are often observed in deltas and have been included in previous analyses to validate the width-based partitioning predictor. As suggested by the numerical results, the effect of the inlet step $\Delta\eta$ decreases as the width asymmetry ΔW increases (Figure 18.4), suggesting that width-based partitioning can be more accurate in bifurcations with larger values of ΔW. It is worth highlighting that width-based partitioning has proven to be a reliable tool when only remotely sensed images are available, as shown by the in-depth analysis carried out by Hariharan et al. (2022). However, our results suggest that even a first approximation of bathymetric differences between the downstream channels can greatly improve the flow partitioning estimate.

Several authors employed the liquid area asymmetry ΔA (defined following Equation 17.3) to evaluate the flow discharge asymmetry at deltaic bifurcations, finding a good agreement with field data (Dong et al., 2020). However, the relationship $\Delta Q = \Delta A$ can be mathematically justified only if the flow velocity (averaged over the cross-section) is the same for both bifurcates. Due to the (nonlinear) dependence of the flow velocity on the water depth, non-negligible differences in flow velocities can be expected whenever a bathymetric step is present. For this reason, we argue that the uniform-flow rating curves provide a more accurate, physics-based estimate of the flow partitioning. Nonetheless, using the liquid area asymmetry leads to a dependence of ΔQ on the bathymetric step $\Delta\eta$ that resembles Equation (18.1), with a relation between the coefficient k and ΔW that follows Equation (19.1).

The analyses performed on the Wax Lake Delta and the simplified geometry show that the partitioning of water in deltaic bifurcations is not affected by different branching angles between the bifurcates. This result suggests that upstream effects on the flow field induced by the branching angle of side channels play a minor role (if any) in determining how water splits between the downstream channels. However, our hydrodynamic simulations were based on the shallow-water equations, thus they neglected any possible three-dimensional flow structures as those resulting from

helical flow. These flow structures, which have also been observed in a bifurcation of the Wax Lake Delta (not analysed in the present study) by Chowdhury et al. (2023), may affect the flow division and the stability of natural bifurcations (Thomas et al., 2011), although their formation can be inhibited by the presence of bedforms (Parsons et al., 2007). Overall, the influence of helical flow and coherent structures on the flow partitioning has yet to be explored for deltaic bifurcations and will deserve further investigations.

Concerning the partitioning of sediments, we firstly note that the `dorado` simulations performed on the synthetic geometry reveal that the particle partitioning equals that of water returned by ANUGA simulations for any value of θ (Figure 18.5), i.e., regardless of the dependence of the particle routing direction on the local water depth. The simplified geometry intentionally lacked any transverse gradient in the bathymetry of the upstream channel, to isolate the role of the geometry of the downstream channels; thus, this result implies that transverse gradients in the free surface of the upstream channel, if any, are so small that they are not able to affect the particle routing. In fact, different values of θ should lead to different particle partitioning in the presence of transverse gradients in the water depth. According to our simplified relationship for the flow partitioning, transverse gradients in the free surface do not affect the partitioning of water either; thus, our study suggests that assuming a flat water surface at the bifurcation node is a reasonable assumption when analysing the flux partitioning at deltaic bifurcations, in agreement with the modelling studies that made the same hypothesis for lowland (Slingerland & Smith, 1998) and gravel-bed (Bolla Pittaluga et al., 2003) bifurcations.

The combined analysis of the `dorado` simulations performed on the simplified geometry and on the Wax Lake Delta allows us to shed light on the role played in the partitioning of sediments with different Rouse numbers by a transverse gradient in the bathymetry of the upstream channel, which emerges as a novel controlling factor. As a matter of fact, simulations performed on the synthetic geometry, where there is no such gradient, are not able to reproduce the dependence of the particle partitioning ΔQ_S on θ observed for the bifurcations in the Wax Lake Delta. Specifically, the difference between the sediment partitioning ΔQ_S of sand ($\theta = 2$) and washload ($\theta = 1$) in the WLD bifurcations is of the order of 10^{-1} (Figure 18.1), while the values of ΔQ_S computed for the simplified geometry are an order of magnitude lower (Figure 18.5). We believe that this different dependence of the sediment partitioning on θ, i.e., on the Rouse number, can be associated with transverse gradients in the bathymetry of the upstream channel. As pointed out in subsection 18.1.1, the `dorado` simulations performed for the WLD with $\theta = 2$ show either a larger or lower asymmetry compared to the flow discharge asymmetry returned by the ANUGA hydrodynamic simulations, which is correctly captured by `dorado` simulations with $\theta = 1$. Interestingly, in all bifurcations where the partitioning of sand ($\theta = 2$) is more balanced than that of washload ($\theta = 1$), the bathymetry of the upstream channel shows a transverse gradient with a deeper area in front of the branch carrying the lower fraction of particles. On the contrary, in bifurcations where the deeper area is in front of the dominant branch the partitioning of sand is more unbalanced than that of water. These results suggest that transverse gradients in the upstream channel bathymetry can cause a proportionately larger amount of sand to be routed towards the corresponding bifurcate. We note that this preferential routing may happen for all sediments that are not transported passively, i.e., whose Rouse number is not vanishing, and can gradually become more intense as the Rouse number increases. The `dorado` simulations on the synthetic geometry strengthened this result, showing that ΔQ_S is not affected by changes in θ in absence of a transverse bathymetry gradient in the upstream channel. Specifically, these results suggest that this gradient is the main controlling factor of the dependence of ΔQ_S on θ, i.e., of the partitioning of sediments with different Rouse numbers.

We note that Slingerland and Smith (1998) already pointed out that the larger the Rouse number in the upstream channel, the lower the fraction of sediments entering

side channels with a bathymetric step at their inlet, due to the larger concentration in the deeper portion of the water column in the main channel. However, according to their model formulation, the division of sediments should be affected by θ in our simplified geometry (which resembles the geometry they considered), contrary to our results. Thus, our analyses suggest that the bathymetric step that controls the partitioning of sediments is that located in the upstream channel, rather than the inlet step at the entrance of the side channel. Thus, if the bed elevation of the upstream channel is lower on the same side of the channel carrying the lower fraction of sediments, the partitioning of sediments with non-vanishing Rouse numbers will be more balanced than water due to a proportionately larger fraction of sediments entering this channel (as in the case of the Main-Gadwall bifurcation, Figures 17.2 and 18.1).

It is worth noting that the role of a transverse bed slope in the upstream channel on the partitioning of sediment was proposed for gravel-bed bifurcations by Bolla Pittaluga et al. (2003), who included it in their widely employed nodal-point relation for the estimate of the bedload partitioning. Moreover, our results are in agreement with field observations by Sassi et al. (2013), who found that the partitioning of suspended sediments at deltaic bifurcations mainly depends on the transverse concentration profile in the upstream channel. Overall, our analyses suggest that the division of sediments at deltaic bifurcations is strongly affected by their transverse concentration profile in the upstream channel. Consequently, we believe that any factor that may affect it, including a transverse gradient in the bathymetry, should be taken into account in future modelling studies on bifurcations where most sediments are transported in suspension.

Generally speaking, the transport of suspended sediments, and therefore its division at bifurcations, is affected by turbulence and displays three-dimensional features. The formulation of the `dorado` model does not account explicitly for these effects, although it does include a proxy representation of the vertical concentration profiles of the transported material. In spite of its simplified approach, however, the `dorado` simulations we performed on the WLD showed a good agreement with field measurements of suspended load, albeit showing larger differences in low-flow conditions. To further corroborate the insights provided by this work, our results could be compared with those of more complex numerical models, to understand whether other local processes play a first-order control on the division of suspended sediments.

Lastly, we note that the flux partitioning and the dynamics of natural bifurcations are the result of the combination of local controls with other hydraulic and morphological processes (i.e., external forcings), which can affect the flow conditions of both the upstream and downstream channels. Concerning bifurcations in deltas, these forcings include asymmetries in the free-surface slope induced by differences in branch length (Edmonds, 2012), tides (Ragno et al., 2020), waves (Ashton et al., 2013), delta lobe progradation (Salter et al., 2018) and curvature in the upstream channel (Kleinhans et al., 2008; Sassi et al., 2013). Understanding how local drivers influence the partitioning of water and sediments is therefore only the first step towards a more comprehensive modelling framework for deltaic bifurcations. Therefore, further studies could investigate how the influence of external forcings on the partitioning of water and sediments interacts with that of the local drivers investigated by the present study.

CONCLUSIONS

Based on previously calibrated hydrodynamic simulations on the Wax Lake Delta, we employed the Lagrangian particle-tracking model `dorado` to understand how particles with different buoyancy split at five different bifurcations, finding good agreement with the sediment fluxes retrieved from field measurements. We then

employed the same numerical tools on a synthetic geometry, to investigate the dependence of the water and sediment partitioning on the geometrical features of the bifurcates, namely channel width, branching angle and inlet bed elevation. Our analyses allow us to draw the following conclusions regarding the controlling factors on water and sediment partitioning at deltaic bifurcations:

- Differences in branching angles among the bifurcates do not affect the partitioning of water and sediments, suggesting a limited influence of bi-dimensional effects on the flow field caused by different branching angles of side channels.
- As verified by previous studies, water splits proportionately to the channel width when differences in the bed elevation among the bifurcates are negligible. However, bathymetric steps at the inlet of side channels considerably increase the flow discharge asymmetry. This effect has been extensively analysed for gravel-bed bifurcations, starting from the work by Bolla Pittaluga et al. (2003). Our contribution suggests that these steps play an important role also within deltaic networks, and provides a quantification of their effect by means of a simple linear relationship that relies on dimensionless indicators.
- Transverse slopes in the upstream channel exert a major control on how sediments with non-vanishing Rouse numbers split with respect to washload, leading the former to be preferentially routed towards the bifurcate corresponding to the deeper areas of the upstream channel.

20 APPENDIX: SIMPLE FORMULA FOR THE FLOW PARTITIONING

We first note that, using the asymmetry indicators defined in the main paper, the channel width and water depth of the two downstream channels can be written as:

$$D_L = \overline{D}(1+\Delta D), \quad D_R = \overline{D}(1-\Delta D), \tag{20.1a}$$

$$W_L = \overline{W}(1+\Delta W), \quad W_R = \overline{W}(1-\Delta W), \tag{20.1b}$$

where the average depth and width of the downstream channels are defined as:

$$\overline{D} = \frac{D_L + D_R}{2} \tag{20.2a}$$

$$\overline{W} = \frac{W_L + W_R}{2}, \tag{20.2b}$$

and the subscript U indicates the upstream channel, while ΔD and ΔW are defined as in Equation (3) of the main paper. Then, we define the dimensionless variables

$$\left(D_i^*, \overline{D}^*\right) := \frac{(D_i, \overline{D})}{D_U}, \quad \left(W_i^*, \overline{W}^*\right) := \frac{(W_i, \overline{W})}{W_U}, \quad Q_i^* := \frac{Q_i}{Q_U}, \quad i = L, R. \tag{20.3}$$

Using the Manning-Strickler formula for the flow resistance and assuming that the branches share the same Manning coefficient n and bed slope S, the uniform-flow rating curves in the three branches read as:

$$Q_i = \frac{1}{n} W_i \sqrt{S} D_i^{5/3}, \quad i = U, L, R, \tag{20.4}$$

and can be made dimensionless using the scaling (20.3), yielding

$$Q_i^* = W_i^* D_i^{*5/3}, \quad i = L, R. \tag{20.5}$$

In dimensionless terms, the continuity equation at the node reads

$$Q_L^* + Q_R^* = 1, \tag{20.6}$$

which, using Equations (20.1, 20.3, 20.5), can be written as:

$$\overline{W}^* \overline{D}^{*5/3} \left[(1+\Delta W)(1+\Delta D)^{5/3} + (1-\Delta W)(1-\Delta D)^{5/3} \right] - 1 = 0. \tag{20.7}$$

To obtain a simplified relationship between ΔQ, ΔW and ΔD, we linearize Equation (20.7) considering a reference state, denoted with the subscript 0, where the water depth asymmetry ΔD equals 0. We then consider a small perturbation of the water depths of the bifurcates, such that ΔD can be considered a small parameter and $\overline{D}^*$ can be expanded as:

$$\overline{D}^* = \overline{D}_0^* + \overline{D}_1^*, \quad \overline{D}_1^* \ll \overline{D}_0^*. \tag{20.8}$$

Using a first-order Taylor expansion, the nonlinear terms in Equation (20.7) can therefore be written as:

$$\overline{D}^{*5/3} \cong \overline{D}_0^{*5/3} + \frac{5}{3} \overline{D}_0^{*2/3} \overline{D}_1^* \tag{20.9a}$$

$$(1+\Delta D)^{5/3} \cong 1 + \frac{5}{3} \Delta D. \tag{20.9b}$$

At the leading order, Equation (20.7) gives:

$$\overline{D}_0^* = \left(2\overline{W}^*\right)^{-3/5}. \tag{20.10}$$

Using Equation (20.10) and considering linear terms, Equation (20.7) gives:

$$\overline{D}_1^* = -\Delta W \Delta D. \tag{20.11}$$

Using the scaling (20.3), the flow discharge asymmetry ΔQ can be written as:

$$\Delta Q = Q_L^* - Q_R^* = \overline{W}^* \overline{D}^{*5/3} \left[(1+\Delta W)(1+\Delta D)^{5/3} - (1-\Delta W)(1-\Delta D)^{5/3} \right], \tag{20.12}$$

which, using Equations (20.10) and (20.11) and neglecting higher-order terms, takes the following form:

$$\Delta Q = \Delta W + \frac{5}{3} \Delta D (1 - \Delta W^2). \tag{20.13}$$

Being $\Delta D = -\Delta \eta$ (Equation 17.5 of the main paper), Equation (20.13) is equivalent to considering

$$k = \frac{5}{3}(1 - \Delta W^2) \tag{20.14}$$

in Equation (18.1) of the main paper.

21 SUPPORTING INFORMATION

21.1 SEDIMENT FLUX MAP OF THE WAX LAKE DELTA

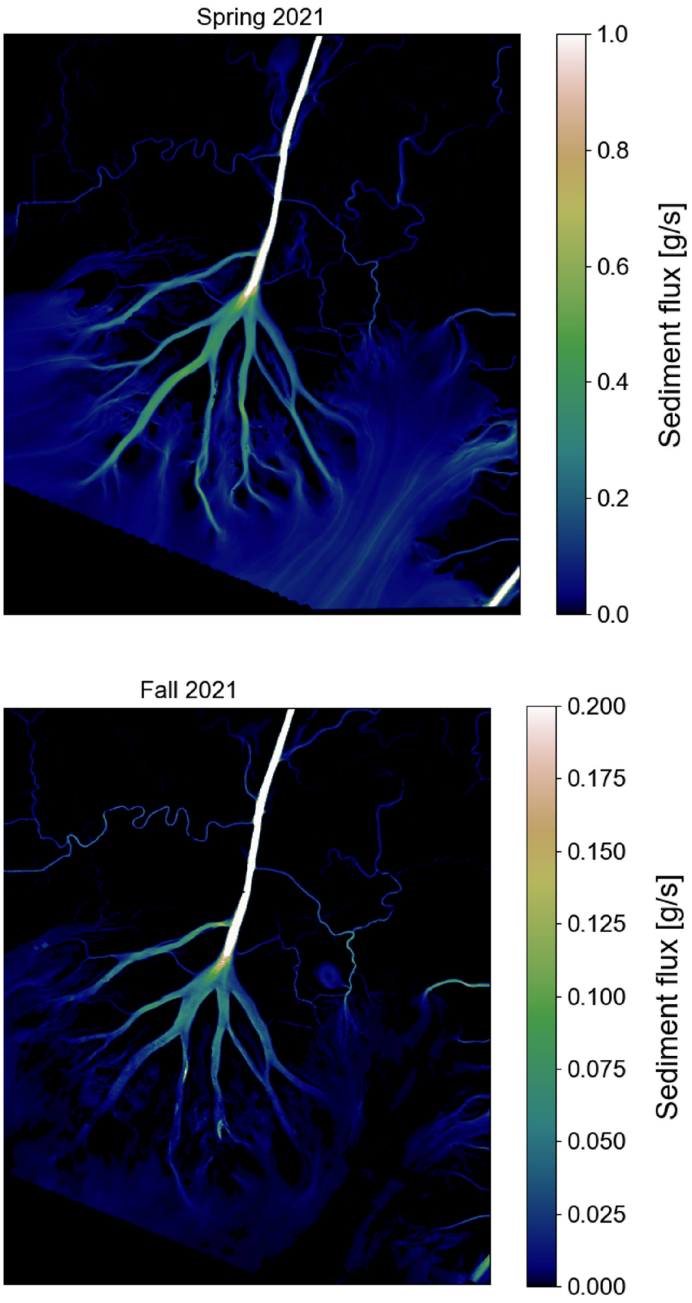


Figure 21.1: Flux maps for the Wax Lake Delta for the Spring and Fall campaigns of NASA's DeltaX program.

21.2 CROSS-SECTION PROFILES OF THE BIFURCATIONS IN THE WAX LAKE DELTA

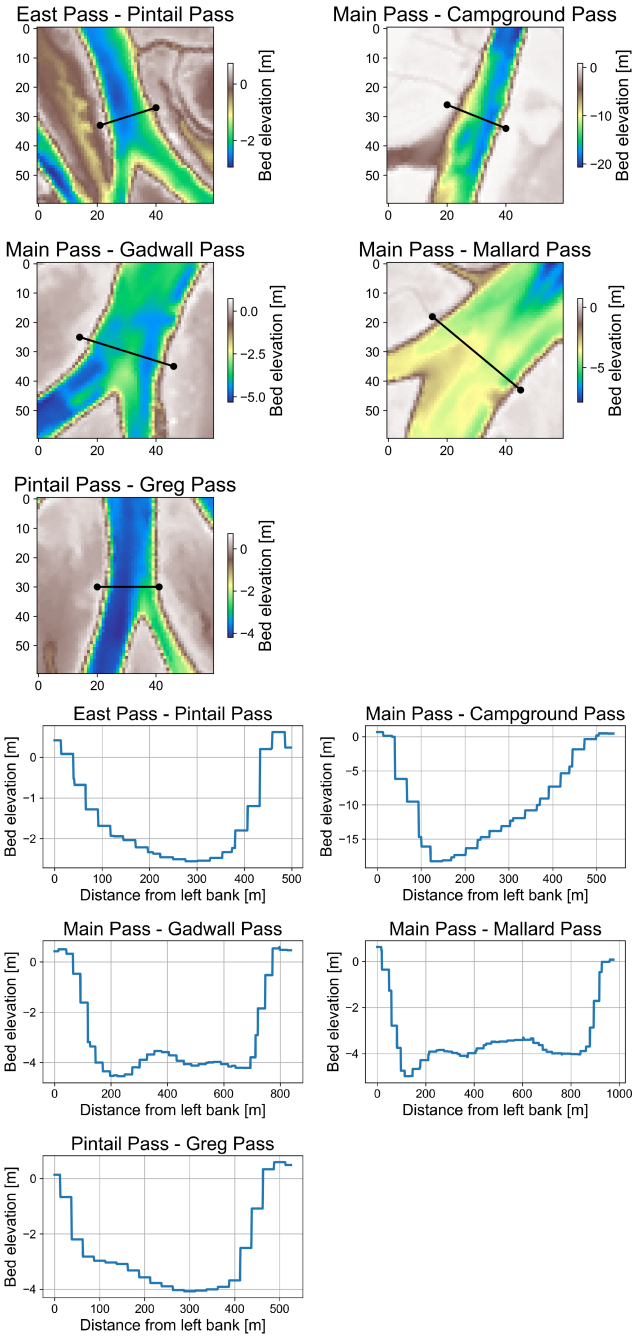


Figure 21.2: Cross-section profiles of the bifurcations in the Wax Lake Delta. The transverse coordinate, used as the horizontal axis in the lower plots, starts from the transect end located on the left bank.

21.3 FURTHER DETAILS ON THE SYNTHETIC GEOMETRY DEFINITION

We chose the length of the channels in the simplified model to be long enough to minimize the boundary effects generated at the downstream end of the bifurcates. After a dedicated sensitivity analysis, we chose a branch length equal to 30% of the backwater length (defined as the ratio between the uniform-flow water depth and the channel slope), which in our case equals $3.13 \cdot 10^5$ m.

Part V

CONCLUDING REMARKS

22 | CONCLUSIONS

THIS WORK'S CONTRIBUTIONS TO THE STUDY OF "FREE" GRAVEL-BED BIFURCATIONS

The numerical and analytical results presented in this work represent a step forward in our understanding of the morphodynamics of river bifurcations. Specifically, the analyses presented in Part ii and Part iii expand the current body of knowledge about gravel-bed, "free" bifurcations, in the wake of the seminal work by Bolla Pittaluga et al. (2003) and of the following studies that relied on the same modelling framework (i.e. the BRT model, see Part i).

The research question addressed in Part ii concerns the conditions in which the flow partitioning into the two downstream branches is so unbalanced that the minor branch is not capable of effectively transporting sediments. This condition represents a limit of the BRT model itself, since its formulation requires that both branches are morphologically active, i.e. they have a non-negligible transport capacity. The first step of the analysis consists of the derivation of the threshold value of the aspect ratio β_{NT} above which these no-transport conditions are met. Then, these conditions are explored using a novel, unsteady numerical model, which shows that when the upstream aspect ratio is larger than β_{NT} all incoming sediments are routed towards the dominant branch, while the flow partitioning is much more unbalanced than that foreseen by the BRT model. This new category of equilibrium configurations is named *partial avulsions*. Contrary to the original BRT framework, in partial avulsion conditions the length of the bifurcates affects the flow and sediment partitioning at equilibrium; in fact, bifurcations with long branches display a higher degree of asymmetry, which leads to channel closure (*full avulsion*) when the branch length exceeds a threshold value. Based on model results, a new analytical framework is formulated to predict the long-term equilibrium state of bifurcations, including partial and full avulsion conditions, which also incorporates the threshold length for channel abandonment.

The analysis carried out in Part iii focusses on the evolutionary timescale of an initially balanced "free" bifurcation that evolves towards an unbalanced equilibrium configuration. The study employs the same numerical tool developed in Part ii and introduces a novel linear analysis that includes the morphological response of the downstream branches. A first key result of this analysis is the identification of two distinct timescales. The first concerns the local morphodynamic evolution at the bifurcation node, which mainly controls the flow and sediment partitioning. The second timescale, which is much longer than the first, is instead related to the overall adjustment of the bed slope of the downstream branches. The investigation then focuses on the first timescale, exploring its dependence on the upstream flow conditions and bifurcation geometry. The distance from resonant conditions, which controls the bifurcation stability (see chapter 2), also stands out as a first-order control on the velocity with which the bifurcation node evolves. The second relevant factor that affects how fast the asymmetry in the flow partitioning develops is the boundary condition set at the downstream end of the branches, which in the proposed formulation is a constant water level, as in most 1-D bifurcation models. This condition accelerates the evolution of the bifurcation, but its influence diminishes with the length of the bifurcates. In fact, the bifurcation timescale grows by an order of magnitude as the branch length increases from 10^2 to 10^4 times the upstream water depth. Both the numerical and the analytical linear model show that when the length of the branches exceeds a given threshold, which can

be derived analytically, the evolution of the bifurcation node no longer depends on the downstream condition and the bifurcation timescale stops increasing with the branch length.

The linear model allows for the quantification of the bifurcation timescale within a wide range of the governing parameters. The resulting values are then compared with the characteristic timescale of several processes that may affect the dynamics of real-world bifurcations. The analysis suggests that bifurcations generally evolve on a longer timescale in comparison with bar migration, except for bifurcations with short branches, or at low values of the reference Shields stress. Moreover, the analysis of a dataset of real gravel-bed bifurcations shows that their timescales range from a few hours to years, thus they are typically longer than those of hydrological flow variations. This study represents the first attempt to perform an extensive analysis on how long it takes for bifurcations to manifest morphological changes as a result of their intrinsic instability. It also provides the starting point for future investigations on the effect of external factors on the evolution of bifurcations in different fluvial contexts.

The analyses presented in Part ii and Part iii rely on several simplifying assumptions, most of which can be found in the BRT model formulation Bolla Pittaluga et al. (2003). Relaxing some of these assumptions might provide new insights on how real-world bifurcations evolve over time. Firstly, the model relies on the concept of formative discharge, thus neglecting the effect of flow variability. Furthermore, the width of the bifurcates is assumed to be fixed and a uniform grain size distribution is considered; in many gravel-bed rivers, these hypotheses might restrain the model capabilities of representing the evolutionary trajectory of bifurcations. Lastly, the simplified representation of the transverse flux of sediments at the bifurcation node has not been tested in unsteady conditions, since most validation efforts have been carried out considering equilibrium conditions (Bertoldi & Tubino, 2007; Ragno & Tubino, 2025; Redolfi et al., 2016). In the following, the main limitations of the work are discussed, and possible future research directions are suggested.

PERSPECTIVES ON THE FREE RESPONSE OF BIFURCATIONS

The discussion included in chapter 14 indicates that single flow events may have a limited morphological impact on gravel-bed bifurcations, especially on those that are close to the resonant conditions and have long branches. In this case, the response of a bifurcation to a variable flow regime could be defined as *incremental*, meaning that it depends on the average properties of the flow regime rather than on the exact sequence of flow events. This hypothesis could be better grounded by means of numerical simulations in which the incoming flow discharge is varied over time to simulate a hydrological regime. The resulting insights could then be used to assess the applicability of the modelling approach suggested by Carlin et al. (2021) to determine the probability of alternating bars occurrence for a given flow discharge time series, which is based on the assumption of an incremental response of bars to the flow regime. Furthermore, the balanced or unbalanced character of bifurcations in the long-term could be better assessed by using the whole hydrological regime rather than considering a reference, "formative" value of the flow discharge, as done in this work.

Among the factors that determine the morphological response of bifurcations, the width of the bifurcates can be intuitively thought of as one of the most influential. Although the formulation by Wang et al. (1995) and the BRT model already considered the widths of the bifurcates to be arbitrary, neither the authors nor any of the following studies extensively analysed the effect of the difference in channel widths on the stability and equilibrium of the system. In fact, most modelling studies on bifurcations —including the present work— consider the simplest configuration, in which the width of both bifurcates is equal to half the width of the upstream channel.

A recent contribution (Barile, Pirlot, et al., 2023) showed that a width asymmetry between the bifurcates enhances the stability of free bifurcations, increasing the critical threshold of the aspect ratio above which balanced configurations become unstable. On the other hand, a local increase in the channel width, which is often observed just upstream of the bifurcation node, exerts an opposite, destabilizing effect, thus increasing the flow and sediment unbalance and promoting the tendency to avulsion. Consistently with this finding, the analysis performed by Pirlot (2024) shows that local widenings rarely exceed 20-30% of the mean river width of the upstream channel in natural *active* bifurcations, while the width asymmetry between the bifurcates shows a wide distribution. A further step in these analyses could be achieved by including local widenings and width asymmetries in the numerical model, exploring their effect on the evolutionary trajectories of real-world bifurcations.

The BRT model assumes that the width of the branches is given and constant over time, as it happens in embanked rivers. However, in natural rivers the channel width evolves over time, possibly tending towards regime values (Ashmore, 2001; Griffiths, 1981; Parker, 1979). In the case of bifurcations, bank evolution processes prefigure a further morphodynamic feedback: changes in flow partitioning at the bifurcation node can lead to changes in the widths in the downstream branches, which in turn affect the flow and sediment partitioning at the node. In Miori et al. (2006a), the long-term equilibrium of bifurcations has been investigated by including in the BRT model the adaptation of the channel width and performing a local analysis at the bifurcation node (thus neglecting the morphological response of the bifurcates). According to this model, gravel-bed bifurcations with erodible banks seem more likely to develop unbalanced configurations. However, this result is mainly due to the application of the regime relationship to the upstream channel: in fact, these formulas return low values of the reference Shields number, causing a decrease in the critical aspect ratio for the bifurcation stability. To explore the transient behaviour of bifurcations with erodible banks, e.g. those embedded in braided networks, future unsteady analyses similar to those performed in this work could let the banks co-evolve with the bifurcation, adopting available dynamic bank evolution models (Cantelli et al., 2004; Cui et al., 2006; Parker, 2004).

As most of the previous bifurcation models, the present work considers a uniform grain size distribution, which is not the case of most gravel-bed rivers, where, in addition, the sand fraction in the bed composition is often non-negligible. As a result, the grain size distribution usually shows a markedly bimodal character and a variety of sorting patterns can be observed on the bed surface (Ashworth et al., 1992). Although the transport of sediment mixtures and the associated sorting effects have been extensively studied, little is known on how sediment mixtures are sorted at bifurcations, where the local changes in the flow conditions and bed topography at the node could affect the way individual grain sizes are transported downstream. The recent contribution of Ragno et al. (2023), which considers a simple bimodal mixture composed of two discrete grain sizes, shows that in unbalanced equilibrium solutions the bed composition is finer in the non-dominant branch, resulting in an increase of its transport capacity. This finding seem to suggest that sediment heterogeneity may reduce the tendency to channel abandonment. Moreover, the analysis provides an indication that bifurcations may enhance the overall fining commonly observed in rivers, consistently with previous evidence on braided networks (Seal & Paola, 1995; Zolezzi et al., 2006). To further analyse the interplay between bifurcations and grain sorting, the analytical framework formulated in chapter 7 could be extended to foresee how the properties of the grain size distribution affect the occurrence of partial and full avulsions, for different flow conditions in the upstream channel and bifurcation geometry. A fully non-linear formulation could also be used to estimate the spatial and temporal scales of the sorting process predicted by the steady analysis by Ragno et al. (2023).

While a lot of theoretical work has been done to study the morphodynamics of "free" bifurcations, there is a paucity of experimental works, let aside a few

fundamental works performed in the early 2000s (Bertoldi & Tubino, 2007; Bolla Pittaluga et al., 2003; Federici & Paola, 2003). In light of recent advances in bifurcation modelling, further analyses relying on laboratory-scaled physical models could offer a new perspective, calling for a reality check of the results obtained by mathematical approaches. For instance, experimental works could help to understand whether the two-cell BRT formulation is still suitable to model the sediment partitioning at the node in the transient behaviour of an evolving bifurcation. Moreover, the effect of different widths and branch lengths could be extensively analysed to validate the results of the aforementioned analytical studies.

PERSPECTIVES ON FORCED BIFURCATIONS

This work mainly focusses on "free" bifurcations and considers symmetric planform geometry and boundary conditions. To narrow the gap with real-world bifurcations, both the analysis on the avulsion conditions and on the evolutionary timescales could be extended by including the effect of external factors, i.e. considering "forced" bifurcations (see chapter 2).

For instance, the role on channel avulsion of planimetric constraints, such as a curved upstream channel, can be straightforwardly incorporated in the analytical model formulated in chapter 7, following the approach of previous studies that analysed the long-term equilibrium configurations (e.g., Redolfi et al., 2019, see chapter 2). A step in this direction has been made in the recent work by Ragno and Tubino (2025), where the analytical model for partial avulsion conditions developed in Part ii has been extended by including the effect of a confluence at the downstream end of the bifurcates and that of a difference in the branch length. The analysis of a large dataset of anabranching units in sand-bed and gravel-bed rivers reveals that most of the observed active bifurcations fall in the region of the parameter space corresponding to unbalanced states with both branches open.

As outlined in chapter 10, the external factors that affect real-world bifurcations are inherently time-dependent and are thus characterized by their own timescales, which may or may not be comparable to that of bifurcations. Modelling efforts to study the impact of these factors on the evolutionary trajectory of bifurcations could thus benefit from an unsteady approach, bringing forward that outlined in Part iii. In fact, the linear formulation presented in chapter 12 allows for an estimate of the bifurcation "intrinsic" timescale, given the flow conditions in the upstream channel and the length of the bifurcates. This estimate can then be compared with the timescale of external forcings, analogously to what is done in chapter 14 for bar migration and flow variations. Such comparisons could suggest whether the bifurcation evolution is mainly governed by either its intrinsic instability or the forcing, or under what conditions there is a competition between the two. For instance, experimental evidence Bertoldi et al. (2009) suggests that either regime is possible when migrating bars interact with bifurcations, depending on upstream flow conditions (see chapter 14).

The linear model developed in Part iii also allows for an explicit inclusion of unsteady forcings, which can be modelled as imposed perturbations at the boundaries of the domain. Therefore, this model could be exploited to explore, for example, the interplay between the variations of the downstream water level, the morphological response of the branches and the flow partitioning set by the bifurcation node. However, a fully-nonlinear numerical approach is required when the aspect ratio is much larger than the resonant threshold, including the partial and full avulsion conditions. A preliminary analysis performed through the numerical model used in this work (Barile et al., 2022) suggests that a steady variation of the downstream water level can promote different long-term regimes, ranging from dynamic equilibrium states to avulsions, possibly reactivating previously abandoned channels in the case of a water level increase.

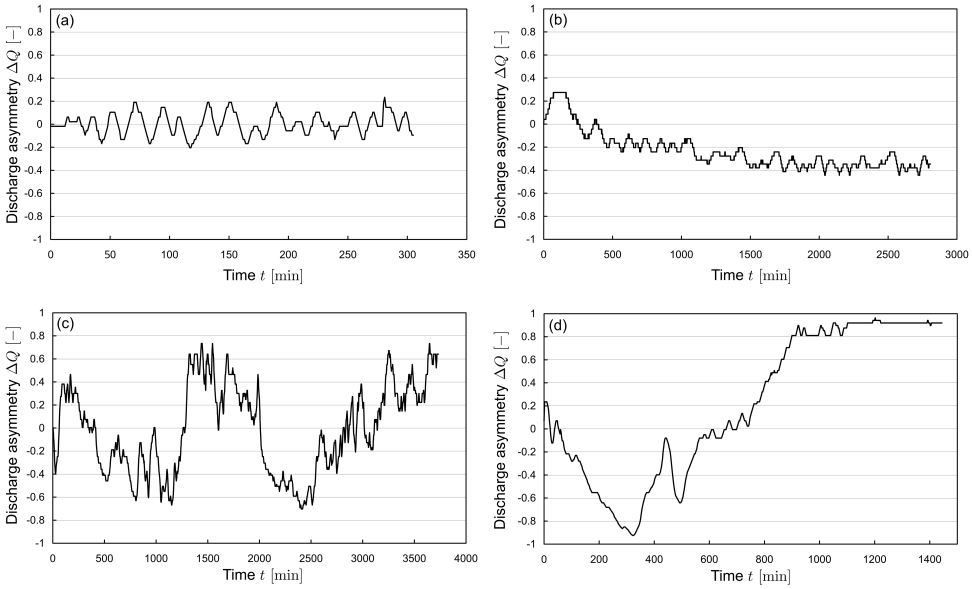


Figure 22.1: Discharge asymmetry ΔQ over time observed by Bertoldi et al. (2009) in their laboratory-scaled physical bifurcation model. The runs illustrate four different types of interaction between migrating bars and bifurcations, showing that bars can induce (a) oscillations in the flow partitioning around a balanced configuration, (b) small perturbations as the bifurcation develops a stable, unbalanced configurations, (c) large perturbations and switches between antisymmetric unbalanced configurations, (d) a single switch between two near-avulsion configurations. Figure adapted from Bertoldi et al. (2009).

In braiding rivers, migrating bars exert a major influence on the stability of bifurcations (Ferguson et al., 1992). Bertoldi et al. (2009) included the effect of migrating bars in the BRT model by imposing that the flow and sediment transport entering the node cells were oscillating in time and unevenly distributed over the cross-section. Their analysis, combined with laboratory observations, provided a broad characterization of the types of interaction between the bar-induced oscillations in the flow and sediment supply and the intrinsic instability mechanism of the bifurcation. However, in several experimental runs the measured discharge asymmetry over time displayed a strongly noisy signal (see Figure 22.1), sometimes exhibiting changes in the dominant branch that could not be entirely predicted by the analytical framework. This evidence might hint at the need to incorporate a stochastic component in morphodynamic models of bifurcations, in order to produce more realistic evolutionary trajectories.

NEXT STEPS FOR SUSPENDED-LOAD BIFURCATIONS

The analysis presented in Part iv represents a step forward the understanding of how water and sediments split at bifurcations in deltas. The two-dimensional hydrodynamic simulations performed on the bathymetry of the Wax Lake Delta and on a synthetic geometry show that the flow discharge asymmetry increases linearly with both the difference between the channel width of the bifurcates and the height of localized bathymetry steps at the inlet of the minor branch, while the water partitioning is not significantly affected by changes in branching angle. Moreover, the results of a Lagrangian model for sediment transport reveal that sediment partitioning follows that of water when the Rouse number of the incoming flux is vanishingly small, while the splitting of sediments is considerably affected by transverse gradients in the upstream bathymetry as the Rouse number gets larger.

Both the analysis on the Wax Lake Delta and the synthetic geometry are based on a number of simplifying assumptions, which might be addressed in future studies on suspended-load dominated bifurcations. Among the different limitations, it is worth remarking that the `dorado` model does not explicitly take into account entrainment and deposition of sediments, thus assuming that the transported sediments are in equilibrium with the bed. Moreover, the partitioning of water and sediments in deltas is the result of the combination of different processes: in addition to the control exerted by the local bifurcation geometry (analysed in the present work), these partitionings can in fact be influenced by tides, waves and other external forcings (see chapter 2 and chapter 19), which might play a relevant role depending on the fluvial context.

Overall, this work sets a starting point for the formulation of a new nodal-point relationship to be employed in one-dimensional models for sand-bed bifurcations. Following the numerical and field evidence, this new nodal-point relationship could rely on a quasi-2D approach that combines the two-cell BRT formulation with the relation for the division of suspended sediments suggested by Slingerland and Smith (1998). The latter accounts for the effect of local steps in the bathymetry, which depends on the Rouse number of the incoming sediment load, and could thus be employed to represent in a simplified fashion the effect of transverse bed gradients highlighted by the simulations performed for the Wax Lake Delta.

It is worth remarking that predicting the partitioning of suspended sediments at bifurcations poses a set of modelling challenges that have not been addressed yet. For example, when flow discharge is partitioned unevenly, the Rouse number of the incoming sediment flux increases abruptly when it is routed towards the minor branch. Thus, sediments transported as washload in the upstream channel could transition into suspended load in the non-dominant branch. Including this process in bifurcation models is key to predict in-channel deposition, thus to explain the widely observed infilling and abandonment of both natural and man-made side channels.

A new modelling framework for the division of water and sediments at sand-bed bifurcations could then be used to quantify their evolutionary timescales, and to seek a comparison with those of external forcings, such as tides and delta front progradation. Regarding the latter process, Barile, Ragno, et al. (2023) recently extended the numerical model developed in Part ii to include a prograding front as downstream boundary condition, building upon the modelling framework earlier developed by Salter et al. (2018) by explicitly considering the delta front height. Model results show that deltaic bifurcations can exhibit different regime behaviours, depending on the length of the branches and the front height, ranging from oscillations in the flow discharge partitioning (with frequent changes in the dominant branch) to channel abandonment. Interestingly, the emergence of different regimes appears to be governed by the ratio between the timescale of delta front progradation (which is mainly controlled by the sediment supply and front height) and the intrinsic bifurcation timescale.

23 CLOSING STATEMENTS

CODE AVAILABILITY

The code used for the 1-D numerical model of a simplified bifurcation, employed in the analysis presented in Part ii and Part iii, is available at https://doi.org/10.5281/zenodo.10079752 (Barile, 2023).

The code for the generation of the synthetic geometry of a bifurcation (employed in Part iv) will be released upon acceptance of the manuscript (Barile, Passalacqua, et al., 2024).

DATA AVAILABILITY

The dataset of the laboratory experiments by Bertoldi and Tubino (2007) is available in the Supplement of their article.

The dataset of the bankfull geometry of the bifurcation-confluence units employed in chapter 14 is available at https://doi.org/10.5281/zenodo.6901398 (Ragno et al., 2022a).

Concerning the analysis on the Wax Lake Delta presented in Part iv:

- the bathymetry and calibrated hydrodynamic simulations on the Wax Lake Delta are publicly available in the DAAC repository at https://doi.org/10.3334/ORNLDAAC/2306 (Wright & Passalacqua, 2024).
- AVIRIS-NG L3-derived concentrations can be downloaded from the ORNL DAAC: https://doi.org/10.3334/ORNLDAAC/2152 (Fichot & Harringmeyer, 2023).
- In-situ measured SSC datasets of the WLD can be downloaded from the ORNL DAAC: https://doi.org/10.3334/ORNLDAAC/2135 (Nghiem et al., 2023).

FUNDING STATEMENT

This work has been supported by the Italian Ministry of Universities and Research (MUR) in the framework of the project DICAM-EXC (Departments of Excellence 2023–2027, grant L232/2016), and the "Agenzia Provinciale per le Risorse Idriche e l'Energia" (APRIE) of the Province of Trento (Italy).

BIBLIOGRAPHY

AIPO. (2022). Rinaturazione dell'area del Po (Programma d'Azione). Retrieved January 8, 2025, from https://www.adbpo.it/download/PNRR_RinaturazionePo/PNRR_Po_PdA_rev_21_07_2022.pdf

Ashmore, P. E. (2001). Braiding phenomena: Statics and kinetics. In M. P. Mosley (Ed.), *Gravel-bed rivers V* (pp. 95–121). N. Z. Hydrol. Soc.

Ashmore, P. E. (1991). How do gravel-bed rivers braid? *Canadian Journal of Earth Sciences*, *28*(3), 326–341. https://doi.org/10.1139/e91-030

Ashton, A. D., Hutton, E. W. H., Kettner, A. J., Xing, F., Kallumadikal, J., Nienhuis, J., & Giosan, L. (2013). Progress in coupling models of coastline and fluvial dynamics. *Computers & Geosciences*, *53*, 21–29. https://doi.org/10.1016/j.cageo.2012.04.004

Ashworth, P. J., Ferguson, R. I., Ashmore, P. E., Paola, C., Powell, D. M., & Prestegaards, K. L. (1992). Measurements in a Braided River chute and lobe: 2. Sorting of bed load during entrainment, transport, and deposition. *Water Resources Research*, *28*(7), 1887–1896. https://doi.org/10.1029/92WR00702

Ashworth, P. J., Best, J. L., & Jones, M. (2004). Relationship between sediment supply and avulsion frequency in braided rivers. *Geology*, *32*(1), 21. https://doi.org/10.1130/G19919.1

Baar, A. W., de Smit, J., Uijttewaal, W. S. J., & Kleinhans, M. G. (2018). Sediment Transport of Fine Sand to Fine Gravel on Transverse Bed Slopes in Rotating Annular Flume Experiments. *Water Resources Research*, *54*(1), 19–45. https://doi.org/10.1002/2017WR020604

Barile, G. (2023). A Python 1D numerical model of a river bifurcation. https://doi.org/10.5281/zenodo.10079752

Barile, G., Pirlot, P., Redolfi, M., & Tubino, M. (2023, September). Effect of width asymmetry on equilibrium and stability of river bifurcations. In R. O. Tinoco, V. Prasad, H. You, Y. Luo, C. Salas, & T. Shukla (Eds.), *13th symposium on river, coastal, and estuarine morphodynamics* (p. 143).

Barile, G., Ragno, N., Redolfi, M., & Tubino, M. (2023, September). Modelling deltaic bifurcations with self-evolving branches. In R. O. Tinoco, V. Prasad, H. You, Y. Luo, C. Salas, & T. Shukla (Eds.), *13th symposium on river, coastal, and estuarine morphodynamics* (p. 48).

Barile, G., Passalacqua, P., Kwon, S., & Tubino, M. (2024, November). Controlling factors on water and sediment partitioning at deltaic bifurcations. https://doi.org/10.22541/essoar.173159997.71559823/v1

Barile, G., Redolfi, M., & Tubino, M. (2022). Exploring river bifurcations response to time-dependent external forcings. *EGU22*. https://doi.org/10.5194/egusphere-egu22-9761

Barile, G., Redolfi, M., & Tubino, M. (2024). Analysis of autogenic bifurcation processes resulting in river avulsion. *Earth Surface Dynamics*, *12*(1), 87–103. https://doi.org/10.5194/esurf-12-87-2024

Bertoldi, W. (2012). Life of a bifurcation in a gravel-bed braided river. *Earth Surface Processes and Landforms*, *37*(12), 1327–1336. https://doi.org/10.1002/esp.3279

Bertoldi, W., & Tubino, M. (2007). River bifurcations: Experimental observations on equilibrium configurations. *Water Resources Research*, *43*(10), 1–10. https://doi.org/10.1029/2007WR005907

Bertoldi, W., Zanoni, L., Miori, S., Repetto, R., & Tubino, M. (2009). Interaction between migrating bars and bifurcations in gravel bed rivers. *Water Resources Research*, *45*(6), 1–12. https://doi.org/10.1029/2008WR007086

Bogoni, M., Putti, M., & Lanzoni, S. (2017). Modeling meander morphodynamics over self-formed heterogeneous floodplains. *Water Resources Research*, *53*(6), 5137–5157. https://doi.org/10.1002/2017WR020726

Bolla Pittaluga, M., Coco, G., & Kleinhans, M. G. (2015). A unified framework for stability of channel bifurcations in gravel and sand fluvial systems. *Geophysical Research Letters*, *42*(18), 7521–7536. https://doi.org/10.1002/2015GL065175

Bolla Pittaluga, M., Repetto, R., & Tubino, M. (2003). Channel bifurcation in braided rivers: Equilibrium configurations and stability. *Water Resources Research*, *39*(3), 1–13. https://doi.org/10.1029/2001WR001112

Brooke, S., Chadwick, A. J., Silvestre, J., Lamb, M. P., Edmonds, D. A., & Ganti, V. (2022). Where rivers jump course. *Science*, *376*(6596), 987–990. https://doi.org/10.1126/science.abm1215

Bulle, H. (1926). Untersuchungen über die geschiebeableitung bei der spaltung von wasserläufen: Modellversuche aus dem flussbaulaboratoriumder technischen hochschule zu karlsruhe.

Burge, L. M. (2006). Stability, morphology and surface grain size patterns of channel bifurcation in gravel–cobble bedded anabranching rivers. *Earth Surface Processes and Landforms*, *31*(10), 1211–1226. https://doi.org/10.1002/esp.1325

Buschman, F. A., Hoitink, A. J. F., van der Vegt, M., & Hoekstra, P. (2010). Subtidal flow division at a shallow tidal junction. *Water Resources Research*, *46*(12). https://doi.org/10.1029/2010WR009266

Cantelli, A., Paola, C., & Parker, G. (2004). Experiments on upstream-migrating erosional narrowing and widening of an incisional channel caused by dam removal. *Water Resources Research*, *40*(3), 1–12. https://doi.org/10.1029/2003WR002940

Carlin, M., Redolfi, M., & Tubino, M. (2021). The Long-Term Response of Alternate Bars to the Hydrological Regime. *Water Resources Research*, *57*(7), e2020WR029314. https://doi.org/10.1029/2020WR029314

Chadwick, A. J., Lamb, M. P., & Ganti, V. (2020). Accelerated river avulsion frequency on lowland deltas due to sea-level rise. *Proceedings of the National Academy of Sciences*, *117*(30), 17584–17590. https://doi.org/10.1073/pnas.1912351117

Chatanantavet, P., Lamb, M. P., & Nittrouer, J. A. (2012). Backwater controls of avulsion location on deltas. *Geophysical Research Letters*, *39*(1), n/a–n/a. https://doi.org/10.1029/2011GL050197

Chowdhury, M. K., Blom, A., Ylla Arbós, C., Verbeek, M. C., Schropp, M. H. I., & Schielen, R. M. J. (2023). Semicentennial Response of a Bifurcation Region in an Engineered River to Peak Flows and Human Interventions. *Water Resources Research*, *59*(4), e2022WR032741. https://doi.org/10.1029/2022WR032741

Coffey, T. S., & Shaw, J. B. (2017). Congruent Bifurcation Angles in River Delta and Tributary Channel Networks. *Geophysical Research Letters*, *44*(22), 11, 427–11, 436. https://doi.org/10.1002/2017GL074873

Colombini, M., Seminara, G., & Tubino, M. (1987). Finite-amplitude alternate bars. *Journal of Fluid Mechanics*, *181*(-1), 213. https://doi.org/10.1017/S0022112087002064

Cortese, L., Donatelli, C., Zhang, X., Nghiem, J. A., Simard, M., Jones, C. E., Denbina, M., Fichot, C. G., Harringmeyer, J. P., & Fagherazzi, S. (2024). Coupling numerical models of deltaic wetlands with AirSWOT, UAVSAR, and AVIRIS-NG remote sensing data. *Biogeosciences (Online)*, *21*(1), 241–260. https://doi.org/10.5194/bg-21-241-2024

Cui, Y., Parker, G., Braudrick, C., Dietrich, W. E., & Cluer, B. (2006). Dam removal express assessment models (DREAM). Part 1: Model development and validation. *Journal of Hydraulic Research*, *44*(3), 291–307. https://doi.org/10.1080/00221686.2006.9521683

Denbina, M., Simard, M., Pavelsky, T., Christensen, A., Liu, K., & Lyon, C. (2020). Pre-delta-x: Channel bathymetry of the atchafalaya basin, LA, USA, 2016. https://doi.org/10.3334/ORNLDAAC/1807

Dong, T. Y., Nittrouer, J. A., McElroy, B., Il'icheva, E., Pavlov, M., Ma, H., Moodie, A. J., & Moreido, V. M. (2020). Predicting Water and Sediment Partitioning in a Delta Channel Network Under Varying Discharge Conditions. *Water Resources Research*, *56*(11), e2020WR027199. https://doi.org/10.1029/2020WR027199

Durante, L., Pittaluga, M. B., Porcile, G., & Tambroni, N. (2023, December). Downstream control on the stability of river bifurcations. https://doi.org/10.22541/essoar.170158316.69242031/v1

Dutta, S., Wang, D., Tassi, P., & Garcia, M. H. (2017). Three-dimensional numerical modeling of the Bulle effect: The nonlinear distribution of near-bed sediment at fluvial diversions. *Earth Surface Processes and Landforms*, *42*(14), 2322–2337. https://doi.org/10.1002/esp.4186

Edmonds, D. A. (2012). Stability of backwater-influenced river bifurcations: A study of the Mississippi-Atchafalaya system. *Geophysical Research Letters*, *39*(8), 1–5. https://doi.org/10.1029/2012GL051125

Edmonds, D. A., & Slingerland, R. L. (2008). Stability of delta distributary networks and their bifurcations. *Water Resources Research*, *44*(9), 9426. https://doi.org/10.1029/2008WR006992

Edmonds, D. A., Chadwick, A. J., Lamb, M. P., Lorenzo-Trueba, J., Murray, A. B., Nardin, W., Salter, G., & Shaw, J. B. (2022). Morphodynamic Modeling of River-Dominated Deltas: A Review and Future Perspectives. In *Treatise on Geomorphology* (pp. 110–140). Elsevier. https://doi.org/10.1016/B978-0-12-818234-5.00076-6

Edmonds, D. A., Hoyal, D. C., Sheets, B. A., & Slingerland, R. L. (2009). Predicting delta avulsions: Implications for coastal wetland restoration. *Geology*, *37*(8), 759–762. https://doi.org/10.1130/G25743A.1

Edmonds, D. A., Paola, C., Hoyal, D. C. J. D., & Sheets, B. A. (2011). Quantitative metrics that describe river deltas and their channel networks. *Journal of Geophysical Research: Earth Surface*, *116*(F4). https://doi.org/10.1029/2010JF001955

Eke, E. C., Czapiga, M. J., Viparelli, E., Shimizu, Y., Imran, J., Sun, T., & Parker, G. (2014). Coevolution of width and sinuosity in meandering rivers. *Journal of Fluid Mechanics*, *760*, 127–174. https://doi.org/10.1017/jfm.2014.556

Engelund, F., & Hansen, E. (1967). A monograph on sediment transport in alluvial streams. *Technical University of Denmark ostervoldgade 10, Copenhagen K.*

Federici, B., & Paola, C. (2003). Dynamics of channel bifurcations in noncohesive sediments. *Water Resources Research*, *39*(6). https://doi.org/10.1029/2002WR001434

Ferguson, R. I. (1993). Understanding braiding processes in gravel-bed rivers: Progress and unsolved problems. *Geological Society, London, Special Publications*, *75*(1), 73–87. https://doi.org/10.1144/GSL.SP.1993.075.01.03

Ferguson, R. I. (2003). The missing dimension: Effects of lateral variation on 1-D calculations of fluvial bedload transport. *Geomorphology*, *56*(1-2), 1–14. https://doi.org/10.1016/S0169-555X(03)00042-4

Ferguson, R. I., Ashmore, P. E., Ashworth, P. J., Paola, C., & Prestegaard, K. L. (1992). Measurements in a Braided River chute and lobe: 1. Flow pattern, sediment transport, and channel change. *Water Resources Research*, *28*(7), 1877–1886. https://doi.org/10.1029/92WR00700

Fichot, C., & Harringmeyer, J. (2023). Delta-x: AVIRIS-NG L3-derived water quality, TSS, and turbidity, MRD, V3. https://doi.org/10.3334/ORNLDAAC/2152

Field, J. (2001). Channel avulsion on alluvial fans in southern Arizona. *Geomorphology*, *37*(1-2), 93–104. https://doi.org/10.1016/S0169-555X(00)00064-7

Gao, W., Shao, D., Wang, Z. B., Zhu, Z., & Yang, Z. (2024). System-Wide Effects of Local Bed Disturbance on the Morphological Evolution of a Bifurcating Channel Network. *Journal of Geophysical Research: Earth Surface*, *129*(3), e2023JF007514. https://doi.org/10.1029/2023JF007514

Gaweesh, A., & Meselhe, E. (2016). Evaluation of Sediment Diversion Design Attributes and Their Impact on the Capture Efficiency. *Journal of Hydraulic Engineering*, *142*(5), 04016002. https://doi.org/10.1061/(ASCE)HY.1943-7900.0001114

Germanoski, D., & Schumm, S. A. (1993). Changes in braided river morphology resulting from aggradation and degradation. *The Journal of Geology*, *101*(4), 451–466. https://doi.org/10.1086/648239

Griffiths, G. A. (1981). Stable-channel design in gravel-bed rivers. *Journal of Hydrology*, *52*(3), 291–305. https://doi.org/10.1016/0022-1694(81)90176-1

Habersack, H., & Piégay, H. (2007). 27 River restoration in the Alps and their surroundings: Past experience and future challenges. *Developments in Earth Surface Processes*, *11*, 703–735. https://doi.org/10.1016/S0928-2025(07)11161-5

Han, J., & Kim, W. (2022). Linking levee-building processes with channel avulsion: Geomorphic analysis for assessing avulsion frequency and channel reoccupation. *Earth Surface Dynamics*, *10*(4), 743–759. https://doi.org/10.5194/esurf-10-743-2022

Hariharan, J., Piliouras, A., Schwenk, J., & Passalacqua, P. (2022). Width-Based Discharge Partitioning in Distributary Networks: How Right We Are. *Geophysical Research Letters*, *49*(14), e2022GL097897. https://doi.org/10.1029/2022GL097897

Hariharan, J., Wright, K., & Passalacqua, P. (2020). Dorado: A Python package for simulating passive particle transport in shallow-water flows. *Journal of Open Source Software*, *5*(54), 2585. https://doi.org/10.21105/joss.02585

Harringmeyer, J. P., Ghosh, N., Weiser, M. W., Thompson, D. R., Simard, M., Lohrenz, S. E., & Fichot, C. G. (2024). A hyperspectral view of the nearshore Mississippi River Delta: Characterizing suspended particles in coastal wetlands using imaging spectroscopy. *Remote Sensing of Environment*, *301*(November 2023). https://doi.org/10.1016/j.rse.2023.113943

Herrero, A., Bateman, A., & Medina, V. (2015). Water flow and sediment transport in a 90° channel diversion: An experimental study. *Journal of Hydraulic Research*, *53*(2), 253–263. https://doi.org/10.1080/00221686.2014.989457

Hines, C., & Piliouras, A. (2024). Suspended Sediment Transport and Storage in Arctic Deltas. *Journal of Geophysical Research: Earth Surface*, *129*(12), e2024JF007802. https://doi.org/10.1029/2024JF007802

Ikeda, S., Parker, G., & Sawai, K. (1981). Bend theory of river meanders. Part 1. Linear development. *Journal of Fluid Mechanics*, *112*, 363–377. https://doi.org/10.1017/S0022112081000451

Iwantoro, A. P., van der Vegt, M., & Kleinhans, M. G. (2022). Stability and Asymmetry of Tide-Influenced River Bifurcations. *Journal of Geophysical Research: Earth Surface*, *127*(6), e2021JF006282. https://doi.org/10.1029/2021JF006282

Iwantoro, A. P., van der Vegt, M., & Kleinhans, M. G. (2021). Effects of sediment grain size and channel slope on the stability of river bifurcations. *Earth Surface Processes and Landforms*, *46*(10), 2004–2018. https://doi.org/10.1002/esp.5141

Jerolmack, D. J. (2006). *Modeling the Dynamics and Depositional Patterns of Sandy Rivers* [Doctoral dissertation, MASSACHUSETTS INSTITUTE OF TECHNOLOGY]. http://dspace.mit.edu/handle/1721.1/37277

Jerolmack, D. J., & Mohrig, D. (2007). Conditions for branching in depositional rives. *Geology*, *35*(5), 463–466. https://doi.org/10.1130/G23308A.1

Kästner, K., & Hoitink, A. J. F. (2019). Flow and Suspended Sediment Division at Two Highly Asymmetric Bifurcations in a River Delta: Implications for Channel

Stability. *Journal of Geophysical Research: Earth Surface*, *124*(10), 2358–2380. https://doi.org/10.1029/2018JF004994

Kästner, K., & Hoitink, A. J. F. (2020). Idealized Model for the Deflection of Sediment Into Lateral Branches of Lowland Rivers. *Water Resources Research*, *56*(6), e2019WR026602. https://doi.org/10.1029/2019WR026602

Kim, W., Mohrig, D., Twilley, R., Paola, C., & Parker, G. (2009). Is It Feasible to Build New Land in the Mississippi River Delta? *Eos, Transactions American Geophysical Union*, *90*(42), 373–374. https://doi.org/10.1029/2009EO420001

Kleinhans, M. G., de Haas, T., Lavooi, E., & Makaske, B. (2012). Evaluating competing hypotheses for the origin and dynamics of river anastomosis. *Earth Surface Processes and Landforms*, *37*(12), 1337–1351. https://doi.org/10.1002/esp.3282

Kleinhans, M. G., Ferguson, R., Lane, S. N., & Hardy, R. J. (2013). Splitting rivers at their seams: Bifurcations and avulsion. *Earth Surface Processes and Landforms*, *38*(1), 47–61. https://doi.org/10.1002/esp.3268

Kleinhans, M. G., Jagers, H. R., Mosselman, E., & Sloff, C. J. (2008). Bifurcation dynamics and avulsion duration in meandering rivers by one-dimensional and three-dimensional models. *Water Resources Research*, *44*(8). https://doi.org/10.1029/2007WR005912

Konsoer, K. M., Siddique, S. T., & Wampler, P. J. (2024). Long-term geomorphic effects of longitudinal training walls in the Grand River, Michigan (USA). *Geomorphology*, *463*, 109342. https://doi.org/10.1016/j.geomorph.2024.109342

Ksiazek, L., & Meijer, D. G. (2011). Changes of Sediment Distribution in a Channel Bifurcation – 3D Modeling. In P. Rowinski (Ed.), *Experimental Methods in Hydraulic Research* (pp. 175–187, Vol. 1). Springer Berlin Heidelberg. https://doi.org/10.1007/978-3-642-17475-9_11

Ku, H. H. (1966). Notes on the use of propagation of error formulas. *Journal of Research of the National Bureau of Standards. Section C: Engineering and Instrumentation*, *70C*(4), 263. https://doi.org/10.6028/jres.070C.025

Lanzoni, S., & Tubino, M. (1999). Grain sorting and bar instability. *Journal of Fluid Mechanics*, *393*, 149–174. https://doi.org/10.1017/S0022112099005583

Lauzon, R., & Murray, A. B. (2018). Comparing the cohesive effects of mud and vegetation on delta evolution. *Geophysical Research Letters*, *45*(19), 10, 437–10, 445. https://doi.org/10.1029/2018GL079405

Le, T. B., Crosato, A., & Montes Arboleda, A. (2020). Revisiting Waal River Training by Historical Reconstruction. *Journal of Hydraulic Engineering*, *146*(5), 05020002. https://doi.org/10.1061/(ASCE)HY.1943-7900.0001688

Le, T. B., Crosato, A., Mosselman, E., & Uijttewaal, W. S. (2018). On the stability of river bifurcations created by longitudinal training walls. Numerical investigation. *Advances in Water Resources*, *113*, 112–125. https://doi.org/10.1016/j.advwatres.2018.01.012

Le, T. B., Crosato, A., & Uijttewaal, W. S. (2018). Long-term morphological developments of river channels separated by a longitudinal training wall. *Advances in Water Resources*, *113*, 73–85. https://doi.org/10.1016/j.advwatres.2018.01.007

Leddy, J. O., Ashworth, P. J., & Best, J. L. (1993). Mechanisms of anabranch avulsion within gravel-bed braided rivers: Observations from a scaled physical model. *Geological Society, London, Special Publications*, *75*(1), 119–127. https://doi.org/10.1144/GSL.SP.1993.075.01.07

Liang, M., Voller, V. R., & Paola, C. (2015). A reduced-complexity model for river delta formation – Part 1: Modeling deltas with channel dynamics. *Earth Surface Dynamics*, *3*(1), 67–86. https://doi.org/10.5194/esurf-3-67-2015

Liang, M., Van Dyk, C., & Passalacqua, P. (2016). Quantifying the patterns and dynamics of river deltas under conditions of steady forcing and relative sea level rise. *Journal of Geophysical Research: Earth Surface*, *121*(2), 465–496. https://doi.org/10.1002/2015JF003653

Makaske, B. (2001). Anastomosing rivers: A review of their classification, origin and sedimentary products. *Earth-Science Reviews*, *53*(3-4), 149–196. https://doi.org/10.1016/S0012-8252(00)00038-6

Mandler, H., Petutschnig, W., & Sereinig, N. (2004). *LIFE-projekt auenverbund obere drau. Endbericht* (tech. rep.). Amt der Kärntner Landesregierung. Klagenfurt.

Marti, C., & Bezzola, G. R. (2006). Bed load transport in braided gravel-bed rivers (G. H. Best, J. L. Bristow, & C. S. Petts, Eds.). *Braided Rivers: Process, Deposits, Ecology and Management. Special Publication*, *36*(1979), 199–215.

Mendoza, A., Berezowsky, M., Caballero, C., & Arganis-Juárez, M. (2022). Alteration of the flow distribution at a river bifurcation caused by a system of upstream dams: Case of the Grijalva River basin, Mexico. *Earth Surface Processes and Landforms*, *47*(2), 509–521. https://doi.org/10.1002/esp.5265

Meselhe, E. A., Sadid, K. M., & Allison, M. A. (2016). Riverside morphological response to pulsed sediment diversions. *Geomorphology*, *270*, 184–202. https://doi.org/10.1016/j.geomorph.2016.07.023

Meyer-Peter, E., & Müller, R. (1948). Formulas for Bed-Load transport. *IAHSR 2nd Meeting, Stockholm, Appendix 2*. Retrieved June 19, 2021, from https://repository.tudelft.nl/islandora/object/uuid%3A4fda9b61-be28-4703-ab06-43cdc2a21bd7

Miori, S., Repetto, R., & Tubino, M. (2006a). A one-dimensional model of bifurcations in gravel bed channels with erodible banks. *Water Resources Research*, *42*(11), 1–12. https://doi.org/10.1029/2006WR004863

Miori, S., Repetto, R., & Tubino, M. (2006b, August). Unsteadiness effects on the morphological behaviour of gravel-bed river bifurcations. In E. Alves, A. Cardoso, J. Leal, & R. Ferreira (Eds.), *River Flow 2006*. Taylor & Francis. https://doi.org/10.1201/9781439833865.ch136

Miori, S., Hardy, R. J., & Lane, S. N. (2012). Topographic forcing of flow partition and flow structures at river bifurcations. *Earth Surface Processes and Landforms*, *37*(6), 666–679. https://doi.org/10.1002/esp.3204

Mohrig, D., Heller, P. L., Paola, C., & Lyons, W. J. (2000). Interpreting avulsion process from ancient alluvial sequences: GuadalopeMatarranya system (Northern Spain) and Wasatch formation (Western Colorado). *Geological Society of America Bulletin*, *112*(12), 1787. https://doi.org/10.1130/0016-7606(2000)112<1787:IAPFAA>2.0.CO;2

Monegaglia, F., & Tubino, M. (2019). The Hydraulic Geometry of Evolving Meandering Rivers. *Journal of Geophysical Research: Earth Surface*, *124*(11), 2723–2748. https://doi.org/10.1029/2019JF005309

Monegaglia, F., Tubino, M., & Zolezzi, G. (2019). Interaction between curvature-driven width oscillations and channel curvature in evolving meander bends. *Journal of Fluid Mechanics*, *876*, 985–1017. https://doi.org/10.1017/jfm.2019.574

Muhar, S., Januschke, K., Kail, J., Poppe, M., Schmutz, S., Hering, D., & Buijse, A. D. (2016). Evaluating good-practice cases for river restoration across Europe: Context, methodological framework, selected results and recommendations. *Hydrobiologia*, *769*(1), 3–19. https://doi.org/10.1007/s10750-016-2652-7

Nghiem, J., Salter, G., & Lamb, M. (2023). Delta-x: Bed and suspended sediment grain size, MRD, LA, USA, 2021, version 2. https://doi.org/10.3334/ORNLDAAC/2135

Nghiem, J., Salter, G., & Lamb, M. (2025). Delta-x: Bed and suspended sediment grain size, MRD, LA, USA, 2019-2021, V3. https://doi.org/10.3334/ORNLDAAC/2379

Paola, C. (1996). Incoherent structure: Turbulence as a metaphor for stream braiding (P. J. Ashworth, Ed.). *Coherent Flow Structures in Open Channels*, *65*, 705–723.

Paola, C., Twilley, R. R., Edmonds, D. A., Kim, W., Mohrig, D., Parker, G., Viparelli, E., & Voller, V. R. (2011). Natural Processes in Delta Restoration: Application to the Mississippi Delta. *Annual Review of Marine Science*, *3*(Volume 3, 2011), 67–91. https://doi.org/10.1146/annurev-marine-120709-142856

Parker, G. (1990). Relation permettant le calcul du charriage dans les rivieres a graviers, a partir de la composition de surface. *Journal of Hydraulic Research*, *28*(4), 417–436. https://doi.org/10.1080/00221689009499058

Parker, G., Shimizu, Y., Wilkerson, G. V., Eke, E. C., Abad, J. D., Lauer, J. W., Paola, C., Dietrich, W. E., & Voller, V. R. (2011). A new framework for modeling the migration of meandering rivers. *Earth Surface Processes and Landforms*, *36*(1), 70–86. https://doi.org/10.1002/esp.2113

Parker, G. (1978). Self-formed straight rivers with equilibrium banks and mobile bed. Part 2. The gravel river. *Journal of Fluid Mechanics*, *89*(01), 127–146. https://doi.org/10.1017/S0022112078002505

Parker, G. (1979). Hydraulic Geometry of Active Gravel Rivers. *Journal of the Hydraulics Division*, *105*(9), 1185–1201. https://doi.org/10.1061/JYCEAJ.0005275

Parker, G. (2004). Chapter 15: Extension of 1D model to include bank erosion and floodplain deposition. In *1D sediment transport morphodynamics with applications to rivers and turbidity currents*. http://hydrolab.illinois.edu/people/parkerg/powerpoint_lectures.htm

Parsons, D. R., Best, J. L., Lane, S. N., Orfeo, O., Hardy, R. J., & Kostaschuk, R. (2007). Form roughness and the absence of secondary flow in a large confluence–diffluence, Rio Paraná, Argentina. *Earth Surface Processes and Landforms*, *32*(1), 155–162. https://doi.org/10.1002/esp.1457

Passalacqua, P., Giosan, L., Goodbred, S., & Overeem, I. (2021). Stable ≠ Sustainable: Delta Dynamics Versus the Human Need for Stability. *Earth's Future*, *9*(7), e2021EF002121. https://doi.org/10.1029/2021EF002121

Pirlot, P. (2024). *Morphodynamics of Multi-Thread Rivers* [Doctoral dissertation, University of Trento]. https://hdl.handle.net/11572/440090

Ragno, N., Redolfi, M., & Tubino, M. (2021). Coupled Morphodynamics of River Bifurcations and Confluences. *Water Resources Research*, *57*(1). https://doi.org/10.1029/2020WR028515

Ragno, N., Redolfi, M., & Tubino, M. (2022a, July). Loops length data. https://doi.org/10.5281/zenodo.6901398

Ragno, N. (2023). Viewing second-order phase transitions as a metaphor for river bifurcations. *Journal of Fluid Mechanics*, *974*, A53. https://doi.org/10.1017/jfm.2023.831

Ragno, N., Redolfi, M., Tambroni, N., & Tubino, M. (2023). Modeling Steady Grain Sorting in River Bifurcations. *Journal of Geophysical Research: Earth Surface*, *128*(9), e2023JF007230. https://doi.org/10.1029/2023JF007230

Ragno, N., Redolfi, M., & Tubino, M. (2022b). Quasi-Universal Length Scale of River Anabranches. *Geophysical Research Letters*, *49*(16), e2022GL099928. https://doi.org/10.1029/2022GL099928

Ragno, N., Tambroni, N., & Bolla Pittaluga, M. (2020). Effect of Small Tidal Fluctuations on the Stability and Equilibrium Configurations of Bifurcations. *Journal of Geophysical Research: Earth Surface*, *125*(8), 1–20. https://doi.org/10.1029/2020JF005584

Ragno, N., & Tubino, M. (2025). Equilibrium of morphological units in anabranching rivers. *Earth Surface Processes and Landforms*, *50*(2), e70004. https://doi.org/10.1002/esp.70004

Raudkivi, A. J. (1993). *Sedimentation: Exclusion and Removal of Sediment from Diverted Water*. CRC Press. https://doi.org/10.1201/9781003077619

Redolfi, M., & Tubino, M. (2014). A diffusive 1D model for the evolution of a braided network subject to varying sediment supply, 1153–1161. https://doi.org/10.1201/b17133-155

Redolfi, M. (2023). Defining the length parameter in river bifurcation models: A theoretical approach. *Earth Surface Processes and Landforms*, *48*(11), 2121–2132. https://doi.org/10.1002/esp.5673

Redolfi, M., Zolezzi, G., & Tubino, M. (2016). Free instability of channel bifurcations and morphodynamic influence. *Journal of Fluid Mechanics*, *799*, 476–504. https://doi.org/10.1017/jfm.2016.389

Redolfi, M., Zolezzi, G., & Tubino, M. (2019). Free and forced morphodynamics of river bifurcations. *Earth Surface Processes and Landforms*, *44*(4), 973–987. https://doi.org/10.1002/esp.4561

Roberts, S., Nielsen, O., Gray, D., Sexton, J., & Davies, G. (2015). *ANUGA user manual*. Manual. https://anuga.anu.edu.au/export/9668/trunk/anuga_core/doc/anuga_user_manual.pdf

Rodrigues, S., Bréhéret, J.-G., Macaire, J.-J., Moatar, F., Nistoran, D., & Jugé, P. (2006). Flow and sediment dynamics in the vegetated secondary channels of an anabranching river: The Loire River (France). *Sedimentary Geology*, *186*(1-2), 89–109. https://doi.org/10.1016/j.sedgeo.2005.11.011

Salter, G., Paola, C., & Voller, V. R. (2018). Control of Delta Avulsion by Downstream Sediment Sinks. *Journal of Geophysical Research: Earth Surface*, *123*(1), 142–166. https://doi.org/10.1002/2017JF004350

Salter, G., Voller, V. R., & Paola, C. (2019). How does the downstream boundary affect avulsion dynamics in a laboratory bifurcation? *Earth Surface Dynamics*, *7*(4), 911–927. https://doi.org/10.5194/esurf-7-911-2019

Santini, W., Camenen, B., Le Coz, J., Vauchel, P., Guyot, J. L., Lavado, W., Carranza, J., Paredes, M. A., Arévalo, J. J., Arévalo, N., Villar, R. E., Julien, F., & Martinez, J. M. (2019). An index concentration method for suspended load monitoring in large rivers of the Amazonian foreland. *Earth Surface Dynamics*, *7*(2), 515–536. https://doi.org/10.5194/esurf-7-515-2019

Sassi, M. G., Hoitink, A. J. F., Vermeulen, B., & Hidayat, H. (2013). Sediment discharge division at two tidally influenced river bifurcations. *Water Resources Research*, *49*(4), 2119–2134. https://doi.org/10.1002/WRCR.20216

Seal, R., & Paola, C. (1995). Observations of Downstream Fining on the North Fork Toutle River Near Mount St. Helens, Washington. *Water Resources Research*, *31*(5), 1409–1419. https://doi.org/10.1029/94WR02976

Seminara, G. (2010). Fluvial Sedimentary Patterns. *Annual Review of Fluid Mechanics*, *42*(1), 43–66. https://doi.org/10.1146/annurev-fluid-121108-145612

Seminara, G., & Tubino, M. (1992). Weakly nonlinear theory of regular meanders. *Journal of Fluid Mechanics*, *244*(-1), 257. https://doi.org/10.1017/S0022112092003069

Seminara, G., Zolezzi, G., Tubino, M., & Zardi, D. (2001). Downstream and upstream influence in river meandering. Part 2. Planimetric development. *Journal of Fluid Mechanics*, *438*, 213–230. https://doi.org/10.1017/S0022112001004281

Shaw, J. B., Estep, J. D., Whaling, A. R., Sanks, K. M., & Edmonds, D. A. (2018). Measuring subaqueous progradation of the Wax Lake Delta with a model of flow direction divergence. *Earth Surface Dynamics*, *6*(4), 1155–1168. https://doi.org/10.5194/esurf-6-1155-2018

Shaw, J. B., Mohrig, D., & Whitman, S. K. (2013). The morphology and evolution of channels on the Wax Lake Delta, Louisiana, USA. *Journal of Geophysical Research: Earth Surface*, *118*(3), 1562–1584. https://doi.org/10.1002/jgrf.20123

Siviglia, A., Stecca, G., Vanzo, D., Zolezzi, G., Toro, E. F., & Tubino, M. (2013). Numerical modelling of two-dimensional morphodynamics with applications to river bars and bifurcations. *Advances in Water Resources*, *52*, 243–260. https://doi.org/10.1016/j.advwatres.2012.11.010

Slingerland, R., & Smith, N. D. (1998). Necessary conditions for a meandering-river avulsion. *Geology*, *26*(5), 435–438. https://doi.org/10.1130/0091-7613(1998)026<0435:NCFAMR>2.3.CO;2

Slingerland, R., & Smith, N. D. (2004). River avulsions and their deposits. *Annual Review of Earth and Planetary Sciences*, *32*(Qian 1990), 257–285. https://doi.org/10.1146/annurev.earth.32.101802.120201

Smith, N. D. (1978). Avulsion. In G. V. Middleton, M. J. Church, M. Coniglio, L. A. Hardie, & F. J. Longstaffe (Eds.), *Encyclopedia of sediments and sedimentary rocks* (pp. 34–36). Springer Netherlands. https://doi.org/10.1007/978-1-4020-3609-5_16

Szewczyk, L., Grimaud, J.-L., & Cojan, I. (2020). Experimental evidence for bifurcation angles control on abandoned channel fill geometry. *Earth Surface Dynamics*, *8*(2), 275–288. https://doi.org/10.5194/esurf-8-275-2020

Tejedor, A., Longjas, A., Zaliapin, I., & Foufoula-Georgiou, E. (2015). Delta channel networks: 1. A graph-theoretic approach for studying connectivity and steady state transport on deltaic surfaces. *Water Resources Research*, *51*(6), 3998–4018. https://doi.org/10.1002/2014WR016577

Thomas, R. E., Parsons, D. R., Sandbach, S. D., Keevil, G. M., Marra, W. A., Hardy, R. J., Best, J. L., Lane, S. N., & Ross, J. A. (2011). An experimental study of discharge partitioning and flow structure at symmetrical bifurcations. *Earth Surface Processes and Landforms*, *36*(15), 2069–2082. https://doi.org/10.1002/esp.2231

Toonen, W. H. J., Kleinhans, M. G., & Cohen, K. M. (2012). Sedimentary architecture of abandoned channel fills. *Earth Surface Processes and Landforms*, *37*(4), 459–472. https://doi.org/10.1002/esp.3189

Tritthart, M., Vanzo, D., Chavarrías, V., Siviglia, A., Sloff, K., & Mosselman, E. (2024). Why do published models for fluvial and estuarine morphodynamics use unrealistic representations of the effects of transverse bed slopes? *Advances in Water Resources*, *193*, 104831. https://doi.org/10.1016/j.advwatres.2024.104831

Tubino, M., & Seminara, G. (1990). Free–forced interactions in developing meanders and suppression of free bars. *Journal of Fluid Mechanics*, *214*, 131–159. https://doi.org/10.1017/S0022112090000088

Tubino, M. (1991). Growth of alternate bars in unsteady flow. *Water Resources Research*, *27*(1), 37–52. https://doi.org/10.1029/90WR01699

Tull, N., Passalacqua, P., Hassenruck-Gudipati, H. J., Rahman, S., Wright, K., Hariharan, J., & Mohrig, D. (2022). Bidirectional River-Floodplain Connectivity During Combined Pluvial-Fluvial Events. *Water Resources Research*, *58*(3), e2021WR030492. https://doi.org/10.1029/2021WR030492

Van Denderen, R. P., Schielen, R. M., Westerhof, S. G., Quartel, S., & Hulscher, S. J. (2019). Explaining artificial side channel dynamics using data analysis and model calculations. *Geomorphology*, *327*, 93–110. https://doi.org/10.1016/j.geomorph.2018.10.016

van der Mark, C. F., & Mosselman, E. (2013). Effects of helical flow in one-dimensional modelling of sediment distribution at river bifurcations. *Earth Surface Processes and Landforms*, *38*(5), 502–511. https://doi.org/10.1002/esp.3335

Van Dijk, M., Kleinhans, M. G., Postma, G., & Kraal, E. (2012). Contrasting morphodynamics in alluvial fans and fan deltas: Effect of the downstream boundary. *Sedimentology*, *59*(7), 2125–2145. https://doi.org/10.1111/j.1365-3091.2012.01337.x

Vuren, S., Havinga, H., & Schielen, R. (2006). Tension between navigation, maintenance and safety calls for an integrated planning of flood protection measures. *River, Coastal and Estuarine Morphodynamics: RCEM 2009*.

Wagner, W., & Mohrig, D. (2019). Flow and Sediment Flux Asymmetry in a Branching Channel Delta. *Water Resources Research*, *55*(11), 9563–9577. https://doi.org/10.1029/2019WR026050

Wang, Z. B., De Vries, M., Fokkink, R. J., & Langerak, A. (1995). Stabilité des bifurcations de rivières dans des modèles morphodynamiques filaires. *Journal of Hydraulic Research*, *33*(6), 739–750. https://doi.org/10.1080/00221689509498549

Wang, Z.-Y., Hu, S., Wu, Y., & Shao, X. (2003). Delta processes and management strategies in China. *International Journal of River Basin Management*, *1*(2), 173–184. https://doi.org/10.1080/15715124.2003.9635204

Wolman, G. M., & Miller, J. P. (1960). Magnitude and frequency of forces in geomorphic processes. *The Journal of Geology*, *68*(1), 54–74.

Wong, M., & Parker, G. (2006). One-dimensional modeling of bed evolution in a gravel bed river subject to a cycled flood hydrograph. *Journal of Geophysical Research: Earth Surface*, *111*(F3). https://doi.org/10.1029/2006JF000478

Wright, K., & Passalacqua, P. (2024). Delta-x: Calibrated ANUGA hydrodynamic outputs for the atchafalaya basin, MRD, LA. https://doi.org/10.3334/ORNLDAAC/2306

Wright, K., Hariharan, J., Passalacqua, P., Salter, G., & Lamb, M. P. (2022). From Grains to Plastics: Modeling Nourishment Patterns and Hydraulic Sorting of Fluvially Transported Materials in Deltas. *Journal of Geophysical Research: Earth Surface*, *127*(11), e2022JF006769. https://doi.org/10.1029/2022JF006769

Wright, K., Passalacqua, P., Simard, M., & Jones, C. E. (2022). Integrating Connectivity Into Hydrodynamic Models: An Automated Open-Source Method to Refine an Unstructured Mesh Using Remote Sensing. *Journal of Advances in Modeling Earth Systems*, *14*(8), e2022MS003025. https://doi.org/10.1029/2022MS003025

Zolezzi, G., & Seminara, G. (2001). Downstream and upstream influence in river meandering. Part 1. General Theory and Application to Overdeepening. *Journal of Fluid Mechanics*, *438*(July), 183–211. https://doi.org/10.1017/S002211200100427X

Zolezzi, G., Bertoldi, W., & Tubino, M. (2006). Morphological Analysis and Prediction of River Bifurcations. In *Braided Rivers* (pp. 233–256). Blackwell Publishing Ltd. https://doi.org/10.1002/9781444304374.ch11